ACOUSTIC EMISSION BASED STRUCTURAL HEALTH MONITORING OF CORRODED/UN-CORRODED CONCRETE STRUCTURES

by

© Ahmed Abdallah Abouhussien, B.Sc., M.Eng.

A thesis submitted to the

School of Graduate Studies

in partial fulfillment of the requirements for the degree of

Doctor of Philosophy (Civil Engineering)

Faculty of Engineering and Applied Science

Memorial University of Newfoundland

May 2017

St. John's, Newfoundland, Canada

ABSTRACT

Structural health monitoring (SHM) is a continuous nondestructive evaluation system used for both damage prognosis and diagnosis of civil structures. Acoustic emission (AE) technique is defined as a passive SHM method that enables the detection of any possible damage. AE technique has been exploited for condition assessment and long-term monitoring of civil infrastructure systems. AE sensors are sensitive to the micro-cracking stage of damage, therefore showed a great potential for early detection of different forms of deteriorations in reinforced concrete (RC) structures. The rate of deterioration in RC structures greatly increases due to reinforcing steel corrosion embedded in concrete. Corrosion results in both expansion and mass loss of steel, thus causing concrete cover cracking and delamination. Moreover, corrosion causes reduction of bond between concrete and steel, which reduces the overall strength of RC structures. The objectives of this research were to: a) utilize AE monitoring for early corrosion detection and concrete cover/steel damage quantification of small-scale RC specimens, b) evaluate and localize corrosion activity using distributed AE sensors in full-scale RC beams, c) attain an early detection of loss of bond between corroded steel and concrete at different corrosion levels, d) identify and assess bond degradation of corroded/un-corroded bars in both small- and full-scale RC beams, and e) develop relationships between the collected AE data and variable levels of corrosion, corrosion-induced cover crack growth, and bond deterioration in RC structures.

Four extensive experimental investigations have been conducted both on small- and full-scale RC elements to accomplish these aforementioned research objectives. AE

monitoring was implemented in these studies on RC elements including a total of 30 prisms, 114 pull-out samples, and 10 beam anchorage specimens under accelerated corrosion, direct pull-out, and four-point load tests, respectively. The analysis of AE data obtained from these tests was performed and compared to the results of half-cell potentials (HCP) standard tests, visual detection of corrosion-induced cracks, crack width measurements, and overall bond behaviour of all tested pull-out samples/beams. The results showed that the analysis of AE signal parameters acquired during corrosion tests enabled the detection of both corrosion and cover crack onset earlier than HCP readings and prior to any visible cracking in both small- and full-scale RC beams, regardless of cover thickness or sensor location. Analyzing the AE signals attained from the pull-out tests permitted the characterization of two early stages of bond degradation (micro- and macro-cracking) in both corroded and un-corroded specimens at all values of bar diameter, corrosion level, cover thickness, and embedded length. The AE analysis also allowed an early identification of three stages of bond damage in full-scale corroded/un-corroded RC beams namely; first crack, initial slip, and anchorage cracking, before their visual observation, irrespective of corrosion level, embedded length, or sensor location. The results of AE intensity analysis on AE signal strength data were exploited to develop damage classification charts to assess the extent of corrosion damage as well as to categorize different stages of bond deterioration in corroded/un-corroded small- and full-scale RC samples.

ACKNOWLEDGEMENTS

I want to express my great gratitude to my thesis advisor Dr. Assem Hassan for offering this great chance and for his continuous encouragement during both my M.Eng. and PhD programs and for his endless help during my first accommodation in St. John's. I would also like to thank my supervisory committee members Dr. Ashutosh Dhar and Dr. Sam Nakhla for agreeing to be in my thesis supervisory committee.

Many thanks are due to Mr. Shawn Organ and Mr. Jason Murphy for their generous assistance and their constant support during my various setups and test programs. Without their help this work would not have been completed.

Words cannot express my thankfulness to the support and encouragement provided by my parents, sisters, and my wife during my studies.

The funding provided by Dr. Assem Hassan, School of Graduate Studies, Mitacs-Accelerate Internship Program, and the RDC OISRA is greatly acknowledged.

Finally, I would embrace this opportunity to thank all my friends for encouraging me to finish this PhD degree, especially Amin Elgharbawy, Walid Jerjawi, Dr. Shadi Alawneh, Walid Saad, and all other colleagues in the Civil Engineering department.

Table of Contents

List of Tables

List of Figures

List of Symbols, Nomenclature or Abbreviations

ACI = American Concrete Institute

AE = Acoustic Emission

ASTM = American Society for Testing and Materials

CE = Cumulative Energy

CSA = Canadian Standard Association

CSS = Cumulative Signal Strength

DC = Direct Current

f_c' = Characteristic Compressive Strength of Concrete (MPa)

f_t' = Tensile Strength of Concrete (MPa)

FRP = Fibre-Reinforced Polymer

$H(t)$ = Historic Index

HCP = Half-Cell Potential

HDT = Hit Definition Time

HLT = Hit Lockout Time

LVDT = Linear Variable Differential Transformer

NDT = Non-destructive Testing

PDT = Peak Definition Time

RA = Rise Time / Maximum Amplitude

RC = Reinforced Concrete

SHM = Structural Health Monitoring

S_r = Severity

List of Appendices

1. Introduction

1.1 Background and Research Motivation

The majority of bridges, tunnels, dams, parking garages, oil platforms, and other components of civil infrastructure are made of reinforced concrete (RC). RC structures exposed to extreme environments are deteriorating at an alarming rate due to concrete durability problems. Corrosion of embedded reinforcing steel is the most critical factor affecting the durability of RC structures (Auyeung et al., 2000; ACI Committee 222, 2001; Fang et al., 2006; Gjørv, 2009; Elfergani et al., 2011; Talakokula and Bhalla, 2015). Concrete is naturally alkaline, which is significant because the alkaline nature of concrete provides embedded steel with corrosion protection. Unfortunately, chlorides from deicing salts, groundwater, or seawater reduce the concrete alkalinity after penetrating the concrete cover and reaching the reinforcing steel. Corrosion starts once the percentage of chloride around the steel bar exceeds the threshold needed for corrosion initiation. After corrosion initiation, corrosion progressively propagates through the reinforcing steel causing accumulation of rust products. This accumulation of rust products eventually leads to expansion of steel bars, cracking, and delamination of the concrete cover (Martin-Peréz et al., 1998; Auyeung et al., 2000; Hooton et al., 2002; Otieno et al., 2010; Kobayashi and Banthia, 2011). Several experimental and numerical studies have indicated that corrosion of reinforcing steel significantly reduces the bond strength of reinforced concrete structures. Reinforcement corrosion contributes to both the reduction of steel cross section and loss of its bond to surrounding concrete, thus minimizing the overall strength and serviceability of RC structures (Auyeung et al., 2000;

ACI Committee 222, 2001; Fang et al., 2006). Despite the design of concrete structures to ensure safe transfer of forces between steel and concrete, the existence of corrosion may weaken their bond and eventually cause sudden bond failures (ACI Committee 408, 2003).

Different nondestructive testing (NDT) techniques are successfully applied to identify and evaluate potential deterioration in RC structures (Maierhofer et al., 2010; Di Benedetti et al., 2014; Zaki et al., 2015). However, most of these methods are intrusive and require regular site visits for efficient condition assessment. Structural Health Monitoring (SHM) involves the continuous nondestructive evaluation method that allows both damage prognosis and diagnosis of concrete structures. For instance, SHM system for damage prognosis employs sensing technology to record, analyze, localize, and predict the deformation, cracking, and other types of damage of the monitored structure (Mufti et al., 2007; Farhidzadeh et al., 2012). SHM eliminates the need for routine site visits for evaluation and inspection of major civil structures and provides an early warning for any potential damage. The SHM system is comprised of embedded or attached sensors, a data acquisition or signal processing system, and other electronics that periodically obtain data from the structure. These sensors can provide quantitative data about the overall health of structures including strains, deformations, corrosion, fracture, and cracks. Examples of monitored structures include bridges, tunnels, dams, ships, oil platforms, and pipelines (Mufti et al., 2007; Farhidzadeh et al., 2012).

Acoustic Emission (AE) technique may be defined as a passive SHM method that allows the identification and localization of potential damage in civil structures. AE sensors are sensitive to the micro-cracking stage of damage, which enables the early detection of

different deterioration mechanisms in concrete structures in service (for example: Ohtsu, 1996; Ohtsu et al., 2002; Grosse et al., 2003; Ziehl et al., 2008; Nair and Cai, 2010; Carpinteri et al., 2011; Salamone et al., 2012; Mpalaskas et al., 2014; Abdelrahman et al., 2015). Micro-cracks resulting from any source of damage in RC structures eventually cause a release of strain energy, thus initiating elastic waves that can be collected by AE sensors. These sensors can be incorporated in SHM systems to capture any AE signal emitted from any form of stress, due to crack growth, and/or from other sources in a structure (Grosse et al., 2003; Nair and Cai, 2010). AE sensors can record a variety of signal parameters from different AE events when attached to the structure's surface or embedded inside. Owing to the limited research involving AE monitoring of RC structures, further research is needed to optimize the application of AE sensors for corrosion monitoring and bond damage detection/assessment, while considering the effects of crack growth created by expansions of reinforcing steel as corrosion progresses. The objective of this study is to apply the AE technique for early detection and evaluation of the extent of damage in RC structures under corrosion attack.

1.2 Research Objectives and Significance

Although the literature contains AE studies dealing with RC structures, there are no available relationships between the degree of degradation caused by reinforcement corrosion and AE parameters. Further studies are needed to investigate the feasibility of applying AE technique for monitoring severe corrosion progression taking into account the influences of cover thickness, sensor location, and specimen size on AE parameters. Research is also required to apply the AE intensity analysis as well as to examine the

feasibility of using the b-value analysis to quantify cover crack growth in RC structures considering the variations in corrosion level, cover thickness, sensors density, and specimen size. Meanwhile, limited studies investigated the application of AE monitoring for the concrete-steel bond of RC structures. The available reported literature also lacks information about AE monitoring of bond deterioration in existing RC structures prone to reinforcing steel corrosion.

The research project presented in this dissertation intended to use the AE data collected from a continuous SHM system to detect the early corrosion activity and to correlate these data to the degree of degradation (in terms of percentage of steel mass loss or crack width) due to corrosion. This research also aimed to implement the AE intensity analysis of signal strength for the identification of early stages of concrete-steel bond degradation and quantification of bond deterioration in corroded/un-corroded RC structures. The project also involved the development of damage classification charts that relate the extent of corrosion damage (in terms of steel mass loss, cover crack growth, and different stages of concrete-steel bond) to the AE parameters. Ultimately, the purpose of this research was to develop an effective AE based SHM system capable of maintaining the safety of new/existing RC structures.

1.3 Scope of Research

This research was conducted using a comprehensive experimental program consisted of four successive stages of tests on both small- and full-scale RC elements. The first and second stages of this research involved monitoring corrosion progression in RC samples via AE sensors. A total of 30 small-scale prism samples with various concrete cover

thicknesses and corrosion levels were examined in the first stage by means of accelerated corrosion tests. The analysis of AE data obtained from this preliminary stage was performed to achieve an early detection of corrosion activity in these samples before any visible damage. After corrosion propagation, the AE monitoring was continued in order to correlate the rate of cover crack growth resulting from corrosion to the collected AE signals. Accordingly, the second stage was implemented to verify the applicability of the results of the first stage to actual concrete structures. Five full-scale RC beams with two configurations were tested in the second stage under similar accelerated corrosion procedures to reach varied degrees of corrosion. The beams were monitored using distributed AE sensors to study the influence of sensor location on the ability of AE analysis to capture early corrosion occurrence as well as cover crack growth.

The third and fourth stages of this experimental setup were focused on the evaluation of bond behaviour of corroded/un-corroded small- and full-scale RC specimens. The investigation of bond behaviour in these stages was done to quantify the expected impact of corrosion of steel on the bond integrity between concrete and steel. The third stage investigated the feasibility of AE monitoring for identifying the successive stages of bond deterioration between concrete and steel. A series of pull-out tests on 114 small-scale prism samples were completed in the third stage. The effects of changing the bar diameter, corrosion level, cover thickness, and embedded length on different AE signal parameters were considered in the third stage. The AE results from this stage were analyzed so as to achieve an early indication of bond damage and characterize the extent of bond degradation in small-scale samples. Eventually, ten full-scale RC beams were used in the fourth stage to confirm the effectiveness of the AE monitoring in sensing bond

deterioration of concrete structures. This last stage involved testing corroded/un-corroded RC beams with various bonded lengths, corrosion levels, and sensor locations under four-point load setup. These beams were continuously monitored throughout the bond tests by multiple sensors to evaluate the effect of sensor position on the detection of bond damage. Following this extensive experimental program, the acquired AE data were undergone an intensity analysis of the AE signal strength from all tests. This analysis was utilized to generate additional AE parameters that can be correlated to all degrees of damage of the tested RC elements. The outcomes from this analysis were also exploited to develop damage classification charts for the purpose of quantification of damage resulting from corrosion of reinforcing steel and loss of bond between concrete and steel in concrete structures.

1.4 Thesis Outline

This thesis consists of eight chapters described as follows:

Chapter 1 demonstrates the background, motivation, objectives, significance, and scope of research conducted in this thesis.

Chapter 2 includes a review of the literature pertaining to the areas of SHM, corrosion of reinforcing steel, AE monitoring, and bond of reinforcement to concrete in RC structures.

Chapter 3 contains the detailed experimental program including the materials, test matrix, and methodology of the four stages of the experimental testing program.

Chapter 4 shows the discussions of the obtained results from the first stage of the experimental program regarding the corrosion detection and crack growth monitoring in small-scale RC samples.

Chapter 5 highlights the results and discussions of the findings of the second stage of the experimental testing about the corrosion detection and crack growth monitoring in full-scale RC beams.

Chapter 6 discusses the results of the third stage of tests dealing with the evaluation of concrete-steel bond behaviour of small-scale corroded/un-corroded RC samples.

Chapter 7 involves the results and discussions of the final stage of the experimental research concerning the evaluation of concrete-steel bond behaviour of full-scale corroded/un-corroded RC beams.

Chapter 8 presents the conclusions and recommendations from the completed research project.

2. Literature Review

2.1 Structural Health Monitoring (SHM) of Concrete Structures

Structural health monitoring (SHM) systems can be utilized to achieve real time non-destructive evaluation of concrete structures (Mufti et al., 2007; Lovejoy, 2008; Boller et al., 2009; Farhidzadeh et al., 2012). SHM systems have the advantage of real-time monitoring of civil structures, which prevents unforeseen structural failures (Staszewski et al., 2004; Giurgiutiu, 2008; Farhidzadeh et al., 2012). SHM of concrete structures has been implemented for the purpose of damage detection, quantification, and assessment of their remaining structural capacity. Examples of SHM sensors include; acoustic emission, chemical, electrochemical, and fiber optic sensors; guided waves; and strain gauges/displacement transducers. SHM systems were also employed for the aim of corrosion monitoring and detection of loss of bond in concrete structures, as explained in the following sections.

2.1.1 Corrosion Monitoring

A number of investigations applied SHM systems for the purpose of corrosion monitoring in RC structures. These studies developed different types of sensors and techniques capable of monitoring early stages of reinforcement corrosion. For instance, fibre optic strain sensors and electrical resistance gauges were utilized for monitoring the accumulation of corrosion by-products (Grattan et al., 2009). Nevertheless, strain based corrosion monitoring can only predict corrosion activity after corrosion starts, thus yielding higher costs of rehabilitation and retrofit. Another SHM technique for corrosion

detection exploited chemical sensors to measure chloride contents of concrete near the reinforcement surface (Lam et al., 2009). The results indicated the effectiveness and sensitivity of the proposed chloride sensors; however, there is a lack of information about the monitoring performance of such sensors when embedded into concrete. Recently, a novel nondestructive testing technique based on guided waves enabled the evaluation of the degree of rebar corrosion in aging concrete structures (Miller et al., 2012). However, this method cannot continuously predict the condition of bond between concrete and corroded steel.

2.1.2 Detection of Loss of Bond between Concrete and Reinforcement

One important application of SHM systems is the detection of bond deterioration between steel bars and concrete. A number of experimental studies aimed at the detection of delamination at the concrete-steel interface as well as internal defects in both corroded and un-corroded RC elements by means of guided waves (Jung et al., 2002; Na and Kundu, 2002; 2003; Na et al., 2002; 2003). More recently, different techniques have also been utilized to monitor de-bonding and/or bar slip in concrete structures (for instance: Wu and Chang 2006a; 2006b; Zhu et al., 2013; Ho et al., 2015; Wu et al., 2015). For example, Wu and Chang (2006a; 2006b) and Zhu et al. (2013) detected the de-bond damage between steel and concrete in beams/slabs by means of embedded piezoelectric sensors and actuators. The results of their investigation were then used to develop three indices to evaluate the bond loss. This technique, however, is considered an active SHM system that requires an external source for generating signals to be detected by sensors. In

addition, this method is not suitable for application in existing structures as it is based on embedded sensors (Zhu et al., 2013).

Another technique deployed fiber Bragg grating-based strain sensors to characterize bond slip in prestressed concrete bridge girders (Ho et al., 2015). This technique evaluated the local strain developed at different stages of bond slip until failure. On the other hand, an active ultrasonic guided wave-based system was developed for bond integrity assessment in reinforced concrete structures under pull-out tests (Wu et al., 2015). This active SHM system consisted of piezoelectric actuators and sensors mounted on the embedded steel bar in concrete. This system allowed for the early detection of bond splitting failure in reinforced concrete structures. A similar system, based on ultrasonic wave propagation using piezoelectric transducers attached to reinforced concrete samples, was developed (Rucka and Wilde, 2013). This technique was successful in detecting micro-cracking and moment before the onset of splitting cracks. However, this technique was not suitable for assessing the size of crack zones in their tested specimens. Thus, further research is needed to quantify the damage resulting from splitting cracks in reinforced concrete. An active sensing approach was recently developed using smart aggregates to detect bond slip between steel-plate and concrete (Qin et al., 2015).

2.2 Acoustic Emission (AE) Monitoring Technique

2.2.1 Overview of AE Signal Parameters

Different AE signal parameters have been considered for damage prognosis in concrete structures. These parameters include energy, amplitude, rise time, duration, and counts, as shown in **Figure 2.1**. In addition, other parameters of AE events such as signal strength

and number of detected hits can be used to describe the type of damage. Complete definitions of the AE signal parameters used in the nondestructive testing industry can be found elsewhere (ASTM E1316, 2014). Each parameter (or combination of parameters) can be assessed to identify and evaluate the level of damage occurring at the source of the recorded signal. The selection of the parameters to be monitored depends on the method of AE data analysis based on the type of application. One of the most important AE parameters is signal strength, which can be described as the measured area under the amplitude-time envelope, or the area below the envelope of the linear voltage time signal. Signal strength has units that are proportional to V-s (a constant specified by the AE instrument manufacturer) and usually includes the absolute area of both the positive and negative amplitude-time envelopes (ASTM E1316, 2014; ElBatanouny et al., 2014).

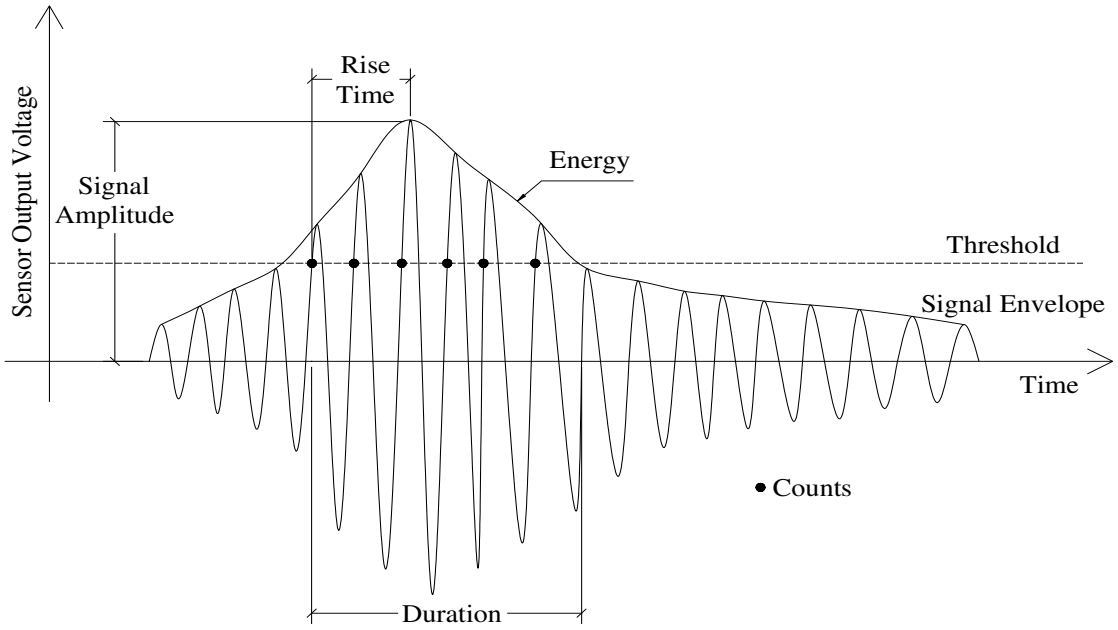

Figure 2.1 Typical AE signal parameters (Mistras Group, 2007)

2.2.2 Applications of AE Monitoring in Concrete Structures

AE monitoring has the advantage of continuous acquisition of signals released due to local damage in materials under stress (Ohtsu et al., 2002; Grosse et al., 2003; Ziehl, 2008; Ziehl et al., 2008; Benavent-Climent et al., 2009; Saboonchi and Ozevin, 2013). This technique was adopted in the literature and allowed the detection and identification of a wide variety of deteriorations in reinforced and prestressed concrete and masonry structures. Examples of these AE applications include: characterizing different sources of damage of RC beams tested under flexural loading (Yoon et al., 2000); evaluation of steel/CFRP bond (Matta et al., 2006); testing the flexural failure behaviour of RC beams with rebar corrosion (Okude et al., 2009); damage evaluation of RC exterior beam-column under cyclic loading (Benavent-Climent et al., 2009); structural assessment of concrete reinforced with chemically bonded anchors (Rizzo et al., 2010); damage assessment of RC slabs subjected to seismic loads (Benavent-Climent et al., 2011); detection of initial yield and failure of post-tensioned concrete beams (Salamone et al., 2012); evaluation of damage in RC bridge beams (Sagar et al., 2012); damage classification of RC beams (Aldahdooh and Bunnori, 2013; Shahidan et al., 2013); characterization of fracture mechanisms in concrete (Puri and Weiss, 2006; Mpalaskas et al., 2014); crack initiation detection in RC beams (Goszczyn´ska, 2014); identification of de-bonding in FRP-strengthened masonry (Ghiassi et al., 2014); corrosion damage detection of prestressed strands under tensile force (Ercolino et al., 2015); evaluation of strengthened reinforced concrete beams (Ridge and Ziehl, 2006); monitoring of alkali–silica reaction in concrete (Abdelrahman et al., 2015); in-situ evaluation of RC slabs and

prestressed beams (Ziehl et al., 2008; Abdelrahman et al., 2014; Di Benedetti and Nanni, 2014); and damage identification of CFRP-confined circular concrete-filled steel tubular columns (Li et al., 2015). The application of AE technology has also been extended to monitor corrosion in RC structures. Researchers tested the feasibility of using attached AE sensors to detect corrosion initiation in small-scale reinforced concrete samples (Ohtsu and Tomoda, 2008; Di Benedetti et al., 2013; 2014). The results from their experimental investigations showed that different analyses of AE parameters can be performed to detect the onset of corrosion. However, more tests are needed to validate the findings reported in their research and to develop relationships between the level of damage and AE signal parameters. More recently, AE-based SHM has been employed to identify the onset of corrosion in prestressed concrete bridge girders (ElBatanouny et al., 2014). The practical application of AE technique in SHM of RC bridges has also been investigated to assess the condition of in-service highway bridge structures (Lovejoy, 2008; Schumacher et al, 2011) and assess the residual strength of decommissioned concrete bridge beams with corroded pretensioned reinforcement (Rogers et al., 2012). The application of AE monitoring has also been extended to monitor real concrete and masonry buildings and multi-story reinforced concrete structures (Carpinteri et al., 2007; 2011).

2.2.3 Methods of AE Signal Analysis in Concrete Structures

Researchers have employed the raw AE signal parameters collected from continuous SHM systems to detect, quantify, and localize variable types of structural damage. For instance, the average frequency (count/time) and RA value (rise time/maximum

amplitude) have been applied to classify different forms of cracks in concrete structures (Ohtsu, 2010). This analysis proves the ability of AE analysis to differentiate between tensile or shear cracks resulting from external loads on structures. On the other hand, the history of cumulative signal strength (CSS) versus elapsed time in accelerated corrosion test was applied to detect the corrosion in prestressed concrete structures (ElBatanouny et al., 2014). CSS was also used to indicate the AE activity in RC slabs under in-situ loads (Ziehl et al., 2008). Alternatively, the cumulative number of hits was exploited to identify corrosion activity in reinforced concrete under accelerated corrosion tests (Li et al., 1998; Ohtsu and Tomoda, 2008).

Another analysis, called b-value analysis, was applied to represent the size distribution of AE sources and correlate it to the corrosion activity in reinforced concrete (Ohtsu and Tomoda, 2008). This analysis is a well-established method of analysis of AE data, which can assess the development of cracking in concrete structures. This analysis is based on seismic magnitude-frequency equations (Butt, 1996) and has been implemented on AE data collected from monitoring concrete structures (Colombo et al., 2003; Kurz et al., 2006; Sagar and Prasad, 2013; ElBatanouny et al., 2014; Li et al., 2015; Behnia et al., 2016). Yet, limited information is available in the literature about the utilization of the b-value analysis for the evaluation of corrosion-induced cracking in RC structures.

Further research was conducted to quantify damage in concrete structures using AE data by performing an intensity analysis (Degala et al., 2009; Mangual et al., 2013; Nair et al., 2014), which was first applied in fibre-reinforced polymer (FRP) vessels. In this analysis, two parameters (historic index and severity) are calculated based on signal strength values and are employed to assess the level of damage occurring in structures. This analysis was

further employed for the assessment of damage in prestressed concrete beams subjected to cyclic loading, corrosion detection of prestressing strands in full-scale beams and piles, and in situ evaluation of reinforced concrete slabs (Di Benedetti et al., 2014; ElBatanouny et al., 2014; Vélez et al., 2015). Eventually, the results from the intensity analysis were utilized to develop intensity classification charts to evaluate corrosion levels and measure the reduction in capacity of prestressed concrete elements. However, it is suggested that more research is required to validate and confirm the classification areas of these intensity classification charts. In addition, similar intensity classification charts are needed for the assessment of RC structures subjected to reinforcing steel corrosion.

2.3 AE Based Corrosion Monitoring of Reinforcing Steel in Concrete Structures

As previously mentioned, AE technique has been applied to monitor corrosion in RC structures (Li et al., 1998; Idrissi and Limam, 2003; Assouli et al., 2005; Ing et al., 2005; Ohtsu et al., 2011; Di Benedetti et al., 2013; Kawasaki et al., 2013; Patil et al., 2014). These experimental investigations have examined the feasibility of using attached AE sensors to detect corrosion of steel in small-scale RC samples. The outcomes from these experimental studies showed that different AE signal parameters can be analyzed to achieve early corrosion detection when compared to traditional nondestructive testing methods. The application of AE has also been extended to detecting corrosion of prestressed concrete small-scale samples (Elfergani et al., 2011; Mangual et al., 2013a; 2013b). The results obtained from these investigations showed the possibility of using AE signal parameters to characterize and quantify the extent of damage in prestressed concrete structures.

Fewer studies focused on utilizing AE monitoring of corrosion in full-scale concrete structures. Lu et al. (2013) exploited the AE monitoring using embedded cement-based piezoelectric sensors to assess the condition of RC beams under the coupled effect of corrosion and service loading. Nevertheless, this approach is not applicable in existing concrete structures owing to the utilization of embedded sensors. More recently, ElBatanouny et al. (2014) achieved an early detection of corrosion in both cracked/un-cracked prestressed concrete girders by means of AE monitoring. Likewise, Vélez et al. (2015) applied AE monitoring to obtain early corrosion recognition in full-scale portions of prestressed concrete piles exposed to accelerated corrosion. Most of these studies utilized AE intensity analysis for both damage identification and quantification of prestressed concrete structures due to corrosion (Mangual et al., 2013a; 2013b; ElBatanouny et al., 2014; Vélez et al., 2015). Nonetheless, further AE intensity analysis is required to quantify the extent of severe corrosion stages/cover crack growth in concrete structures considering the effects of corrosion level and cover thickness. The literature also lacks information regarding corrosion monitoring of large-size RC beams using AE technique. Moreover, no available quantitative data about AE monitoring of corrosion damage progression in existing RC structures exposed to severe levels of corrosion (following corrosion onset).

2.4 Concrete-Steel Bond Behaviour in Concrete Structures

Reinforced concrete (RC) structures are designed and constructed to ensure that a perfect bond between concrete and steel is maintained throughout its service lifetime. This bond allows the transfer of longitudinal forces from steel to concrete and ensures the composite

action within RC elements (ACI Committee 408, 2003; Nilson et al., 2010). The concrete-steel bond strength depends on a number of parameters including material and structural factors. In addition, different requirements are specified in building codes in order to design concrete structures that avoid bond failures. However, the performance of this bond may be affected when RC structures are exposed to excessive repeated loading and/or severe environmental conditions. For instance, corrosion of embedded reinforcement can minimize the bond strength of RC structures, thus affecting serviceability and overall strength (Auyeung et al., 2000; ACI Committee 222, 2001; Fang et al., 2006). As a result, continuous monitoring of the integrity of the steel-to-concrete bond is essential to prevent any sudden failure of concrete structures.

Researchers mostly used the pull-out test specimens for evaluating bond behaviour of concrete structures due to the simplicity of fabricating those test specimens (ACI Committee 408, 2003; Gallego et al., 2015; Park et al. 2016). On the other hand, flexural bond tests similar to those performed by Ju and Oh (2015) can be adopted, which are considered to be more representative to the stress states of RC structures subjected to flexure (ACI Committee 408, 2003). Meanwhile, anchorage beam specimens are considered to represent realistic bond behaviour of full-size reinforced concrete structures (ACI Committee 408, 2003; Rilem-Fip-Ceb, 1973; Soudki et al., 2007).

2.5 AE Monitoring of Concrete-Steel Bond in Concrete Structures

It has been confirmed that AE monitoring is a strong tool to detect micro-cracking of materials and structures under stresses (Pollock, 1986; Fowler et al., 1989). Early stages of bond loss between concrete and steel are known to be associated with the initiation of

micro-cracking at the concrete-steel interface (CEB-FIP, 2000; Gallego et al., 2015). The initiation of micro-cracks and crack growth are both considered to be among the possible sources of emission of AE signals (Fowler et al., 1989; Fowler et al., 1998). For this reason, Iwaki et al. (2003) and Gallego et al. (2015) exploited this capability of AE monitoring to characterize the bond behaviour of RC samples cast with different concrete and reinforcement materials under pull-out tests. Iwaki et al. (2003) applied AE monitoring in reinforced concrete under pull-out tests to investigate the influence of concrete compaction on the bond behaviour of reinforced concrete elements. The results indicated the feasibility of analyzing AE activity (in terms of cumulative number of hits) to detect the locations of insufficient bond and slippage of steel bars. More recently, the bond behaviour of black and galvanized deformed steel in concrete subjected to pull-out tests was evaluated using AE monitoring (Gallego et al., 2015). The analysis of AE activities (cumulative number of hits) reflected different stages of bond degradation and differentiated between the behaviour of different types of steel (Gallego et al., 2015). It can be concluded that the effects of other factors, including bar diameter, bar confinement, cover thickness, and development length on different AE signal parameters, have not yet been investigated. Meanwhile, there is a lack of research dealing with the utilization of AE monitoring for the evaluation of bond behaviour of corroded reinforcement to concrete. Moreover, the implementation of AE monitoring for the evaluation of bond behaviour in full-scale RC structures has not yet been examined.

It conclusion, this literature review indicated that AE monitoring is a useful tool for both damage detection and quantification in concrete structures under different damage mechanisms. However, some gaps in knowledge of AE technique still exist especially in

using AE monitoring for corrosion damage quantification and bond damage detection/evaluation. The work presented in this thesis aimed at addressing these gaps in the AE knowledge to eventually use AE monitoring as a feasible SHM tool.

3. Experimental Program

3.1 Introduction

The experimental program conducted in this research is described in detail in this chapter. This experimental program involved four consecutive stages of experiments, as will be explained in the following sections.

3.2 Materials and Concrete Mixture Properties

In all experimental investigations, small- and full-scale RC samples were constructed and tested. All samples were constructed using one normal concrete mixture and ordinary deformed reinforcing steel bars. This concrete mixture contained type GU Canadian Portland cement, similar to ASTM Type I (ASTM, 2012a), with a specific gravity of 3.15. Natural sand and 10 mm maximum size stone were incorporated into the mixture as fine and coarse aggregates, respectively. Both coarse and fine aggregates had a specific gravity of 2.60 and water absorption of 1%. The 28-day compressive strength of concrete was obtained by testing six cylindrical samples as per ASTM C39 (ASTM, 2012b). Moreover, the splitting tensile strength of six additional cylindrical specimens was determined based on ASTM C496 (ASTM, 2011a), as seen in **Table 3.1**. Carbon steel bars with three variable diameters (10, 20, and 35 mm) were used in the tested samples. All reinforcing steel bars have an average yield stress of 480 MPa and tensile strength of 725 MPa. The mixture properties and 28-day compressive/tensile strength results of the concrete mixture are shown in **Table 3.1**.

Table 3.1 Concrete mixture proportions and 28-day compressive/tensile strength

Cement (kg/m^3)	10 mm stone (kg/m^3)	Sand (kg/m^3)	Water (kg/m^3)	28-day compressive strength (MPa)	28-day splitting tensile strength (MPa)
350	1168.27	778.84	140	f_c = 36.93	f_{ct} = 3.79

3.3 Experimental Study 1: Corrosion Detection and Crack Growth Monitoring Using AE Sensors in Small-Scale RC Samples

In this study, 30 small-scale reinforced concrete prism samples were subjected to an accelerated corrosion test and the rate of corrosion was continuously monitored using AE sensors (**Figure 3.1**). The samples were exposed to corrosion using an impressed current accelerated corrosion test until reaching variable levels of damage. These different degrees of damage were estimated based on the theoretical mass loss of steel, including 1%, 2%, 3%, 4%, and 5%. Two identical samples were tested at each degree of mass loss to confirm the repeatability of the test results. The selected levels of mass loss were presumed, based on reviewing the literature, to obtain the range of the critical corrosion degree that causes cover cracking in reinforced concrete structures. This literature review showed that a critical range of 0.8% to 5.6% of steel mass loss may induce cover cracking ranges between 10 mm and 50 mm (Oh et al., 2009; Otieno et al., 2010). The targeted values of the theoretical mass loss of steel in all tested samples were calculated by applying Faraday's law (**Equation 3.1**).

$$Mass\ Loss = \frac{t\,.\,i\,.\,M}{z\,.\,F} \qquad \textbf{(3.1)}$$

Where: t = the time passed (s); i = the current passed (Ampere); M = atomic weight (for steel: M = 55.847 g/mol); z = ion charge (2 moles of electrons); and F = Faraday's constant (F = 96485 coulombs per mole (C/mol)).

3.3.1 Description of Test Specimens

These prism samples were constructed with three different concrete covers (20, 30, 40 mm) around one embedded steel bar at the centre of each prism. The dimensions of the prisms were as follows: 60 x 60 x 250 mm for the 20 mm cover, 80 x 80 x 250 mm for the 30 mm cover, and 100 x 100 x 250 mm for the 40 mm cover samples. The length of the steel rebar was varied: 210, 190, and 170 mm for 20, 30, and 40 mm cover samples, respectively, to keep a constant cover in all directions. On the other hand, the length of all samples was kept constant at 250 mm to facilitate the construction of multiple prisms using the same formwork. All samples were cured in water for a period of 28 days before the corrosion testing. The tested samples were designated according to the concrete cover (20, 30, 40 mm), percentage of steel mass loss (1%, 2%, 3%, 4%, and 5%), and replicate number (1, 2). For instance, the first replicate of the prism sample cast with concrete cover of 30 mm and exposed to 3% steel mass loss is identified as 30-3-1.

3.3.2 Accelerated Corrosion Test Procedure

All tested samples were subjected to an electrically accelerated corrosion test, as shown in **Figure 3.1**. A constant voltage (12 V) was applied to all tested samples during the test. The prism samples were partially submerged in a plastic container filled with a 5% NaCl water solution. The embedded steel bar in each sample was connected as an anode (+) in a direct current (DC) power supply, whereas a stainless steel mesh was placed underneath all samples to act as a cathode (–). The amount of the electric current passing in each sample was constantly monitored and recorded at one-minute intervals using a data-acquisition system. Based on the recorded values of the electric current and passed time,

the predicted percentage of steel mass loss was calculated using **Equation 3.1** until the target values were reached. The half-cell potential (HCP) difference between the embedded steel bar and a $Cu/CuSO_4$ reference electrode (copper-copper sulfate reference cell electrode) was measured on a daily basis according to ASTM C876 standard test (ASTM, 1991) to determine the probability of corrosion activity. The location of the reference cell at the surface of the concrete was kept constant throughout all tests. The samples were also visually inspected on a daily basis to detect the concrete cover cracking and to measure the crack widths by means of a crack-width-measuring microscope. The test was ended for each sample after reaching the previously assumed degrees of steel mass loss (1 to 5%). The percentage of steel mass loss was verified at the end of the test by breaking the samples and weighing the steel bar to obtain the actual mass loss, as per ASTM G1 standard method (ASTM, 2011b).

(a)

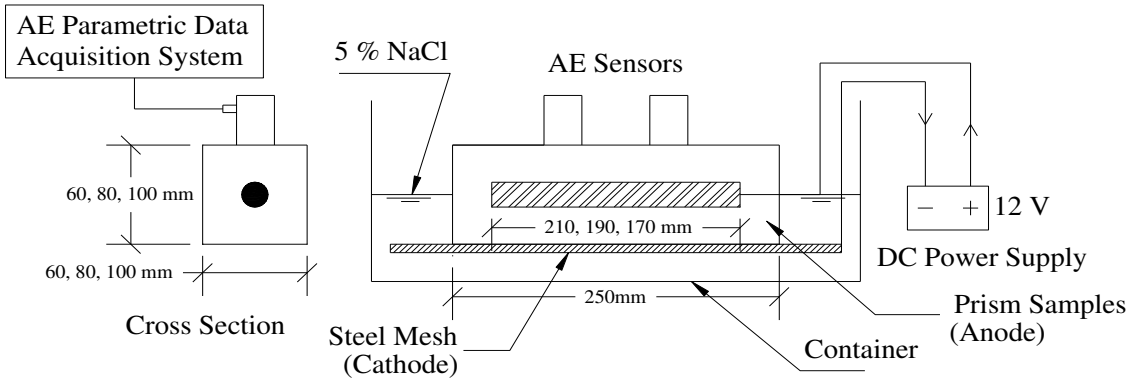

(b)

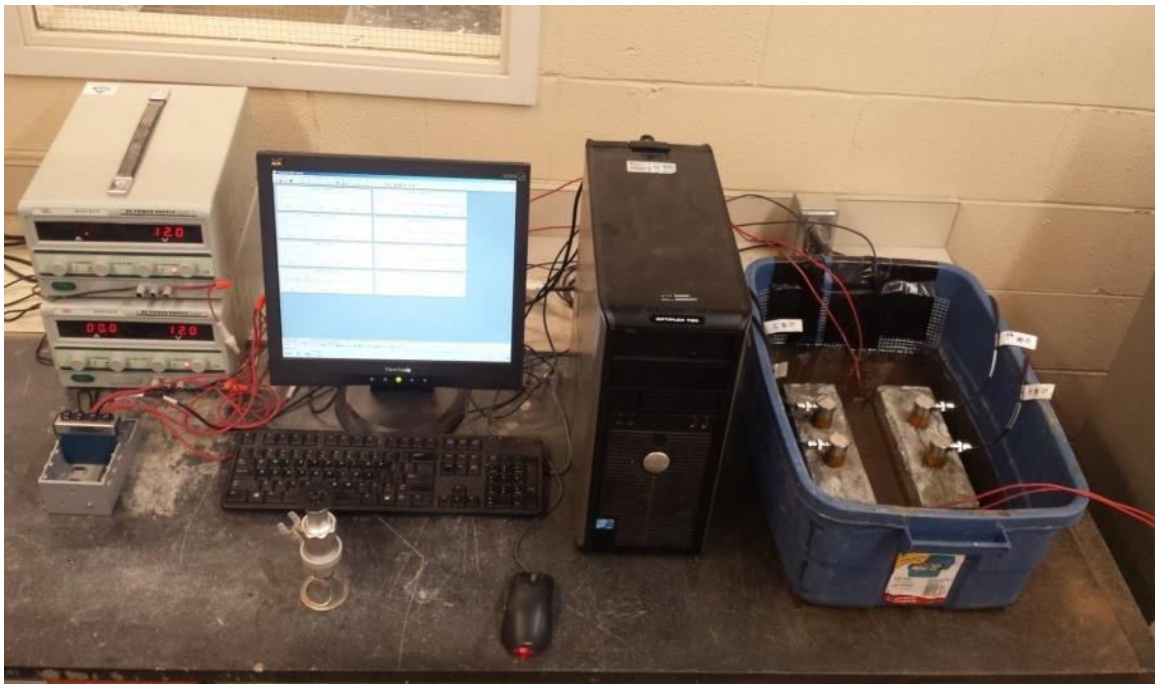

Figure 3.1 Accelerated corrosion test and AE monitoring setup: (a) schematic and (b) picture of typical experiment

3.3.3 AE Monitoring Setup

The acoustic emissions, resulting from the steel corrosion/cover crack growth in each sample during the accelerated corrosion test, were monitored using two piezoelectric AE sensors (Physical Acoustics, 2005) with integral preamplifier (R6I-AST). These sensors were selected due to their high sensitivity and low resonant frequency, which make them suitable for many applications, such as metal, FRP, and concrete structures in petroleum, refineries, chemical plants, and offshore platforms (Physical Acoustics, 2005). These sensors were utilized in some available studies from the literature dealing with corrosion of steel/prestressing tendons in concrete structures (Di Benedetti et al., 2013; Mangual et al., 2013a; 2013b; ElBatanouny et al., 2014; Vélez et al., 2015). These sensors were

mounted on each specimen on the top of the steel bar (**Figure 3.1**). The sensors were attached to the top of the specimen using an epoxy adhesive. It can be seen from **Figure 3.1** that the sensors were not exposed to direct contact with the chloride solution in the container. For field applications, it is therefore recommended to protect the sensors from different environmental exposures to obtain similar results. The reinforcing steel corrosion rate was continuously monitored for all tested samples using 4-channel AE data acquisition system and AEwin signal processing software (Mistras Group, 2007). An amplitude threshold value of 40 dB was used for the collected AE data. Any signal voltage exceeding this threshold value was recorded using the AE data acquisition system (Di Benedetti et al., 2013). **Table 3.2** shows a summary of the specifications of the sensors along with the features and filters selected in the data acquisition hardware. Different AE signal parameters were selected to be collected during the test including amplitude, energy, counts, rise time, duration, signal strength, absolute energy, and frequency. In this study, only the results of signal strength are presented and subjected to further analysis. A similar procedure was successfully employed for corrosion monitoring in both reinforced and prestressed concrete structures (Di Benedetti et al., 2013; Mangual et al., 2013a; 2013b; ElBatanouny et al., 2014).

Table 3.2 AE sensors specifications and data acquisition system setup (Mistras Group, 2005; 2007)

R6I-AST sensor specifications		AE hardware setup	
Integral preamplifier	40 dB	Threshold	40 dB_{AE}
Peak sensitivity, Ref V/(m/s)	117 dB	Sample rate	1 MSPS
Peak sensitivity, Ref V/µbar	-23 dB	Pre-trigger	256 µs
Operating frequency range	40-100 kHz	Length	1k points
Resonant frequency, Ref V/(m/s)	55 kHz	Preamp gain	40 dB
Resonant frequency, Ref V/µbar	98 kHz	Preamp voltage	28
Directionality	+/-1.5 dB	Analog filter	1-50 kHz
Temperature range	-35 to 75ºC	Digital filter	100-400 kHz
Dimensions	29 mm diameter x 40 mm height	PDT	200 µs
Case material	Stainless steel	HDT	800 µs
Face material	Ceramic	HLT	1000 µs
Weight	98 grams	Maximum duration	1000 µs

3.4 Experimental Study 2: Corrosion Detection and Crack Growth Monitoring Using AE Sensors in Full-Scale RC Beams

The results obtained from the experimental study 1 proved the feasibility of AE monitoring technique to detect/assess corrosion damage and cover crack growth in small-scale RC prism samples. The aim of this stage was to verify these results by testing full-scale corroded RC beams, which can be more representative to actual concrete structures.

3.4.1 Details of Corroded Beams

Five RC full-scale beams were constructed with two configurations: 250 x 250 x 1500 mm and 250 x 250 x 2440 mm were exposed to accelerated corrosion procedures to reach higher corrosion levels (5, 10, 20, and 30% of steel mass loss). These beams were also

used in bond testing in study 4, thus were designed to ensure bond failure. To promote bond failure, the anchorage lengths of all five beams were chosen as 200 mm to be less than the minimum development length as specified by the Canadian Standard Association (CSA) standard (Soudki et al., 2007; CSA, 2014). Each beam specimen was reinforced with two 20M steel bars as main reinforcement with 10M stirrups with the configuration presented in **Figure 3.2**. Two additional 10M bars were provided to hold the stirrups in each beam sample. The main reinforcement rebar were partially bonded in the anchorage zones by adding PVC pipe (bond breaker) in the middle part of each beam. The main reinforcement included two protruding parts to permit the measurement of the free end bar slip at the two beam ends (**Figure 3.2**). The dimensions of beams B1, B2, B3, and B4 were identical (250 x 250 x 1500 mm) and were corroded to 5, 10, 20, and 30% of steel mass lass, respectively. Meanwhile, B5 was cast the same cross section (250 x 250 mm), but with an extended length (2440 mm) and were corroded to 30% of steel mass lass. Concrete was poured in wooden formwork with the main reinforcing bars are horizontally placed at the bottom of the formwork. The compaction of all beams was done by means of mechanical vibration. The beams specimens were de-molded after 24 hours of casting and then water-cured for a period of 28 days before corrosion exposure.

3.4.2 Accelerated Corrosion Test Setup

In this investigation, an electrically accelerated corrosion test was implemented so as to induce severe corrosion levels in a reasonable time frame. The test was performed using a constant electrical current (0.1 A) and varied corrosion period obtained by Faraday's law (**Equation 3.1**) to reach variable degrees of steel mass loss. The beams were subjected to

corrosion at only one side along the bonded length (200 mm) of the two 20M main steel bars (**Figure 3.2**) to represent localized corrosion condition. As being upside down, one end of each beam was exposed to a 5% NaCl water solution by means of a hard foam tank attached to the top of the beam surface along the bonded length. Both the 20M steel bars in each beam were connected to two DC power supplies acting as anodes (+). In addition, a stainless steel mesh was positioned at the bottom of the foam tank to serve as cathodes (–). Throughout the corrosion tests, the half-cell potential (HCP) test was daily executed and visual inspection of corrosion cracking was daily monitored. The HCP test was performed in accordance with the ASTM standard test method (ASTM, 1999). As soon as the corrosion cracks were identified, the crack width measurements were also daily obtained by means of a crack measuring microscope. The final corrosion crack widths were recorded at the end of the corrosion tests for the aim of correlation with the AE data. Besides, the actual percentages of steel mass loss were verified following the bond testing after breaking all beams and weighing the corroded steel bars according to ASTM G1 (ASTM, 2011b).

(a)

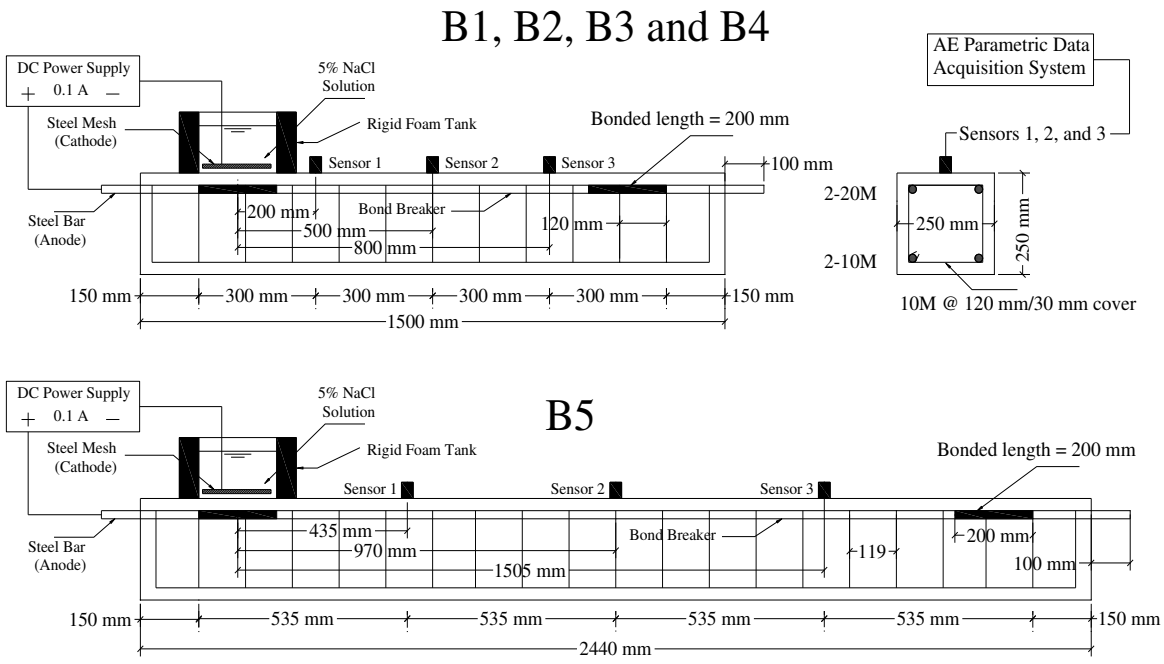
B1, B2, B3 and B4
DC Power Supply
+ 0.1 A –
5% NaCl Solution
Steel Mesh (Cathode)
Rigid Foam Tank
Bonded length = 200 mm
AE Parametric Data Acquisition System
Sensors 1, 2, and 3
Sensor 1
Sensor 2
Sensor 3
100 mm
Steel Bar (Anode)
200 mm
Bond Breaker
500 mm
800 mm
120 mm
2-20M
2-10M
250 mm
250 mm
150 mm
300 mm
300 mm
300 mm
300 mm
150 mm
1500 mm
10M @ 120 mm/30 mm cover
B5
DC Power Supply
+ 0.1 A –
5% NaCl Solution
Steel Mesh (Cathode)
Rigid Foam Tank
Bonded length = 200 mm
Sensor 1
Sensor 2
Sensor 3
Steel Bar (Anode)
435 mm
970 mm
1505 mm
Bond Breaker
119
200 mm
100 mm
150 mm
535 mm
535 mm
535 mm
535 mm
150 mm
2440 mm

(b)

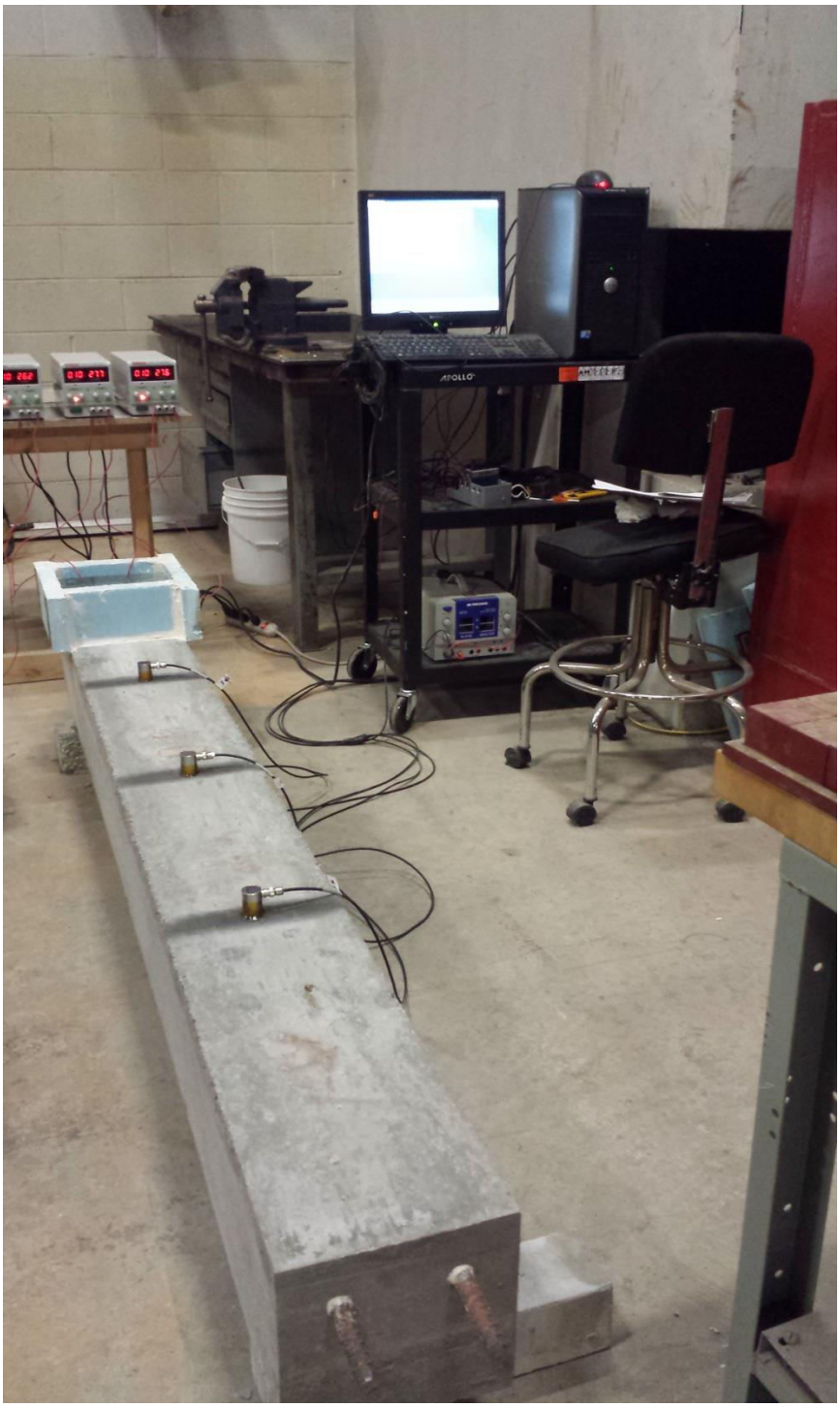

Figure 3.2 Accelerated corrosion test and AE monitoring setup: (a) schematic and (b) picture of the typical experiment of B5

3.4.3 AE Monitoring Setup

In this study, each tested beam was monitored through the accelerated corrosion test via three AE sensors (**Figure 3.2**). These sensors were attached to the top side of the beam surface at the centre line of the beam cross section by a two-part epoxy adhesive (**Figure 3.2**). These sensors were distributed at three varied distances from the corroded side of the beam. The configuration of the sensors was designed to examine the effect of sensor location on the ability of AE monitoring in detecting/assessing corrosion initiation, propagation, and cover crack growth in large-scale RC structures. The sensors used in this study, AE data acquisition system, and AE signal parameters had all exactly the same setup of that employed in study 1.

3.5 Experimental Study 3: Evaluation of Concrete-Steel Bond Behaviour Using AE Sensors in Small-Scale Corroded/Un-Corroded RC Samples

In this stage, the concrete-steel bond behaviour of a total of 114 small-scale RC prism samples was examined with AE monitoring during pull-out tests. These samples included 60 previously corroded and 54 un-corroded samples with variable bar diameter, corrosion level, concrete cover thickness and embedded length. The description of these samples and tests setup are as follows:

3.5.1 Details of Pull-out Prism Samples

One reinforcing steel bar was partially embedded in each prism sample (corroded and un-corroded) with one protruding end to enable the pull-out testing (**Figure 3.3**). These samples had three variable concrete cover thicknesses (20, 30, and 40 mm) around the

embedded steel bar. The clear concrete cover was maintained constant around the steel bar on all sides of each sample. The concrete dimensions of the samples were changed based on the value of the cover thickness. After mixing, concrete was poured in wooden formwork with the reinforcing bars in a horizontal casting position. Sufficient compaction of all formwork was achieved by using mechanical vibration. After 24 hours of mixing, the specimens were de-molded and then water-cured for a period of 28 days before corrosion exposure or pull-out testing. The bottom ends of all samples were filled with waterproof silicon to insulate the steel bar and avoid the direct connection to water in the accelerated corrosion period. This filling was removed from all samples at the end of corrosion exposure to allow the measurement of free end bar slippage in the pull-out test. Two identical samples were prepared from each specimen, at the same degree of steel mass loss, to ensure the repeatability of the results.

3.5.1.1 Corroded Samples

A total of 60 samples were exposed to an accelerated corrosion process (similar to that completed in study 1) until they reached five different degrees of theoretical steel mass loss: 1%, 2%, 3%, 4%, and 5% (**Figure 3.3**). The corroded prism samples were cast with 20 mm diameter (20M) bars and two values of bonded length (50 and 200 mm). Each sample had two PVC pipes acting as bond breakers placed before and after the bonded length. The bonded length was changed from 200 to 100 or 50 mm by extending the length of the PVC pipe from the bottom end of the sample (**Figure 3.3**). The test matrix, complete dimensions, and results of accelerated corrosion tests of all corroded samples are presented in **Table 3.3**.

(a)

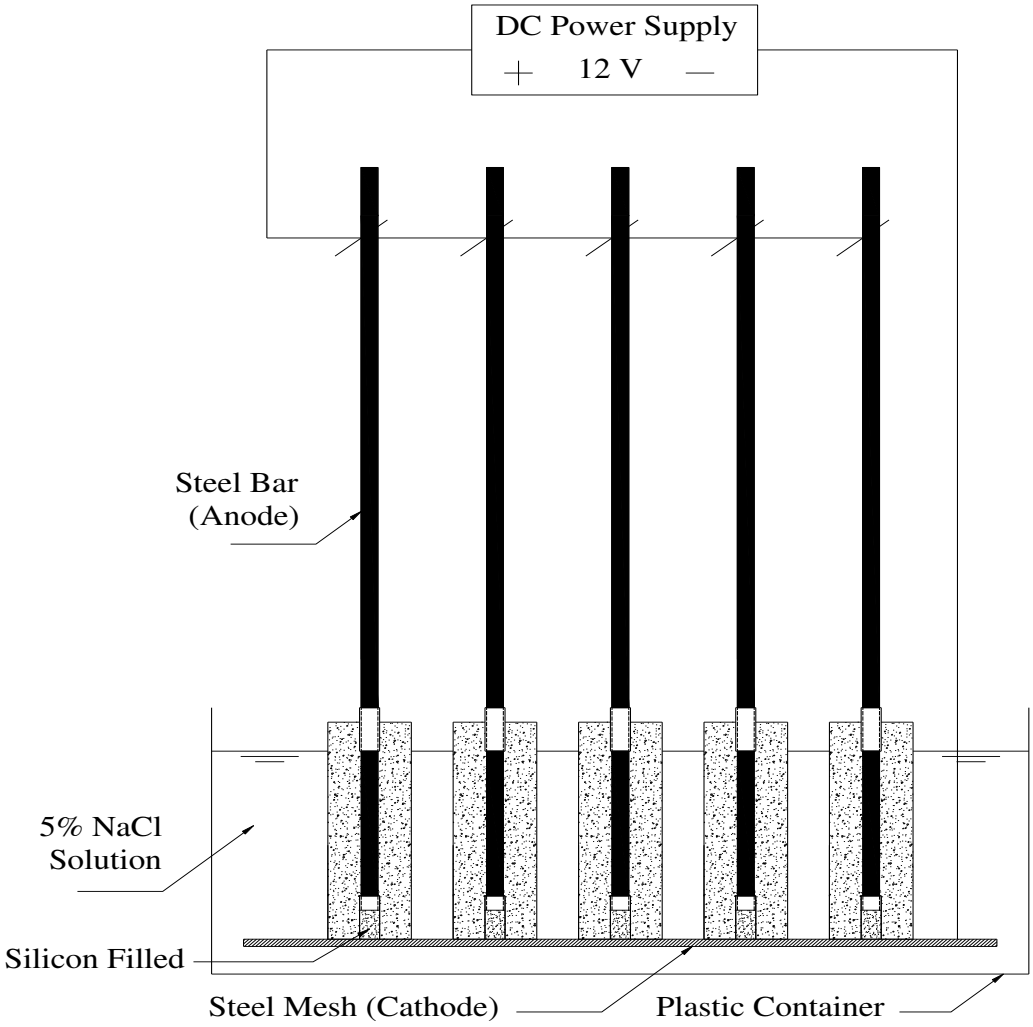
DC Power Supply
+ 12 V —
Steel Bar
(Anode)
5% NaCl
Solution
Silicon Filled
Steel Mesh (Cathode)
Plastic Container

(b)

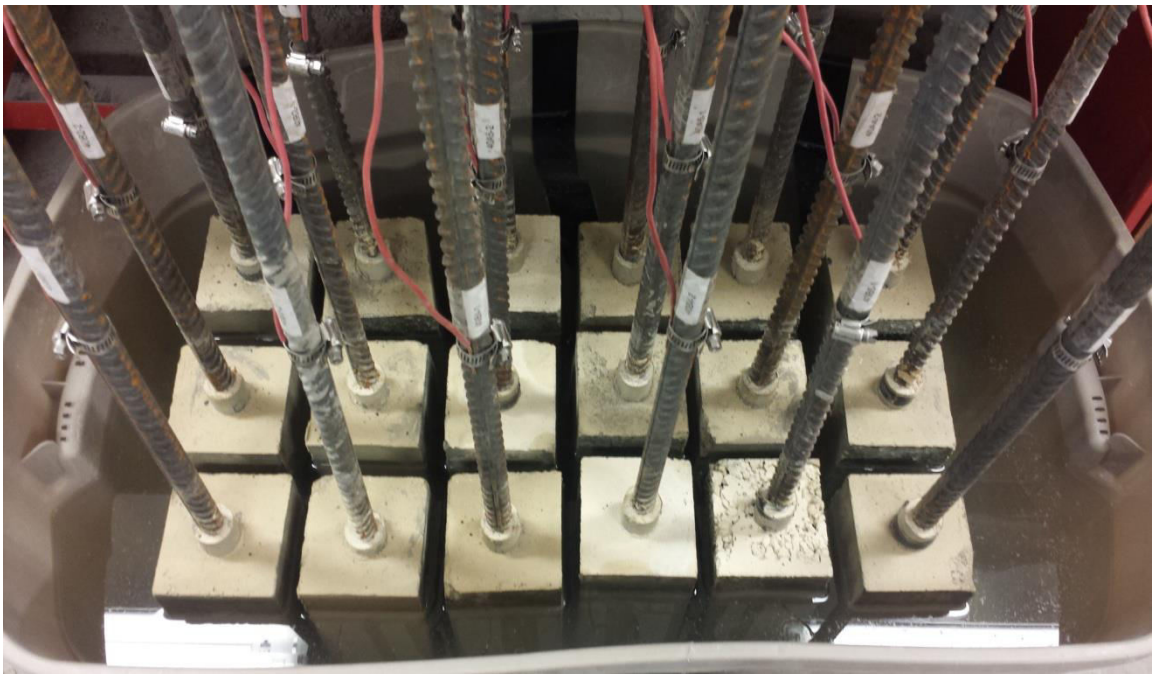

Figure 3.3 Typical accelerated corrosion setup: (a) schematic and (b) picture of typical experiment

Table 3.3 Corroded specimens details and accelerated corrosion results

Sample number	Sample designation	Cover thickness (mm)	Embedded length (mm)	Theoretical steel mass loss (%)	Dimensions (mm x mm x mm)
1	20M20A1-1	20	50	1	60 x 60 x 260
2	20M20A1-2	20	50	1	60 x 60 x 260
3	20M20C1-1	20	200	1	60 x 60 x 260
4	20M20C1-2	20	200	1	60 x 60 x 260
5	20M20A2-1	20	50	2	60 x 60 x 260
6	20M20A2-2	20	50	2	60 x 60 x 260
7	20M20C2-1	20	200	2	60 x 60 x 260
8	20M20C2-2	20	200	2	60 x 60 x 260
9	20M20A3-1	20	50	3	60 x 60 x 260
10	20M20A3-2	20	50	3	60 x 60 x 260
11	20M20C3-1	20	200	3	60 x 60 x 260
12	20M20C3-2	20	200	3	60 x 60 x 260
13	20M20A4-1	20	50	4	60 x 60 x 260

14	20M20A4-2	20	50	4	60 x 60 x 260
15	20M20C4-1	20	200	4	60 x 60 x 260
16	20M20C4-2	20	200	4	60 x 60 x 260
17	20M20A5-1	20	50	5	60 x 60 x 260
18	20M20A5-2	20	50	5	60 x 60 x 260
19	20M20C5-1	20	200	5	60 x 60 x 260
20	20M20C5-2	20	200	5	60 x 60 x 260
21	20M30A1-1	30	50	1	80 x 80 x 280
22	20M30A1-2	30	50	1	80 x 80 x 280
23	20M30C1-1	30	200	1	80 x 80 x 280
24	20M30C1-2	30	200	1	80 x 80 x 280
25	20M30A2-1	30	50	2	80 x 80 x 280
26	20M30A2-2	30	50	2	80 x 80 x 280
27	20M30C2-1	30	200	2	80 x 80 x 280
28	20M30C2-2	30	200	2	80 x 80 x 280
29	20M30A3-1	30	50	3	80 x 80 x 280
30	20M30A3-2	30	50	3	80 x 80 x 280
31	20M30C3-1	30	200	3	80 x 80 x 280
32	20M30C3-2	30	200	3	80 x 80 x 280
33	20M30A4-1	30	50	4	80 x 80 x 280
34	20M30A4-2	30	50	4	80 x 80 x 280
35	20M30C4-1	30	200	4	80 x 80 x 280
36	20M30C4-2	30	200	4	80 x 80 x 280
37	20M30A5-1	30	50	5	80 x 80 x 280
38	20M30A5-2	30	50	5	80 x 80 x 280
39	20M30C5-1	30	200	5	80 x 80 x 280
40	20M30C5-2	30	200	5	80 x 80 x 280
41	20M40A1-1	40	50	1	100 x 100 x 300
42	20M40A1-2	40	50	1	100 x 100 x 300
43	20M40C1-1	40	200	1	100 x 100 x 300
44	20M40C1-2	40	200	1	100 x 100 x 300
45	20M40A2-1	40	50	2	100 x 100 x 300
46	20M40A2-2	40	50	2	100 x 100 x 300
47	20M40C2-1	40	200	2	100 x 100 x 300
48	20M40C2-2	40	200	2	100 x 100 x 300
49	20M40A3-1	40	50	3	100 x 100 x 300
50	20M40A3-2	40	50	3	100 x 100 x 300
51	20M40C3-1	40	200	3	100 x 100 x 300

52	20M40C3-2	40	200	3	100 x 100 x 300
53	20M40A4-1	40	50	4	100 x 100 x 300
54	20M40A4-2	40	50	4	100 x 100 x 300
55	20M40C4-1	40	200	4	100 x 100 x 300
56	20M40C4-2	40	200	4	100 x 100 x 300
57	20M40A5-1	40	50	5	100 x 100 x 300
58	20M40A5-2	40	50	5	100 x 100 x 300
59	20M40C5-1	40	200	5	100 x 100 x 300
60	20M40C5-2	40	200	5	100 x 100 x 300

3.5.1.2 Un-Corroded Samples

As previously noted, 54 un-corroded samples were tested in this study in order to investigate the effects of bar diameter, concrete cover, and embedded length on the bond behaviour and resulting AE signals in the pull-out tests. The un-corroded samples were cast with three diameters of the reinforcing bars: 10 mm (10M), 20 mm (20M), and 35 mm (35M) bars and three varied bonded lengths: 50, 100, and 200 mm. The detailed dimensions of all un-corroded prism samples are tabulated in **Table 3.4**. All samples (corroded and un-corroded) were designated according to bar diameter (10M, 20M, 35M), concrete cover (20, 30, and 40 mm), embedded length (A for 50 mm, B for 100 mm and C for 200 mm), percentage of theoretical steel mass loss (0%, 1%, 2%, 3%, 4%, and 5%), and replicate number (1, 2). For example, the first replicate of a sample cast with 20M bar, 30 mm cover, 200 mm embedded length, and corroded to 3% of steel mass loss is denoted as 20M30C3-1.

Table 3.4 Test matrix and un-corroded specimens dimensions

Sample number	Sample designation	Bar diameter (mm)	Cover thickness (mm)	Embedded length (mm)	Dimensions (mm x mm x mm)
1	10M20A0-1	10	20	50	50 x 50 x 240
2	10M20A0-2	10	20	50	50 x 50 x 240
3	10M20B0-1	10	20	100	50 x 50 x 240
4	10M20B0-2	10	20	100	50 x 50 x 240
5	10M20C0-1	10	20	200	50 x 50 x 240
6	10M20C0-2	10	20	200	50 x 50 x 240
7	20M20A0-1	20	20	50	60 x 60 x 240
8	20M20A0-2	20	20	50	60 x 60 x 240
9	20M20B0-1	20	20	100	60 x 60 x 240
10	20M20B0-2	20	20	100	60 x 60 x 240
11	20M20C0-1	20	20	200	60 x 60 x 240
12	20M20C0-2	20	20	200	60 x 60 x 240
13	35M20A0-1	35	20	50	75 x 75 x 240
14	35M20A0-2	35	20	50	75 x 75 x 240
15	35M20B0-1	35	20	100	75 x 75 x 240
16	35M20B0-2	35	20	100	75 x 75 x 240
17	35M20C0-1	35	20	200	75 x 75 x 240
18	35M20C0-2	35	20	200	75 x 75 x 240
19	10M30A0-1	10	30	50	70 x 70 x 260
20	10M30A0-2	10	30	50	70 x 70 x 260
21	10M30B0-1	10	30	100	70 x 70 x 260
22	10M30B0-2	10	30	100	70 x 70 x 260
23	10M30C0-1	10	30	200	70 x 70 x 260
24	10M30C0-2	10	30	200	70 x 70 x 260
25	20M30A0-1	20	30	50	80 x 80 x 260
26	20M30A0-2	20	30	50	80 x 80 x 260
27	20M30B0-1	20	30	100	80 x 80 x 260
28	20M30B0-2	20	30	100	80 x 80 x 260
29	20M30C0-1	20	30	200	80 x 80 x 260
30	20M30C0-2	20	30	200	80 x 80 x 260
31	35M30A0-1	35	30	50	95 x 95 x 260
32	35M30A0-2	35	30	50	95 x 95 x 260
33	35M30B0-1	35	30	100	95 x 95 x 260
34	35M30B0-2	35	30	100	95 x 95 x 260
35	35M30C0-1	35	30	200	95 x 95 x 260

36	35M30C0-2	35	30	200	95 x 95 x 260
37	10M40A0-1	10	40	50	90 x 90 x 280
38	10M40A0-2	10	40	50	90 x 90 x 280
39	10M40B0-1	10	40	100	90 x 90 x 280
40	10M40B0-2	10	40	100	90 x 90 x 280
41	10M40C0-1	10	40	200	90 x 90 x 280
42	10M40C0-2	10	40	200	90 x 90 x 280
43	20M40A0-1	20	40	50	100 x 100 x 280
44	20M40A0-2	20	40	50	100 x 100 x 280
45	20M40B0-1	20	40	100	100 x 100 x 280
46	20M40B0-2	20	40	100	100 x 100 x 280
47	20M40C0-1	20	40	200	100 x 100 x 280
48	20M40C0-2	20	40	200	100 x 100 x 280
49	35M40A0-1	35	40	50	115 x 115 x 280
50	35M40A0-2	35	40	50	115 x 115 x 280
51	35M40B0-1	35	40	100	115 x 115 x 280
52	35M40B0-2	35	40	100	115 x 115 x 280
53	35M40C0-1	35	40	200	115 x 115 x 280
54	35M40C0-2	35	40	200	115 x 115 x 280

3.5.2 Pull-out Test Setup

All samples (corroded and un-corroded) were tested under direct pull-out tests in a universal testing machine, as described in **Figure 3.4**. These prism samples were loaded under an incrementally increasing monotonic loading condition until bond failure. The free end slip of the steel bar of each specimen was obtained using one linear variable differential transformer (LVDT) mounted at the top of each sample (**Figure 3.4**). The magnitude of loading and the corresponding free end slip measured using the LVDT in each sample were constantly acquired by a data-acquisition system.

3.5.3 AE Monitoring Setup

Each tested sample was monitored during the pull-out test by two piezoelectric AE sensors, as shown in **Figure 3.4**. The AE sensors were attached, using a two-part epoxy adhesive, to one side of each sample's surface located at the centre of the embedded steel bar. All AE signals emitted through the test were continuously recorded via a 4-channel AE data-acquisition system and AEwin signal processing software. The data-acquisition system was exactly set up as explained in studies 1 and 2.

(a)

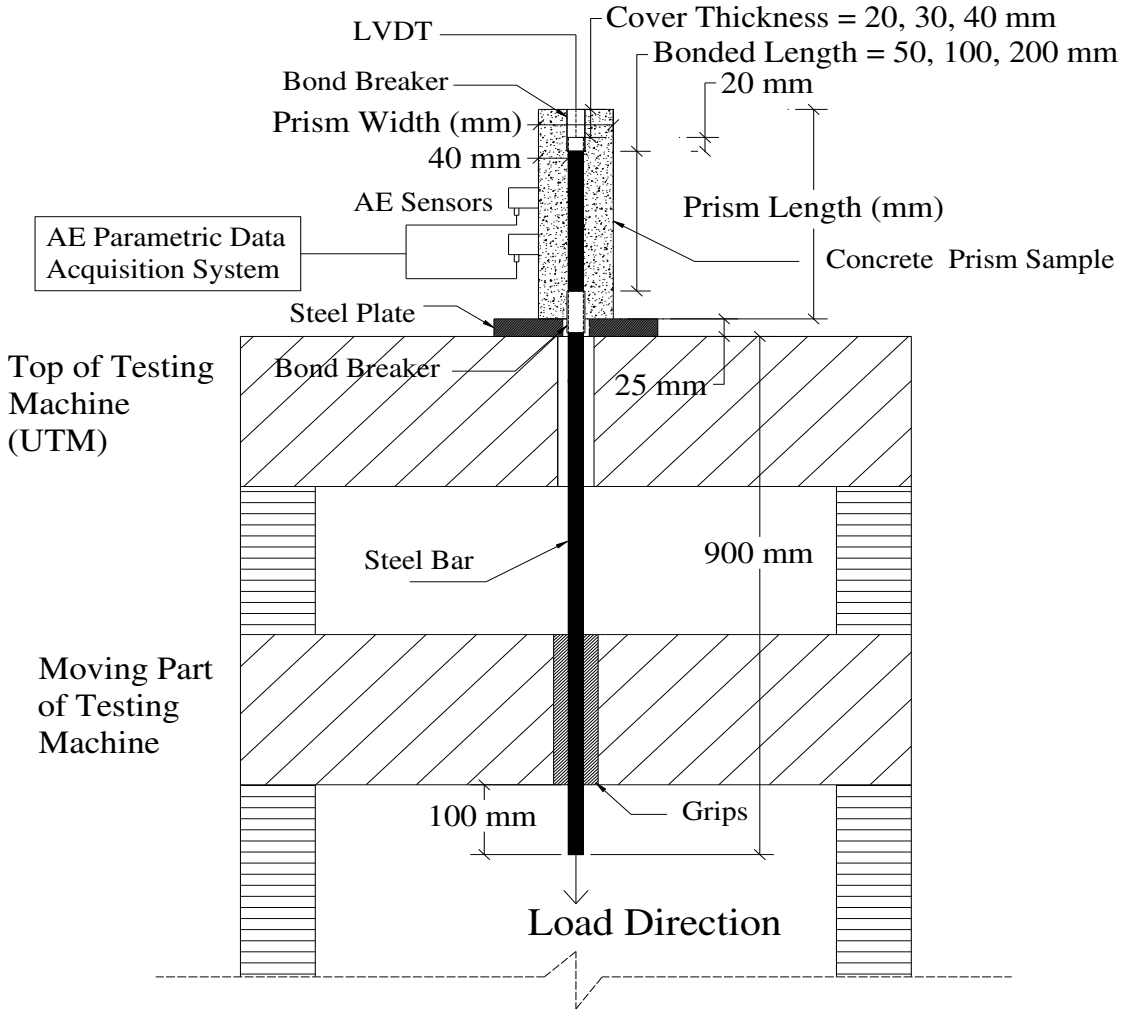

(b)

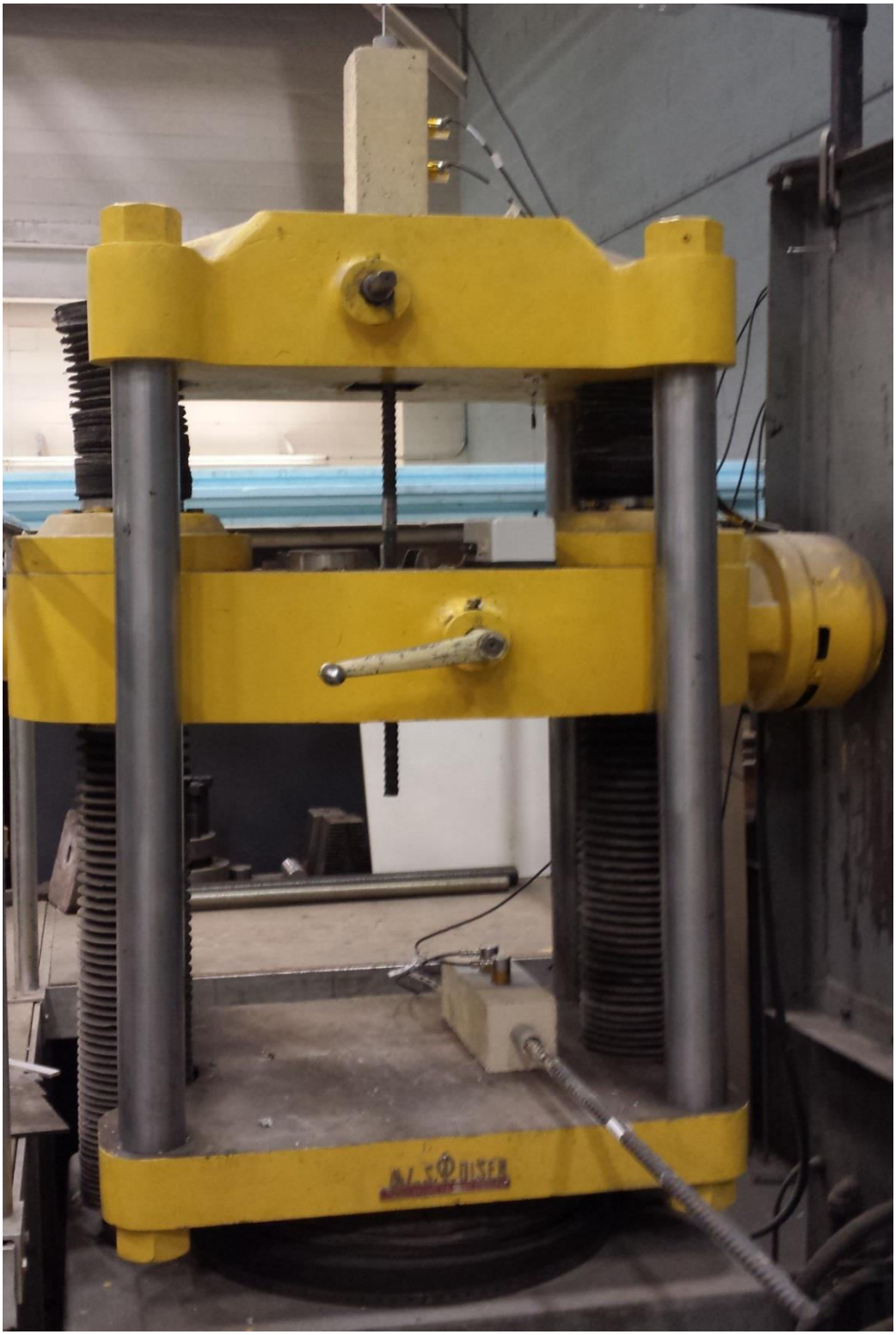

Figure 3.4 Pull-out test and AE monitoring setup: (a) schematic and (b) picture of typical experiment

3.6 Experimental Study 4: Evaluation of Concrete-Steel Bond Behaviour Using AE Sensors in Full-Scale Corroded/Un-Corroded RC Beams

The outcomes attained from study 3 were verified by performing further experiments on corroded/un-corroded full-scale RC beams.

3.6.1 Details of Tested Beams

The five corroded beams obtained from study 2 (AE monitoring during corrosion) were tested under four-point vertical loading conditions, as described in **Figure 3.5**. Those five beams are corroded to 5% (B1), 10% (B2), 20% (B3), and 30% (B4 and B5) of steel mass loss at only one of the anchorage sides of the beams end. Those anchorage beam specimens were selected for this investigation to represent realistic bond behaviour of full-scale reinforced concrete structures (ACI Committee 408, 2003). In addition, this study involved testing additional five un-corroded beams under the same test setup (**Figure 3.6**) to examine the use of longer anchorage lengths. In all beams, concrete was cast in wooden formwork while the 20M reinforcing bars were horizontally placed at the bottom of the formwork. All beams were compacted through mechanical vibration. After 24 hours of casting, the beam specimens were de-molded and then water-cured for a period of 28 days before being exposed to the accelerated corrosion or bond testing.

3.6.1.1 Corroded Beams

As previously mentioned, the five corroded beams tested in study 2 were further tested in this stage to evaluate their bond behaviour under four-point load tests. The anchorage lengths of all five corroded beams were chosen as 200 mm (less than the minimum

development length, as per CSA, 2014) and the shear span to depth ratio was kept constant to ensure bond failure in all beams. The AE monitoring was continued during these bond tests with the setup and configuration shown in **Figure 3.5**.

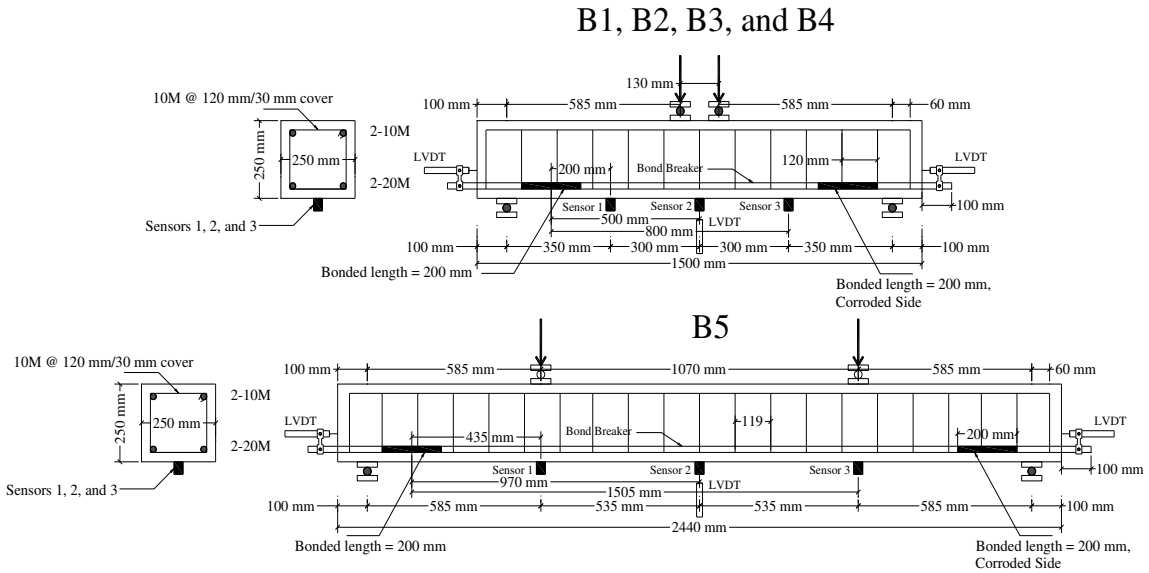

Figure 3.5 Four-point load test and AE monitoring setup of corroded beams

3.6.1.2 Un-Corroded Beams

For the comparison, this investigation involved testing additional five un-corroded beams. The anchorage length was varied in these un-corroded beams B6, B7, B8, B9, and B10 as follows: 100 mm, 200 mm, 300 mm, 400 mm, and 200 mm, respectively (**Figure 3.6**). This variable anchorage length is obtained by changing the length of the PVC pipes acting as the bond breaker. The dimensions of beams B6, B7, B8, and B9 are identical (250 x 250 x 1500 mm). On the other hand, B10 have the same cross section (250 x 250 mm), but with longer span (2440 mm) to study the influence of sensor location on the bond behaviour.

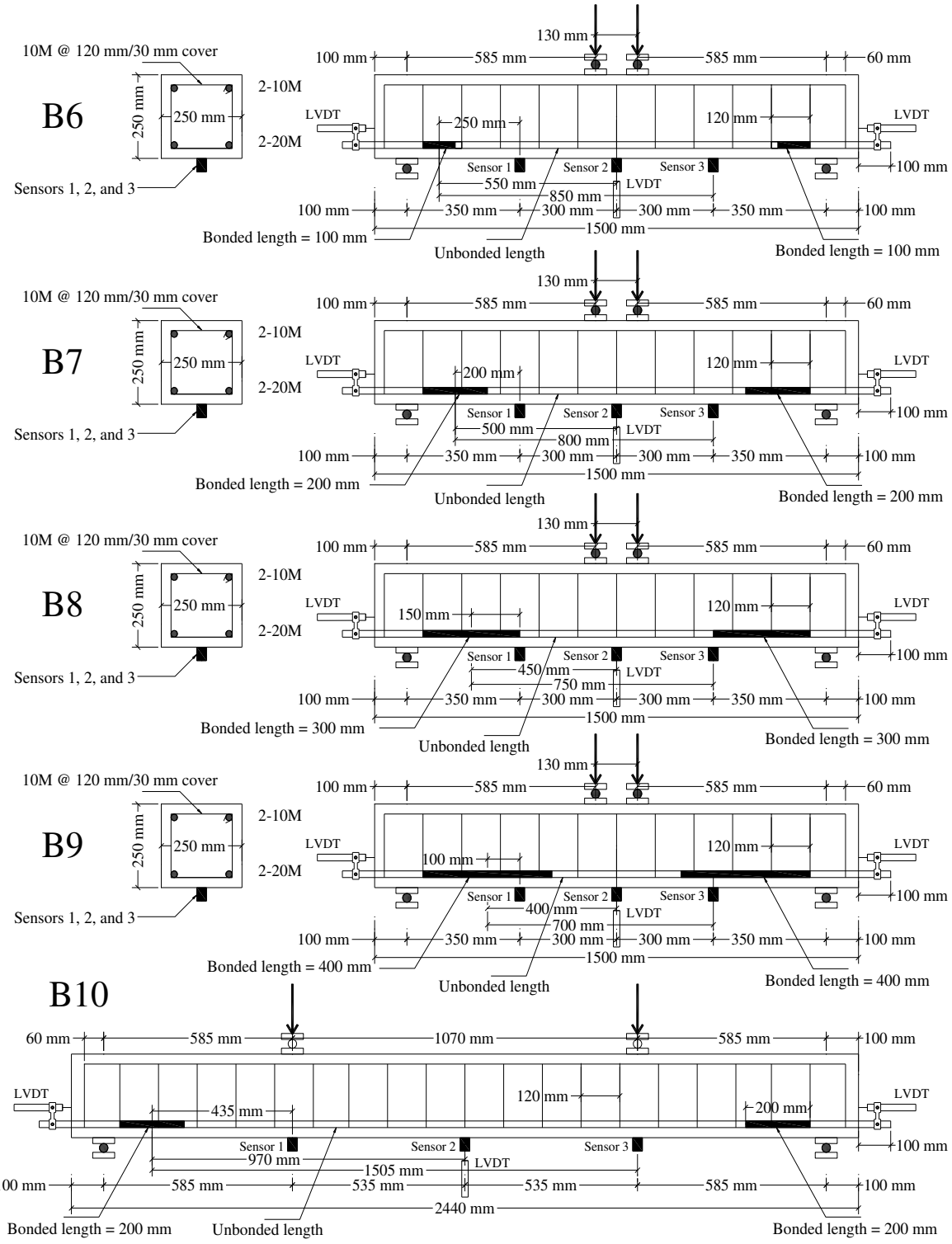

Figure 3.6 Four-point load test and AE monitoring setup of un-corroded beams

3.6.2 Four-Point Load Test Setup

All ten beams (five corroded and five un-corroded beams) were tested under four-point vertical loading conditions, as described in **Figure 3.7**. The vertical single load was applied through a manual hydraulic jack and then distributed into two-point loads by a steel plate/spreader beam. This loading was gradually applied at a constant loading rate for all tested beams up to failure. Four linear variable differential transformer (LVDT) were utilized to measure the free end slip of the protruding end of the steel bars at both beam's end (LVDT1 and LVDT2 on the left side and LVDT3 and LVDT4 on the right side). Another LVDT was mounted at the mid-span of each beam to record the values of mid-span deflection (**Figure 3.7**). All LVDTs used in this investigation were DC-DC long stroke displacement transducers (Model JEC-AG DC-DC from Honeywell) with a stroke range of ± 12.7 to 76.2 mm and output accuracy of about ± 0.0002 mm. The magnitude of load and the corresponding free end slip and mid-span deflection in each beam were all recorded using a data-acquisition system. The load was stopped twice during the tests to allow the visual observation of first crack and the identification of first bar slip using the readings of LVDTs. During the test and after failure, the crack widths were measured by using a crack width measuring device.

(a)

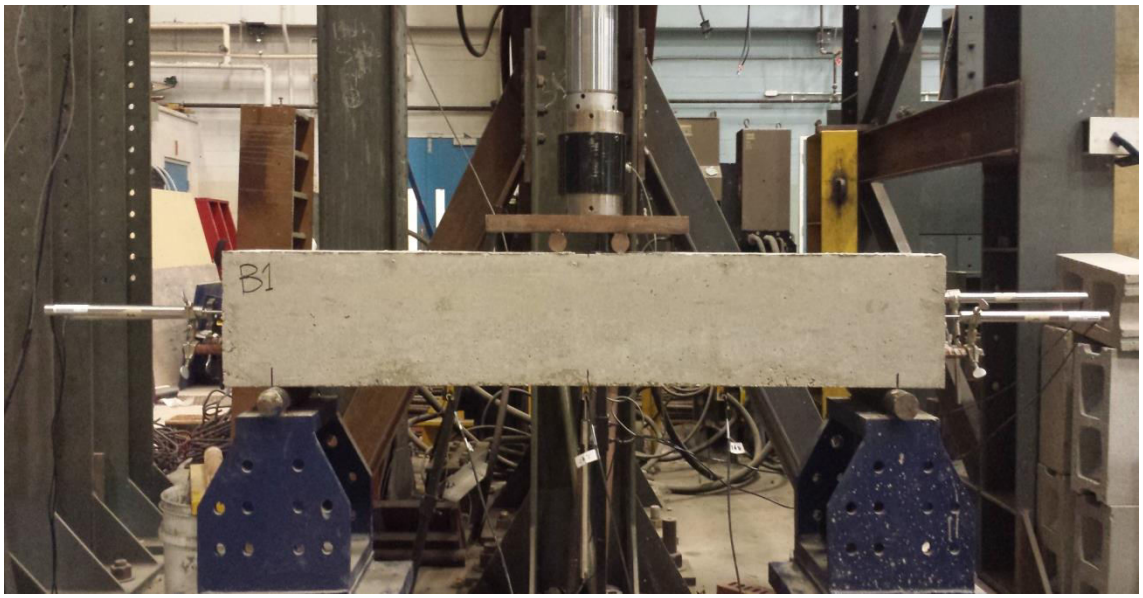

(b)

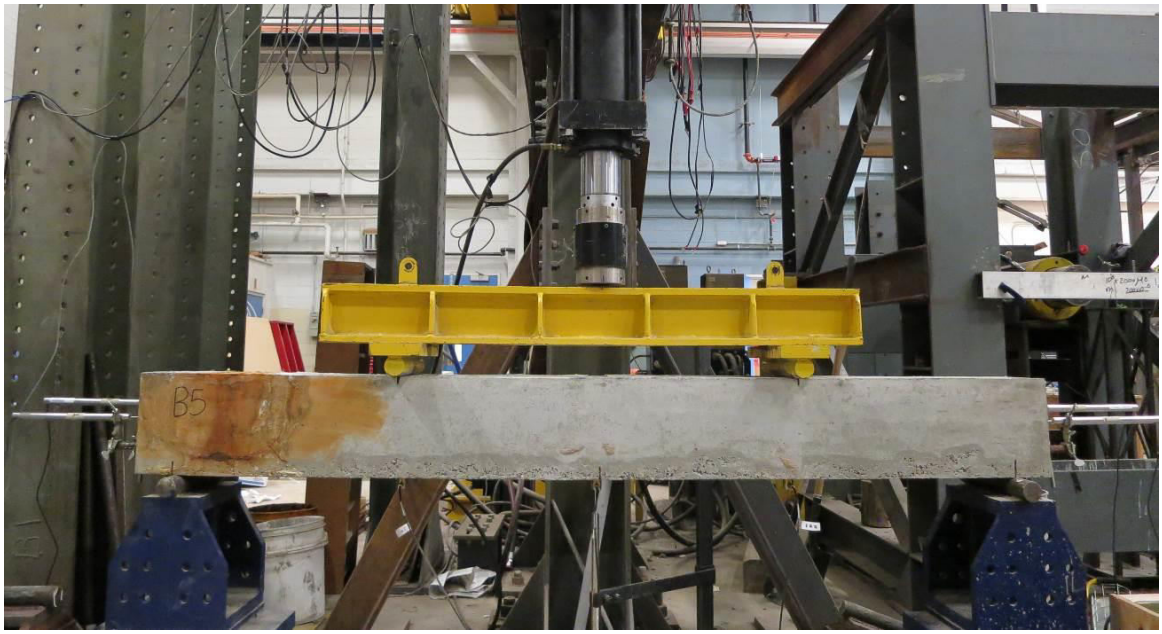

(c)

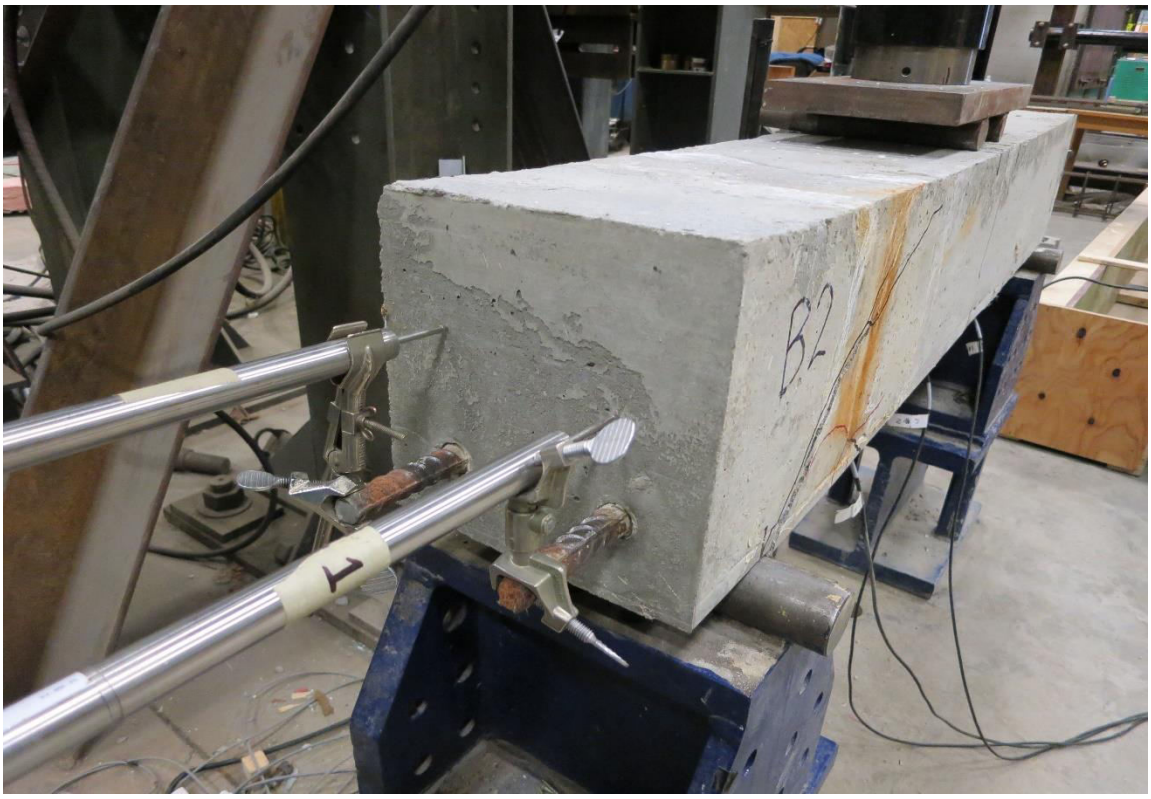

Figure 3.7 Four-point load test and AE monitoring typical setup: (a) short beam, (b) long beam, and (c) side view showing the LVDTs

3.6.3 AE Monitoring Setup

It is clear from **Figure 3.7** that, each beam was monitored throughout the four-point load test with three AE sensors. All sensors were attached at the bottom side of each beam at the centre of the beam width at the locations described in **Figures 3.5-3.6**. The acquisition of acoustic emissions during these tests was performed by means of the AE data acquisition system with the same setup described in the previous studies.

4. Discussion of Results from Experimental Study 1: Corrosion Detection and Crack Growth Monitoring in Small-Scale RC Samples

4.1 Introduction

This chapter presents the results and discussions of the first experimental study completed in this research. The results obtained at the end of the accelerated corrosion test on all tested samples are shown in **Table 4.1**. These results include the test duration, time to detect cover cracking by visual inspection, both theoretical and actual percentages of steel mass loss, and crack widths at the end of the experiments. **Table 4.1** shows that increasing the cover thickness from 20 to 40 mm resulted in longer test durations, longer time to first crack, and smaller crack widths at the same percentage of mass loss. The initiation of smaller crack widths with larger concrete cover may be attributed to the contribution of the confinement of the concrete cover, which increased by increasing the cover thickness. The table also shows that the actual degrees of steel mass loss were mostly in good agreement with the predicted percentage of steel mass loss results.

All tested samples showed a similar cracking behaviour, as seen in **Figure 4.1**. It can be noticed from the figure that the samples, regardless of cover thickness, exhibited one crack along the length of the embedded bar on only one side of the specimen. The results in **Table 4.1** will be used as a benchmark for the results obtained from AE monitoring in order to characterize the damage in the cover zone in terms of AE data.

Table 4.1 Results of all tested samples at the end of the accelerated corrosion tests

Specimen	Test duration (days)	Theoretical mass loss of steel (%)	Actual mass loss of steel (%)	Time to first detected crack (days)	Final crack width (mm)
20-1-1	3	1	0.8	3	0.12
20-1-2	3	1	0.8	3	0.1
20-2-1	5	2	1.7	3	0.65
20-2-2	5	2	1.9	3	0.76
20-3-1	6	3	2.9	3	0.9
20-3-2	6	3	2.8	3	0.85
20-4-1	8	4	3.8	3	2.5
20-4-2	8	4	4	3	2.2
20-5-1	10	5	5.1	3	5
20-5-2	10	5	5.4	3	4.88
30-1-1	7	1	0.8	5	0.1
30-1-2	7	1	0.9	5	0.1
30-2-1	9	2	1.7	5	0.48
30-2-2	9	2	1.9	5	0.53
30-3-1	11	3	2.9	5	0.78
30-3-2	11	3	2.8	5	0.82
30-4-1	13	4	4	5	1.38
30-4-2	13	4	3.9	5	1.24
30-5-1	15	5	4.9	5	2.5
30-5-2	15	5	4.8	5	2.3
40-1-1	12	1	0.9	10	0.1
40-1-2	12	1	0.8	10	0.08
40-2-1	15	2	1.8	10	0.46
40-2-2	15	2	1.8	10	0.48
40-3-1	17	3	3	10	0.72
40-3-2	17	3	2.8	10	0.8
40-4-1	19	4	3.9	10	1.12
40-4-2	19	4	4	10	1.23
40-5-1	21	5	4.8	10	1.88
40-5-2	21	5	4.9	10	1.95

(a)

(b)

(c)

Figure 4.1 Typical cracking behaviour of tested samples: (a) 20-3-1, (b) 30-3-1, and (c) 40-3-1

4.2 AE Waveform Parameters

The results collected from AE sensors were subjected to a filtering process in order to minimize noise related signals or wave reflections. Amplitude-duration based filter (or Swansong II filter) similar to that adopted in similar research studies (Fowler et al., 1989; Abdelrahman et al., 2014; ElBatanouny et al., 2014; Vélez et al., 2015) was performed herein. After reviewing the collected waveform parameters, all signals characterized by low amplitude range (40-45 dB) were considered to be related to noise and therefore were all rejected. In addition, signals with higher amplitudes and relatively long durations were excluded based on the amplitude-duration ranges in **Table 4.2**. **Figure 4.2** shows some examples of different rejected waveforms at all amplitude ranges based on the rejection

limits described in **Table 4.2**. It should be mentioned that the AE waveform signatures may vary from those occurring in natural corrosion mechanisms. Consequently, the limits of the filter presented herein may be modified in naturally occurring corrosion process to differentiate corrosion related AE signals. This target can be achieved by performing an extensive evaluation of different collected waveforms to generate suitable filter limits (Vélez et al., 2015).

Table 4.2 Rejection limits for amplitude-duration filter (Vélez et al., 2015)

Amplitude range (dB)	Duration (μs)	
	Lower	Upper
40<A<45*	—	—
45 ≤ A<54	0	1000
54 ≤ A<60	100	1000
60 ≤ A<65	300	1000
A ≥ 65	500	1000

*All signals were rejected regardless of the duration value

(a)

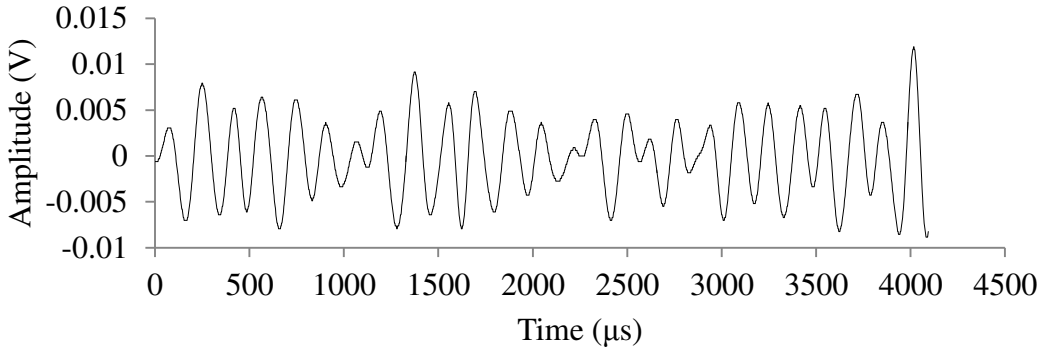

(b)

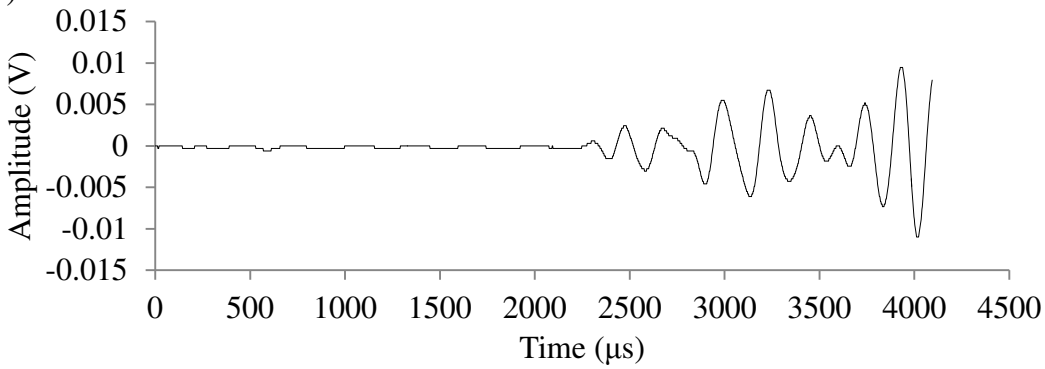
0.015
0.01
0.005
0
-0.005
-0.01
-0.015
Amplitude (V)
0
500
1000
1500
2000
2500
3000
3500
4000
4500
Time (μs)

(c)

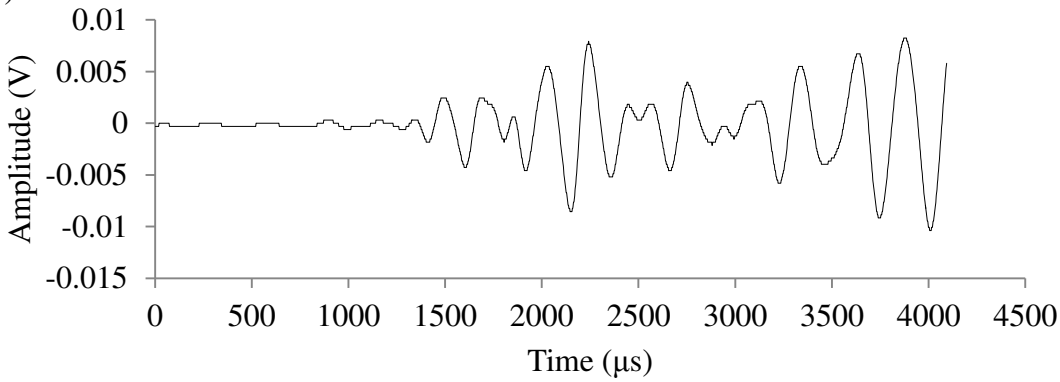
0.01
0.005
0
-0.005
-0.01
-0.015
Amplitude (V)
0
500
1000
1500
2000
2500
3000
3500
4000
4500
Time (μs)

(d)

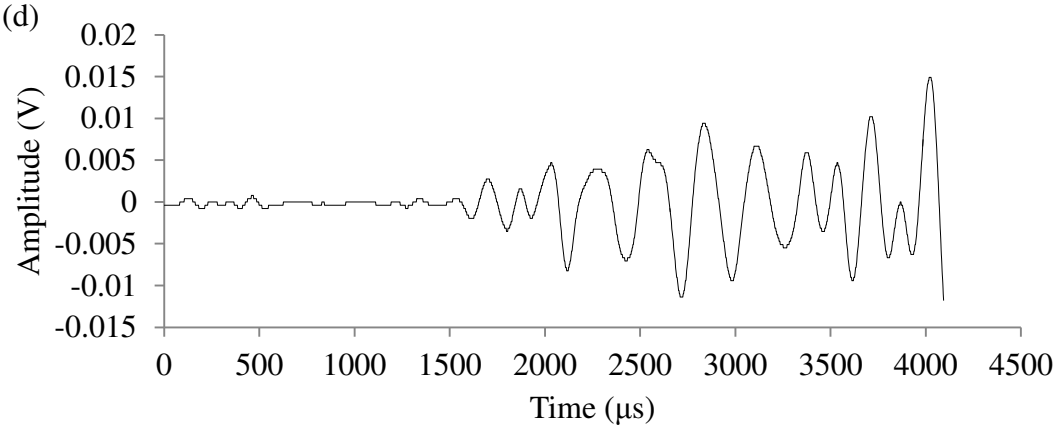
0.02
0.015
0.01
0.005
0
-0.005
-0.01
-0.015
Amplitude (V)
0
500
1000
1500
2000
2500
3000
3500
4000
4500
Time (μs)

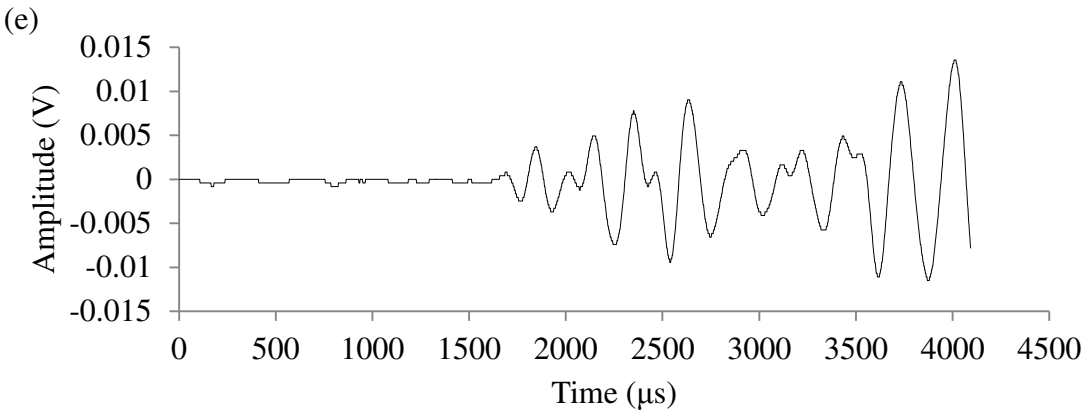

Figure 4.2 Examples of rejected waveforms with amplitude values of: (a) 43 dB, (b) 47 dB, (c) 57 dB, (d) 63 dB, and (e) 66 dB

After performing the above filtering criteria, the results of different waveform parameters of all samples were analyzed and evaluated. These parameters included signal strength, energy, absolute energy, amplitude, rise time, duration, counts, as well as frequency parameters. By studying the relationships of each of the aforementioned parameters with the elapsed time, it was found that all the parameters have a similar trend of variation. However, the AE signal strength was chosen in this study to evaluate the process of damage in all tested samples. It should be mentioned that, different researchers also applied signal strength analysis for a better assessment of concrete structures under corrosion (Di Benedetti et al., 2013; Mangual et al., 2013a; 2013b; ElBatanouny et al., 2014; Vélez et al., 2015). In this study, cumulative signal strength (CSS) was calculated and analyzed for detecting both the onset and progression of the corrosion in all tested samples. This CSS is calculated as the integral of signal strength (voltage) over time of recorded AE hits until any period of time during the test. The variations in CSS with respect to time were monitored in order to differentiate between degrees of damage.

4.3 AE Intensity Analysis

The results of signal strength were further analyzed to obtain more accurate indications of the levels of damage from corrosion and were also used to quantify this level in terms of steel mass loss and cover cracking. To this end, an intensity analysis was performed using the signal strength values of all acquired signals (hits) to calculate two parameters, historic index and severity. Historic index, or *H (t),* is a parameter that indicates any sudden changes of slope of CSS curve by comparing the average signal strength of the last *K* hits with the mean value of the signal strength of all acquired hits. This index can be calculated using **Equation 4.1** and is used to represent the level of damage in concrete structures (Mangual et al., 2013a; 2013b; ElBatanouny et al., 2014; Vélez et al., 2015).

$$H(t) = \frac{N}{N-K}\frac{\sum_{i=K+1}^{N} S_{oi}}{\sum_{i=1}^{N} S_{oi}} \qquad \textbf{(4.1)}$$

Where: N = the number of hits up to time *(t);* and S_{oi} = signal strength of the i^{th} event (Golaski et al., 2002; Nair and Cai, 2010; ElBatanouny et al., 2014; Vélez et al., 2015).

On the other hand, severity (S_r) may be described as the average signal strength of the *J* events with the maximum algebraic value of signal strength at any time and can be assessed by **Equation 4.2** (Golaski et al., 2002; Nair and Cai, 2010; ElBatanouny et al., 2014; Vélez et al., 2015).

$$S_r = \sum_{i=1}^{J} \frac{S_{oi}}{J} \qquad \textbf{(4.2)}$$

It is worth noting that, the values of the constants *K* in **Equation 4.1** and *J* in **Equation 4.2** may vary based on the type of phenomenon, degradation mechanisms, and simulation method (For example; natural versus accelerated corrosion). Parametric analysis can be performed to better understand the influence of these constants on severity and historic

index based on the mechanism of damage (Vélez et al., 2015). The value of K can be calculated as a function of the number of hits based on the equations specified in some research studies (Golaski et al., 2002; Nair and Cai, 2010; ElBatanouny et al., 2014; Vélez et al., 2015). On the other hand, the value of J is taken as 50 in these reported papers (Golaski et al., 2002; Nair and Cai, 2010; ElBatanouny et al., 2014; Vélez et al., 2015). Initially, the intensity analysis was performed on the values of signal strength by using the previously mentioned constants (Golaski et al., 2002; Nair and Cai, 2010; ElBatanouny et al., 2014; Vélez et al., 2015). Alternatively, the values of K and J were assumed as 25 and 35, respectively, based on the results of a parametric analysis performed in the literature to identify the optimum values of theses constants for corrosion detection in concrete structures (Vélez et al., 2015). By assuming these constants as $K = 25$ and $J = 35$, it was found that these values were more suitable to capture the variations in both values of $H(t)$, and S_r corresponding to different levels of damage. The values of both historic index and severity were calculated for all samples using **Equation 4.1 and 4.2** continuously throughout the tests. These values were then drawn versus time to detect the onset of early damage and are shown in **Figure 4.3** (first 24 hours of sample 20-5-1 as an example).

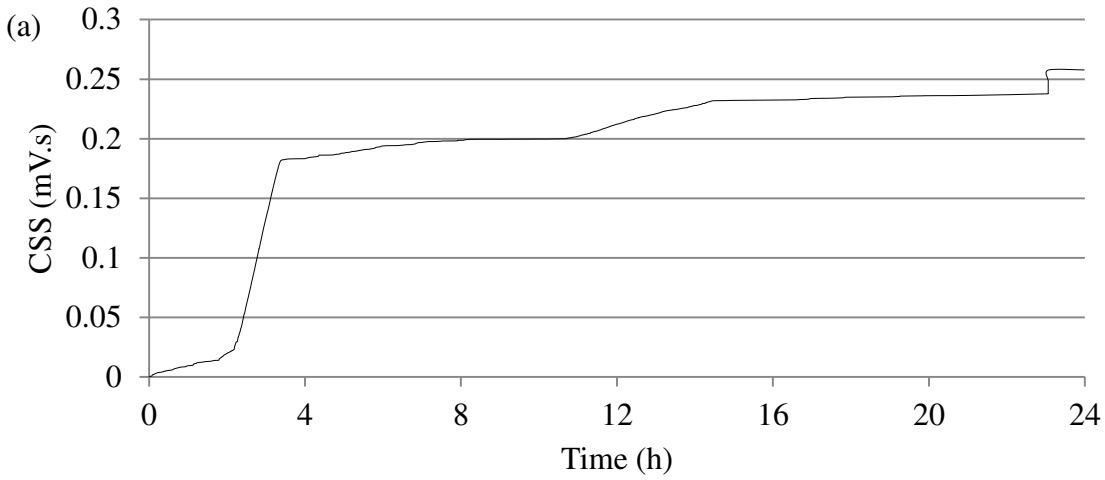
(a)
0.3
0.25
0.2
0.15
0.1
0.05
0
CSS (mV.s)
0
4
8
12
16
20
24
Time (h)

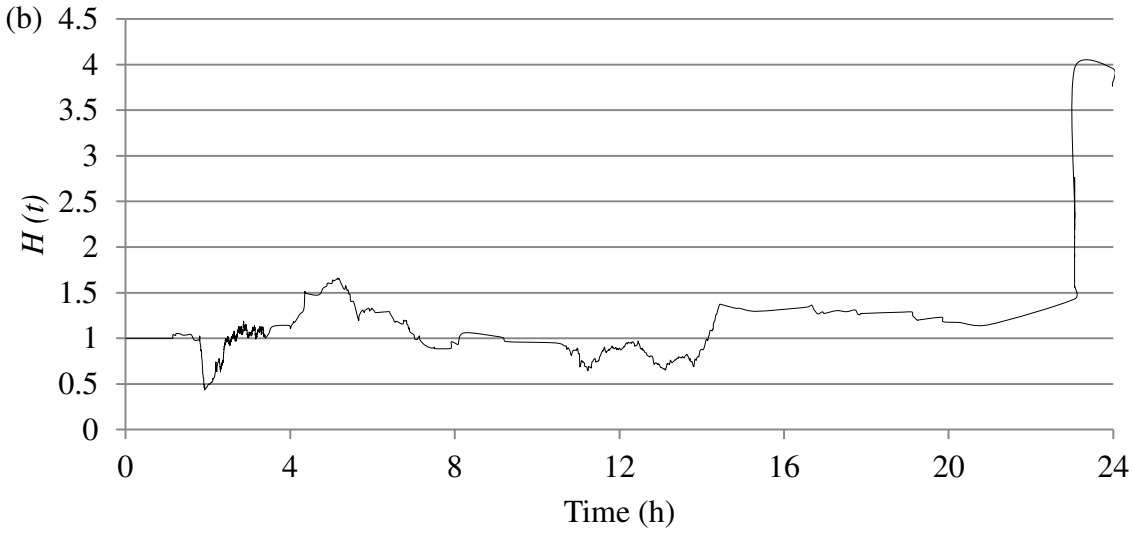
(b)
4.5
4
3.5
3
2.5
2
1.5
1
0.5
0
H (t)
0
4
8
12
16
20
24
Time (h)

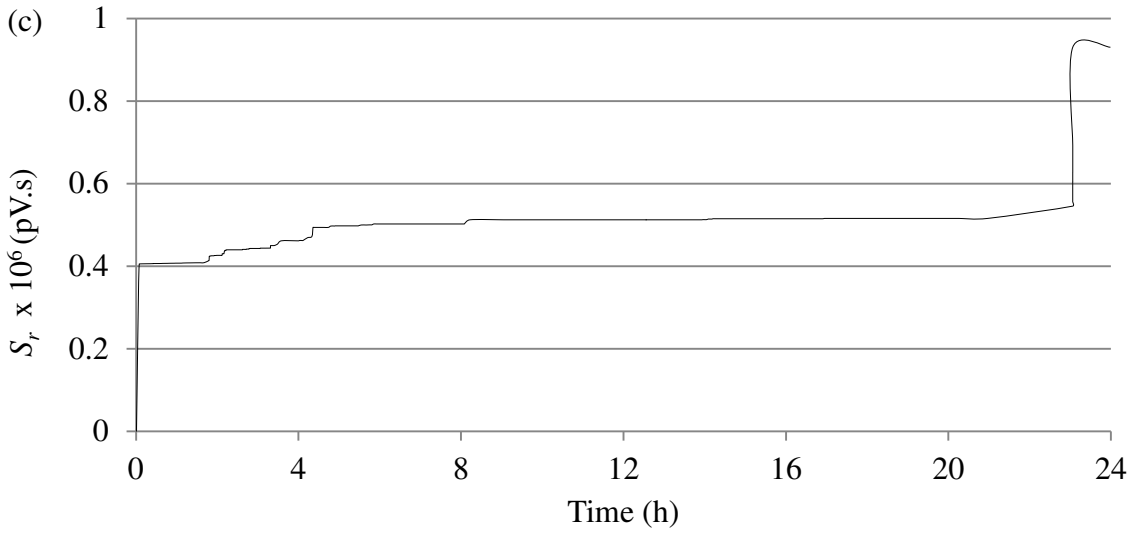

Figure 4.3 Values of CSS, *H (t)*, and S_r for the first 24 hours of sample 20-5-1: (a) CSS versus time, (b) *H (t)* versus time, and (c) S_r versus time

4.4 Corrosion Detection Using AE Analysis

The curves showing variation in CSS for the 20 mm cover samples (as an example of all tested samples) can be seen in **Figure 4.4**. This figure shows that an overall increase in the CSS was recorded as a result of both corrosion initiation and micro-cracking resulting from the expansions due to the accumulation of corrosion products, in all tested samples. The change in CSS over time is monitored in order to identify corrosion onset. It has been reported that the points of sudden rise of the CSS curve can be used to detect any sudden damage in concrete (corrosion initiation in this case) (Ohtsu and Tomoda 2008; Di Benedetti et al., 2013). By applying such an approach, it can be identified in **Figure 4.4** that all CSS curves exhibited a sharp increase at approximately 22 hours (average time of all tested sample). At these points, sudden increases in the CSS can be located in the curve, which are associated with an average CSS value of 0.1 mV.s (**Table 4.3**). This first detected sudden rise is mostly related to the point of corrosion initiation when an increase

in AE events (in terms of CSS increase) are detected resulting from steel depassivation (accumulation of oxides at the steel-concrete interface). This point has been confirmed from the findings of similar research studies reported in the literature (Ohtsu and Tomoda 2008; Di Benedetti et al., 2013; Mangual et al., 2013a; 2013b; ElBatanouny et al., 2014; Vélez et al., 2015). It should be mentioned that some samples exhibited a sudden rise in the CSS well before the 22-hour average of all tested samples (**Figure 4.4**). These points however, may not be correlated to corrosion initiation. This is because the corresponding values of the electrical current for these points were decreasing and the HCP readings for them were indicating no corrosion activity, as explained in Section 4.5 (**Figure 4.5**). Instead, those early detected AE activities may be attributed to the movement of chloride solution while penetrating the concrete cover (Di Benedetti et al., 2014). It is also clear from **Figure 4.4** that the values of CSS showed significant variations at the same time of the test (even between replicates of identical samples). These results indicate that the CSS curves can only be utilized for damage identification rather than quantifying the extent of degradation. Furthermore, the use of impressed currents to accelerate corrosion may also influence the values of CSS when compared to those related to natural corrosion process.

The results of CCS, historic index, and severity are shown in **Figure 4.3** (showing the first 24 hours of sample 20-5-1 as an example). The intensity analysis curves (**Figure 4.3b, c**) can be utilized to further confirm the detection of corrosion initiation. It is clear from these curves that a sudden AE activity occurred in both $H(t)$ and S_r for sample 20-5-1 (at the location of the first sudden increase in CSS curve). Historic index value of 1.61 and severity of 0.56 x 10^6 pV.s were clearly observed at that sudden AE activity (**Figure**

4.3b, c). The results of $H(t)$ and S_r of the other 20 mm cover samples show a similar trend with average values of 1.41 and 0.52 x 10^6 pV.s, respectively (**Table 4.3**).

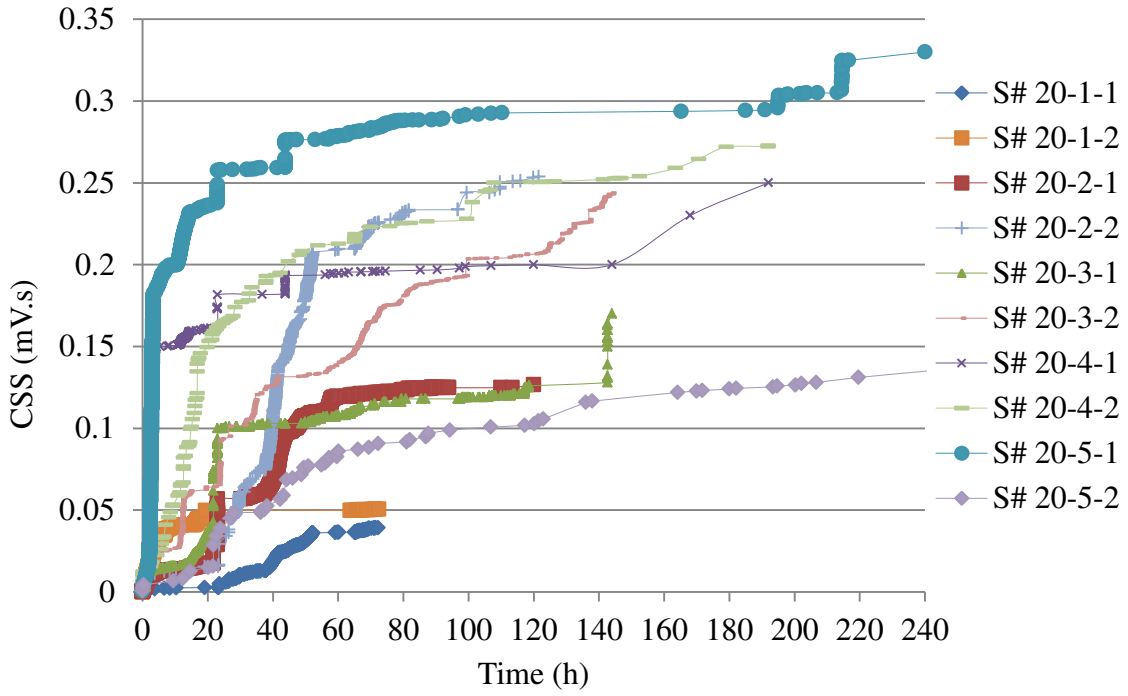

Figure 4.4 CSS versus test time for the 20 mm cover samples

It can be noticed from **Figure 4.4** that a second point of sudden increase of the CSS represents another significant intensity of AE events at an average time of 43.3 hours of all tested specimens. This AE activity may be associated with the onset of micro-cracking, which could also be associated with the loss of steel-concrete bonding. The assumption that this point could be related to the occurrence of micro-cracking can somewhat be justified by the detection of cover cracking which was visually observed at 72 hours in all tested samples. However, this assumption is not substantiated and cannot be correlated to AE signal strength parameters. Instead, **Table 4.3** presents the values of

cover crack widths detected using visual inspection of all samples as well as the values of CSS, *H (t),* and S_r. It is obvious that an overall increase in the values of CSS, *H (t),* and S_r corresponding to the progression of corrosion (from corrosion initiation to visual cover cracking) in all specimens. However, the presented values of CSS, *H (t),* and S_r may depend on the range of tested variables and type of sensors used in this study. In addition, further validation of the presented results is needed to overcome the potential disadvantages in assessing corrosion by means of impressed currents (Poursaee and Hansson, 2009), prior to use it as a reliable monitoring tool in field applications.

Table 4.3 Different AE parameters at different levels of damage for 20 mm cover samples

Specimen	First detected AE activity (Corrosion initiation)				First detected cover crack using visual inspection detected at 72 h							Values of different parameters after 24 hours from first crack detection		
	Time (h)	CSS (mV.s)	*H (t)*	S_r x 10^6 (pV.s)	Crack Width (mm)	CSS (mV.s)	% Increase in CSS*	*H (t)*	% Increase in *H (t)**	S_r x 10^6 (pV.s)	% Increase in S_r *	CSS (mV.s)	*H (t)*	S_r x 10^6 (pV.s)
20-1-1	23.61	0.02	1.18	0.43	0.10	0.04	100	5.02	325	1.59	270	NA	NA	NA
20-1-2	20.53	0.04	1.29	0.69	0.12	0.05	25	6.04	368	1.89	174	NA	NA	NA
20-2-1	21.77	0.05	1.54	0.57	0.20	0.12	300	5.18	236	1.67	193	0.12	5.57	1.79
20-2-2	23.61	0.20	1.75	0.72	0.15	0.23	15	5.37	207	1.75	143	0.23	5.72	1.76
20-3-1	23.06	0.04	1.10	0.38	0.24	0.12	200	5.48	398	1.79	371	0.12	5.98	2.11
20-3-2	22.89	0.10	1.43	0.55	0.20	0.17	70	6.11	327	1.80	227	0.19	6.11	2.23
20-4-1	20.97	0.16	1.35	0.35	0.25	0.19	19	6.23	361	1.61	360	0.19	6.65	1.69
20-4-2	22.58	0.19	1.59	0.51	0.22	0.22	16	6.05	281	1.77	247	0.23	6.21	1.8
20-5-1	22.79	0.25	1.61	0.56	0.15	0.28	12	5.70	254	1.54	175	0.29	6.19	1.63
20-5-2	20.49	0.03	1.25	0.39	0.18	0.09	200	5.42	334	1.69	333	0.10	5.82	1.85
Average	22.04	0.11	1.41	0.52	0.18	0.15	45	5.66	301	1.71	229	0.18	6.03	1.86

*Percentage of increase from the first detected AE activity (corrosion initiation)

4.5 Evaluation of Corrosion Detection Using Electrochemical Measurements

The results obtained from both the HCP test and anodic passing currents throughout the test period for five selected samples (20 mm cover) are described in **Table 4.4** and **Figure 4.5**. The graphs in **Figure 4.5** are used to detect the corrosion initiation times in order to

compare them with those obtained from the AE monitoring. It can be noticed from these curves that the values of the passing electrical current decreased at the first part of the curve reaching the lowest point of the curve, then started to increase until the end of the test. The lowest point in the current-time curve occurred at times ranging between 20 and 40 hours. This point can be related to initiation of the corrosion activity (depassivation of steel) in the tested sample (Mangual et al., 2013a; 2013b; ElBatanouny et al., 2014). On the other hand, the HCP test indicates a 90% possibility of corrosion if the results are more negative than -350 mV (ASTM C876, 1991). Following this approach, the values of the HCP test for the tested samples exceeded -350 mV at a time ranging from 60 to 80 hours (**Figure 4.5**). By checking the corrosion initiation times for all samples, it can be concluded that the corrosion initiation times detected by the electric currents (by locating the lowest point in the current-time curve (Mangual et al., 2013a; 2013b; ElBatanouny et al., 2014)) are similar to those obtained from AE analysis. Nonetheless, the results of HCP indicated the probability of corrosion onset at noticeably larger times than those identified by both current-time curve and AE results. This finding is also confirmed in similar research reported in the literature (Ohtsu and Tomoda 2008; Di Benedetti et al., 2013; Mangual et al., 2013a; 2013b; ElBatanouny et al., 2014; Vélez et al., 2015). This can be attributed to the higher sensitivity of the AE technique, which can detect the stage of micro-damage. Moreover, the values of HCP were only measured on a daily basis throughout the test compared to the continuous monitoring of electrical current and acoustic emissions. Furthermore, the values of HCP can only be used for corrosion detection and are not applicable to quantify the degree of corrosion. This is especially true

as the HCP test results can only indicate the probability of corrosion and cannot be correlated to the actual degree of corrosion damage.

Table 4.4 Typical results of currents and HCP readings

Specimen	Average anodic current (mA)	HCP (mV)
20-1-1	66	-355
20-2-1	78	-385
20-3-1	94	-423
20-4-1	96	-448
20-5-1	100	-590

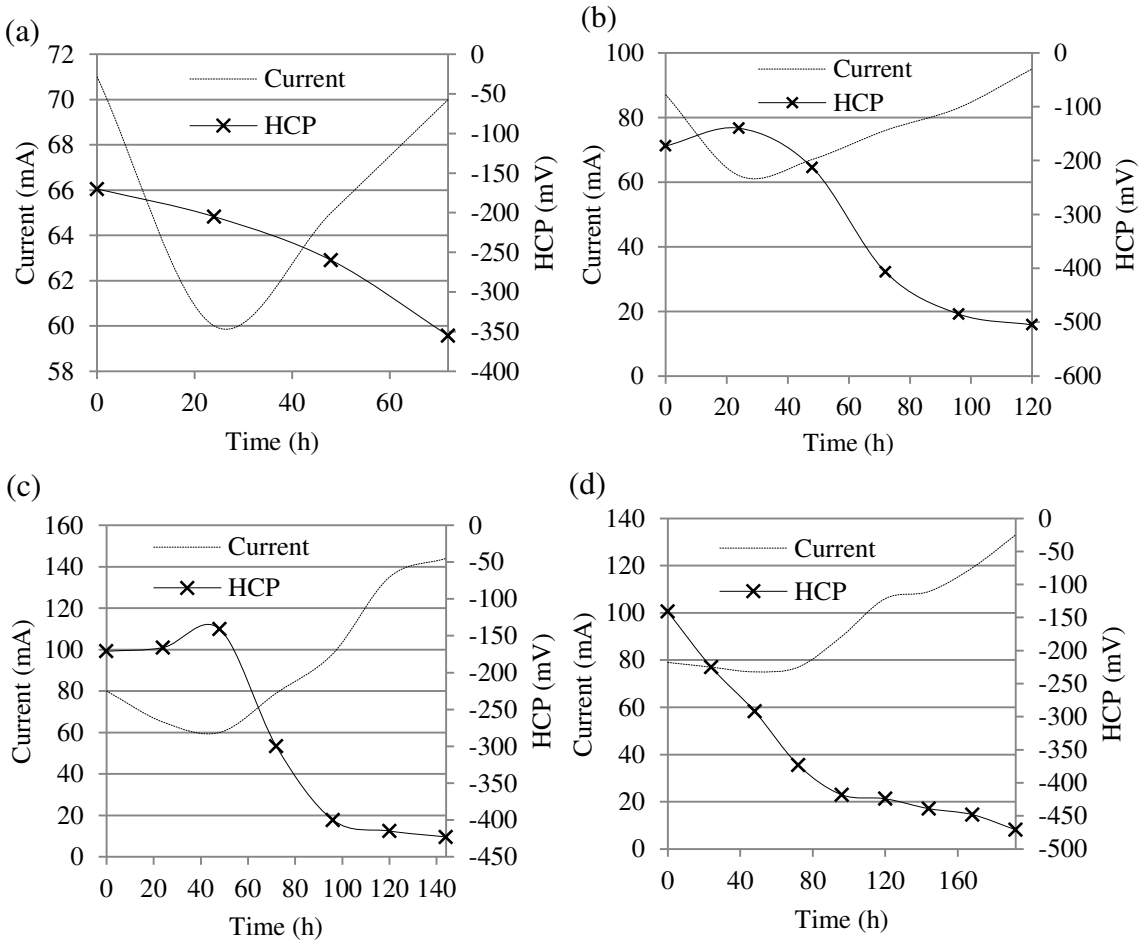

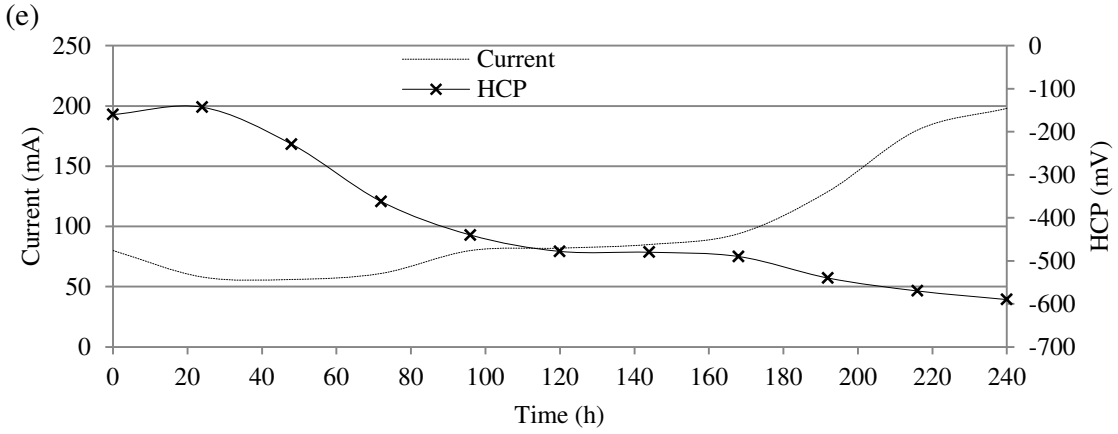

Figure 4.5 Current versus HCP results for selected specimens: (a) 20-1-1, (b) 20-2-1, (c) 20-3-1, (d) 20-4-1, and (e) 20-5-1

4.6 Evaluation of Damage Progression Using AE Analysis

Following the stage of corrosion initiation and micro-cracking, the samples were severely corroded to reach specific levels of mass loss. Meanwhile, AE monitoring was continued during this stage to assess its ability to represent the actual degree of damage occurring in each sample. For this reason, the CSS values were calculated similarly along with the theoretical degree of mass loss each 24 hours for all 20 mm cover samples and presented in **Figure 4.6**. After a period of approximately 72 hours, the first visual crack was detected (by visual inspection) for all 20 mm cover samples. The samples generally showed only one longitudinal crack parallel to the steel bar (approximately at the centre of the embedded steel bar) at only one side of each sample (see **Figure 4.1**). The occurrence of visual cover cracks may be explained by the expansion of the embedded steel bars due to the accumulation of rust products. Upon the conclusion of the test, all specimens were broken and the actual percentages of mass loss of steel bars were

measured as seen in **Figure 4.7**. **Table 4.1** also compares the theoretical to actual mass loss of steel which showed a well agreement between both values in all tested samples.

It can be noticed from **Figure 4.6** that all samples showed an overall increase in the CSS values as a result of increasing amounts of theoretical mass loss up to 5.3%. For instance, in sample 20-5-1, the recorded CSS was constantly increased from 0.26 to 0.33 mV.s, due to the increase of corrosion mass loss starting from 0.37 up to 5.3% mass loss. The other samples also confirmed a correlation between both mass loss with CSS throughout the tests. Thus, it can be concluded that the AE results (CSS) can be correlated to both the degree of mass loss caused by corrosion of steel in concrete. However, beyond the observation of first visual crack, both corrosion propagation (in terms of steel mass loss) and cover cracking may occur simultaneously. This can be explained by the increasing trend in the results of CSS due to the increase in the values of both steel mass loss and cover crack width. It should be noted that the rate of increase in CSS values was slower after the formation of visual cracks owing to the continuous opening of the crack width, which contributes to the wave attenuation that yields lower values of signal strength. This wave attenuation could be attributed to the reduction of signal amplitude of AE waves as a result of scattering and reflections (Ervin, 2007). It should also be noted that the absolute values of CSS exhibited variations between tested samples at similar degrees of damage (see **Figure 4.6**). Consequently, the analysis of CSS can only indicate the progression of damage and may not solely be used to quantify the degree of mass loss or cover cracking. Alternatively, further intensity analysis on the values of signal strength was performed for damage quantification of tested samples, as described in the following section.

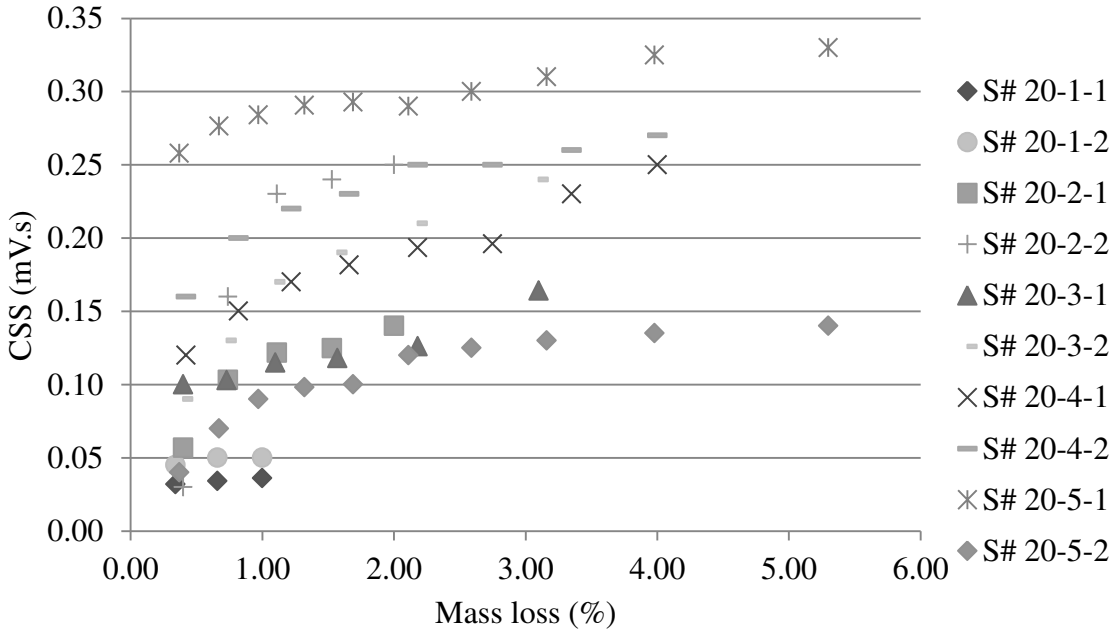

Figure 4.6 CSS versus mass loss for 20 mm cover samples at 24-hour intervals

Figure 4.7 Effects of different levels of mass loss in 20 mm cover samples

4.7 Correlations between the Degree of Corrosion and AE Intensity Analysis Parameters

As previously stated, the AE intensity analysis was recommended to quantify the extent of damage in the tested samples. Two parameters, historic index and severity, were estimated at different degrees of mass loss for the 20 mm cover samples and reported in **Table 4.5**. In addition, intensity classification chart (**Figure 4.8**) was developed to predict

the level of corrosion damage in reinforced concrete subjected to reinforcing steel corrosion based on the acquired AE data. **Table 4.5** contains the results of $H(t)$ and S_r for the 20 mm cover samples at five degrees of corrosion damage in terms of steel mass loss (1%, 2%, 3%, 4%, and 5%). These results were also used to develop the intensity analysis chart that can directly correlate the extent of damage (in term of mass loss) to the AE recorded signals (**Figure 4.8**). This chart can give a range within which the damage can be classified. For example, by knowing that the historic index is between 5.18 and 6.23 or the severity is between 1.54 and 1.89 x 10^6 (pV.s), it can be concluded that the corrosion of the embedded steel has a 1% mass loss. Likewise, all other levels of damage can be identified by locating the values of $H(t)$ and/or S_r into the intensity analysis chart and then comparing it to the corresponding ranges of each level. It is clear from the same chart that the values obtained from different tested samples at the same stage of corrosion exhibited insignificant variations. This shows that the intensity analysis can give a more accurate representation of damage than that obtained from the CSS. It is also obvious from the chart that the corrosion progression yielded an overall linear increase in both $H(t)$ and S_r values at all degrees of damage from corrosion initiation until 5% steel mass loss. Based on the above results, AE monitoring can characterize the percentage of mass loss and eventually estimate the residual strength of concrete structures exposed to reinforcing steel corrosion. It is worth taking into consideration that this chart is based on the experimental results presented in the current study and more tests are required to validate and generalize these conclusions. These tests may induce corrosion without using impressed currents (for example, wet and dry tests) to capture any differences in the presented values of $H(t)$ and S_r, if any.

Table 4.5 Results of intensity analysis at consequent degrees of damage for 20 mm cover samples

Sample	Mass loss																	
	1%		2%				3%				4%				5%			
	$H(t)$	S_r ($\times 10^6$) pV.s	$H(t)$	% $H(t)$ *	S_r ($\times 10^6$) pV.s	% S_r *	$H(t)$	% $H(t)$ *	S_r ($\times 10^6$) pV.s	% S_r *	$H(t)$	% $H(t)$ *	S_r ($\times 10^6$) pV.s	% S_r *	$H(t)$	% $H(t)$ *	S_r ($\times 10^6$) pV.s	% S_r *
20-1-1	5.02	1.59	NA	NA	NA	NA	NA	NA	NA	NA	NA	NA	NA	NA	NA	NA	NA	NA
20-1-2	6.04	1.89	NA	NA	NA	NA	NA	NA	NA	NA	NA	NA	NA	NA	NA	NA	NA	NA
20-2-1	5.18	1.67	6.15	19	1.75	5	NA	NA	NA	NA	NA	NA	NA	NA	NA	NA	NA	NA
20-2-2	5.37	1.75	6.31	18	1.88	7	NA	NA	NA	NA	NA	NA	NA	NA	NA	NA	NA	NA
20-3-1	5.48	1.79	6.41	17	2.17	21	7.40	35	2.37	32	NA	NA	NA	NA	NA	NA	NA	NA
20-3-2	6.11	1.80	6.55	7	2.23	24	7.15	17	2.44	36	NA	NA	NA	NA	NA	NA	NA	NA
20-4-1	6.23	1.61	6.86	10	1.86	16	7.12	14	2.21	37	8.15	31	2.28	42	NA	NA	NA	NA
20-4-2	6.05	1.77	6.25	3	1.81	2	6.89	14	2.08	18	7.91	31	2.19	24	NA	NA	NA	NA
20-5-1	5.70	1.54	6.6	16	1.97	28	7.28	28	2.17	41	8.70	53	2.36	53	9.40	65	2.57	67
20-5-2	5.42	1.69	6.48	20	1.90	12	7.17	32	2.10	24	8.88	64	2.27	34	9.28	71	2.66	57
Average	5.66	1.71	6.45	14	1.95	14	7.16	27	2.22	30	8.41	49	2.28	33	9.34	65	2.62	53

*Percentage of increase from the values calculated at 1% of steel mass loss

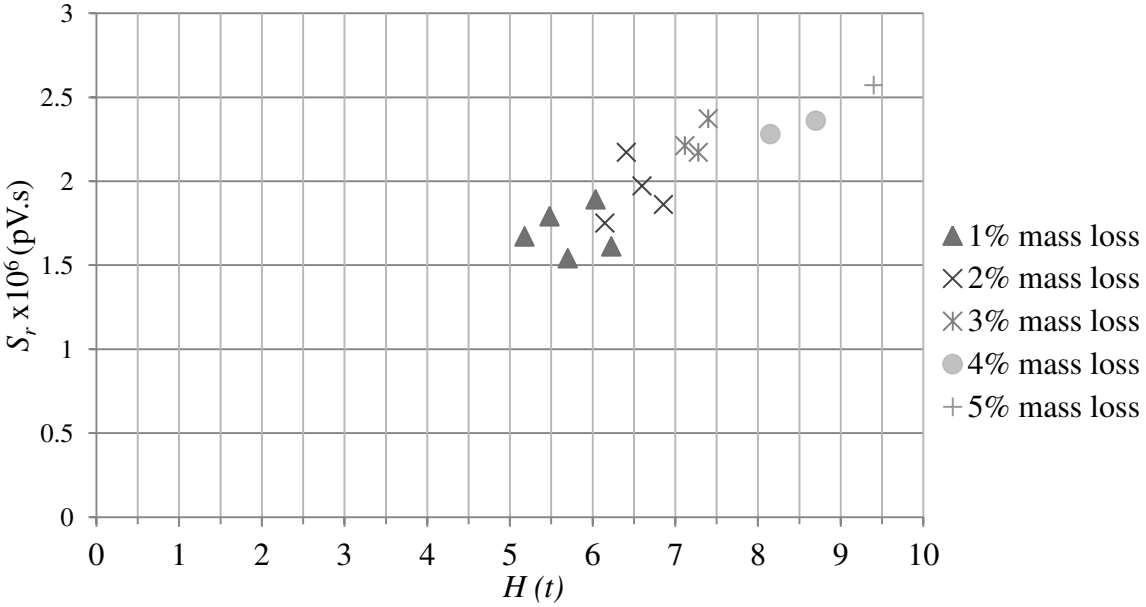

Figure 4.8 Intensity analysis chart for classifying degree of corrosion damage for 20 mm cover samples

4.8 Effect of Cover Crack Growth on Different AE Parameters

The results in **Table 4.1** show that all tested samples exhibited an overall increase in the values of crack width with higher levels of corrosion (higher percentages of steel mass loss). **Figures 4.9-4.11** show the impact of the increase in crack widths on different AE parameters in samples with different cover thickness corroded up to 3% of steel mass loss (20-3-1, 30-3-1, and 40-3-1), as an example. The figures show the variations of the number of hits (**Figure 4.9**), cumulative signal strength (CSS) (**Figure 4.10**), and cumulative energy (CE) (**Figure 4.11**) versus test time. It can be realized from the figures that the increase in crack width as a result of corrosion showed an overall increase in the results of number of hits, CSS, and CE in all tested samples regardless of the cover thickness. These figures, however, demonstrated an increase in number of hits, CSS, and CE before the detection of the first visual crack in these samples. This increase may be related to the movement of chlorides through the sample and further to the depassivation of steel and corrosion initiation.

It is also clear that these graphs exhibited sudden increases at certain times of the test in all tested covers. For instance, the CSS versus time curve for 40-3-1 (**Figure 4.10**) has two points of sudden activity at nearly 120 hr and 205 hr. The first sudden change, at about 120 hr, is mostly related to the onset of steel corrosion, which also showed a significant increase in the number of hits and CE (**Figures 4.9 and 4.11**). On the other hand, the second point, at almost 205 hr, can be correlated to the inception of micro-cracking resulting from the rebar expansions, which is due to the accumulation of corrosion products. This increased AE activity was further confirmed by the detection of

the first visual crack (width of 0.08 mm) in this sample (40-3-1) at 240 hr (**Table 4.1**). After these two points of the curve, the results of number of hits, CSS, and CE showed an almost linear increasing trend, indicating further opening of the crack. These detections of sudden changes in number of hits, CSS, and CE curves were used by other researchers to indicate different stages of corrosion of steel in concrete structures (Li et al., 1998; Idrissi and Limam, 2003; Assouli et al., 2005; Ing et al., 2005; Ohtsu and Tomoda, 2008; Ramadan et al., 2008; Di Benedetti et al., 2013; Kawasaki et al., 2013; 2014; Mangual et al., 2013a; 2013b; ElBatanouny et al., 2014; Vélez et al., 2015). It can also be noticed from **Figures 4.9-4.11** that both CSS and CE followed a similar increasing trend in the three tested covers as a result of the cover crack growing. The results of number of hits, CSS, and CE at the end of the test for all tested samples are summarized in **Table 4.6**. The results presented in **Table 4.6** also confirm that increasing cover crack widths (higher percentages of steel mass loss) yielded higher number of hits, CSS, and CE in all tested cover thicknesses. Although these relationships can give an indication of the crack growth by this continuously increasing trend of AE activity, it cannot be applied to quantify the amount of crack width. Instead, an intensity analysis should be performed to assess the extent of cover cracking due to corrosion of embedded steel.

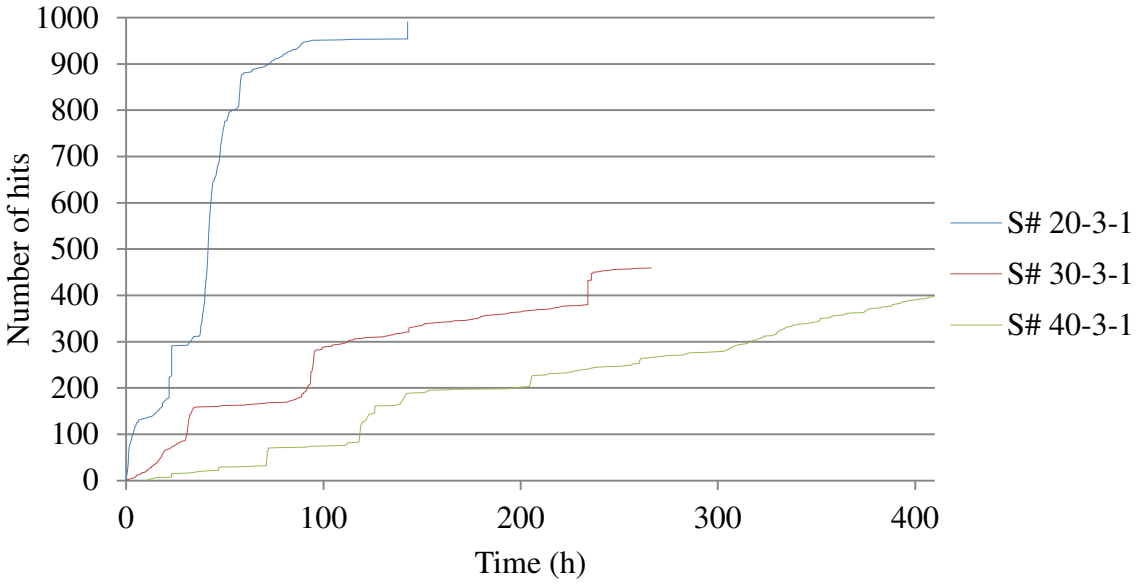

Figure 4.9 Number of collected hits versus test times of samples: 20-3-1, 30-3-1, and 40-3-1

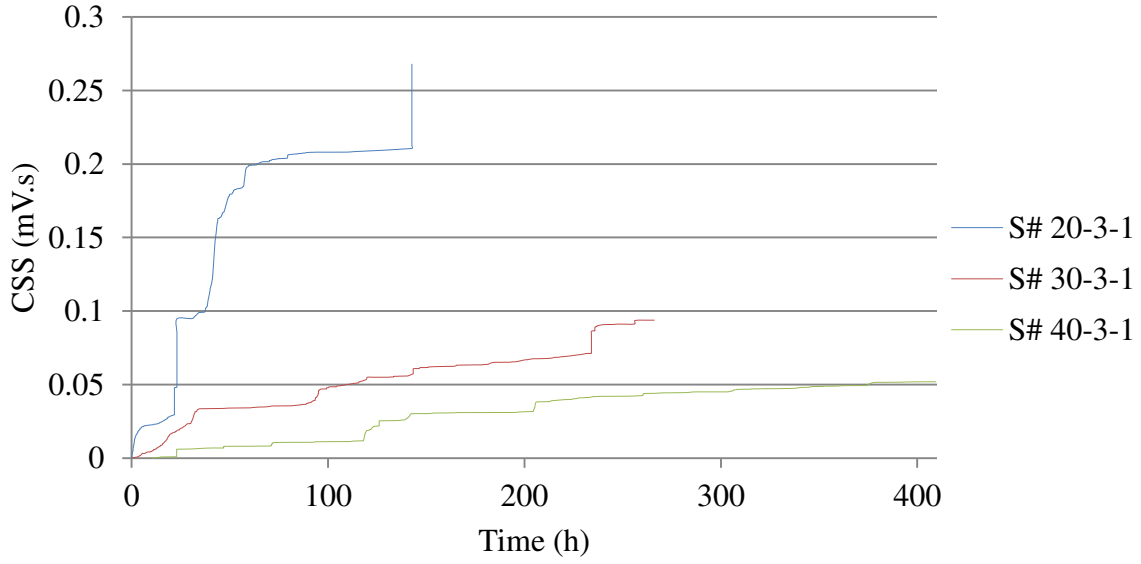

Figure 4.10 CSS versus test time of samples: 20-3-1, 30-3-1, and 40-3-1

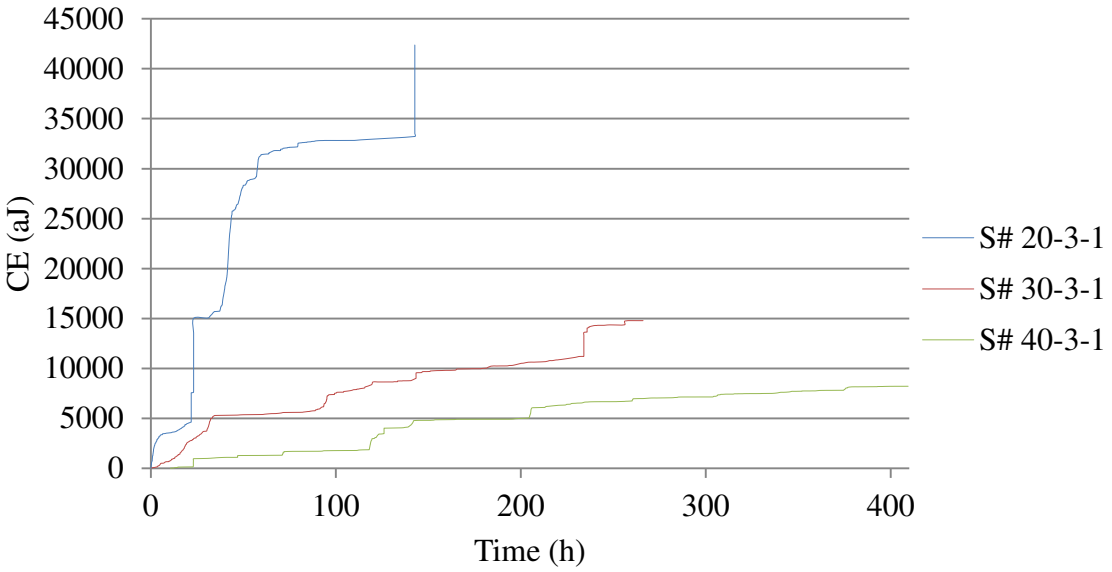

Figure 4.11 CE versus test time of samples: 20-3-1, 30-3-1, and 40-3-1

Table 4.6 Results of number of hits, CSS, CE, amplitude, and peak frequency of all tested samples at the end of tests

Specimen	Number of hits	Cumulative energy (aJ)	Cumulative signal strength (mVs)	Amplitude * (dB)	Peak frequency * (kHz)
20-1-1	380	5480	0.035	81	102
20-1-2	425	6201	0.051	80	103
20-2-1	701	19797	0.126	83	104
20-2-2	715	20185	0.215	85	106
20-3-1	991	42369	0.268	83	105
20-3-2	815	45068	0.218	82	102
20-4-1	1178	37127	0.236	84	107
20-4-2	1325	44582	0.277	83	105
20-5-1	1599	46531	0.296	82	106
20-5-2	1488	46112	0.282	81	110
30-1-1	201	5104	0.032	82	102
30-1-2	124	4717	0.029	84	109
30-2-1	355	9025	0.054	80	104
30-2-2	418	10619	0.067	81	106
30-3-1	459	14790	0.093	84	111
30-3-2	475	11077	0.071	79	104
30-4-1	517	12881	0.079	81	103

30-4-2	599	13151	0.084	82	107
30-5-1	628	17623	0.111	84	111
30-5-2	654	14258	0.091	84	104
40-1-1	117	5390	0.034	77	103
40-1-2	97	3711	0.023	82	103
40-2-1	154	6825	0.048	83	102
40-2-2	223	6177	0.043	85	103
40-3-1	397	8223	0.052	85	107
40-3-2	356	7059	0.049	83	107
40-4-1	510	9857	0.071	84	103
40-4-2	490	8856	0.069	83	102
40-5-1	538	10080	0.076	83	110
40-5-2	597	11817	0.082	84	108

* The values of amplitude and peak frequency represent the maximum value of all detected signals in each sample

4.9 Effect of Cover Thickness on Different AE Parameters

Figures 4.9-4.11 presented a comparison between number of hits, CSS, and CE of three samples with three varied clear concrete covers corroded up to 3% of steel mass loss throughout the test duration. In addition, **Table 4.6** shows the amount of these AE parameters at the end of the tests for all remaining samples. Moreover, **Figure 4.12** contains the distribution of the amplitude of all detected AE signals in the same selected samples (samples 20-3-1, 30-3-1, and 40-3-1) during the test period. **Table 4.6** also presents the value of the maximum amplitude and peak frequency in all tested samples recorded during the whole length of the tests. It is obvious from **Figures 4.9-4.11** that increasing the cover thickness from 20 to 40 mm resulted in an overall reduction of the number of hits, CSS, and CE in these samples. This reduction was also confirmed at other degrees of steel mass loss in all tested samples, as shown in **Table 4.6**. It should be

mentioned that this reduction is mostly attributed to the higher crack widths in samples with 20 mm covers than their 30 and 40 mm counterparts, as seen in **Table 4.1**.

On the other hand, **Figure 4.12** indicates no significant variation in the amplitude values, which ranged from 45 to 85 dB, among all detected AE hits in these three samples. These results were also verified in all tested samples shown in **Table 4.6**, indicating that all samples showed similar values of maximum amplitude of all acquired AE signals. The results of the peak frequencies in all samples in **Table 4.6** also confirmed no significant variations between different samples with the same cover thickness. The values of peak frequency of all signals of the tested samples showed a wide range from 19 to 111 kHz. It should be noted that increasing the cover thickness may contribute to the wave attenuation, thus affecting all AE signal parameters. However, this effect was not pronounced in the tested values of cover thickness (up to 40 mm) reported in this study. Further research should investigate the effect of higher values of cover thicknesses (> 40 mm) on different AE signal parameters.

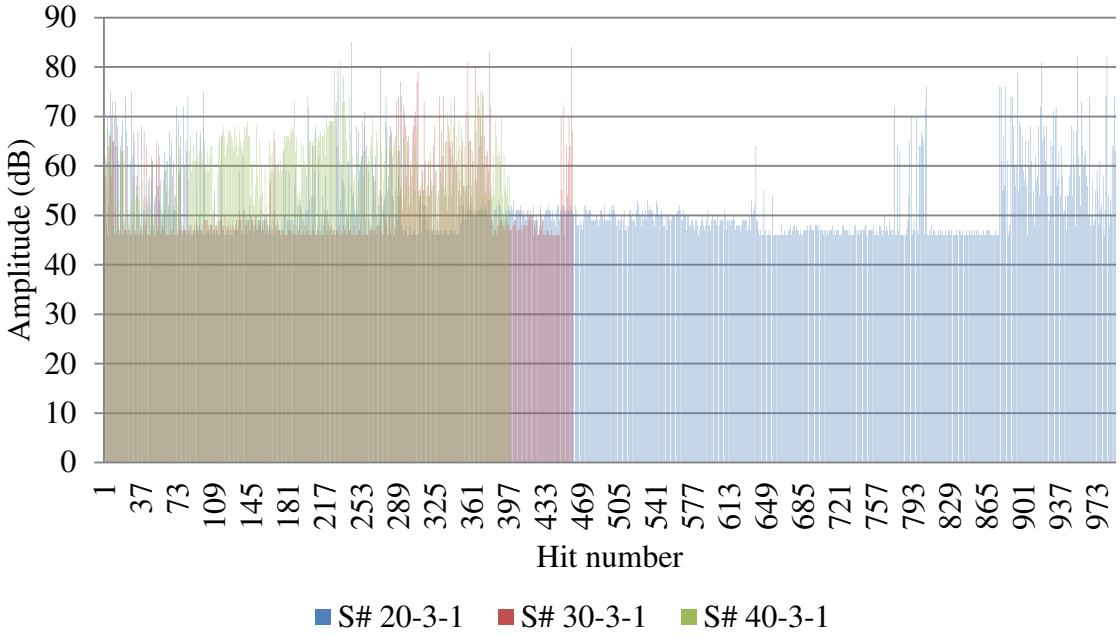

Figure 4.12 Amplitude of all hits acquired for samples: 20-3-1, 30-3-1, and 40-3-1

4.10 Evaluation of Cover Crack Growth Using AE Intensity Analysis

The signal strength values were further analyzed to quantify the cover crack growth in all tested samples of different cover thickness. Thus, an intensity analysis on the signal strength values of all acquired signals of each tested sample was completed to obtain two parameters (*H (t)* and S_r). The values of these parameters were calculated continuously throughout the test for all tested samples, as previously explained. For example, **Figures 4.13-4.14**, respectively, compare the values of *H (t)* and S_r of samples 20-3-1, 30-3-1, and 40-3-1 corresponding to the cover crack growing.

4.10.1 Effect of Cover Crack Growth on $H(t)/S_r$

The results in **Figure 4.13** indicate that increasing the crack width (after being visually detected) yielded an almost linear increase in the values of *H (t)* in all samples regardless

of cover thickness. It can also be seen that the values of *H (t)* were only influenced by the cover crack width values and not by the cover thickness. It is also clear that the values of historic index did not significantly increase after the first crack detection. The values of historic index showed an increase of only 21%, 27%, and 35% due to the crack growth from 0.08 to 0.72 in sample 40-3-1, from 0.11 to 0.78 in sample 30-3-1, and from 0.15 to 0.9 in sample 20-3-1. These results indicate that most of the recorded AE activity occurred at the stages of bar expansion due to corrosion products as well as the micro-cracking of the surrounding concrete. This finding may also be attributed to the wave attenuation that may be due to the crack opening.

Similarly, **Figure 4.14** follows an overall increasing trend of the values of severity due to the increase in crack widths. For instance, samples 40-3-1, 30-3-1, and 20-3-1 witnessed an increase of 28%, 33%, and 32% of the original values recorded upon detection of the first visual crack. The results also confirmed that cover thickness has no significant impact on the values of severity. It can be seen from **Figure 4.14** that different cover samples (20 mm, 30 mm, and 40 mm cover thickness) exhibited similar values of severity at the same values of crack width. It is also obvious that the values of severity did not see a sharp increase after the formation of the first visual cover crack. These results once more indicate that most of the acquired AE signals were related to the early stages of damage at the beginning of visual cover cracking. It is worth noting that other tested samples were corroded to different levels of steel mass loss and crack widths, yet they showed similar behaviour to the samples presented in **Figures 4.13-4.14**.

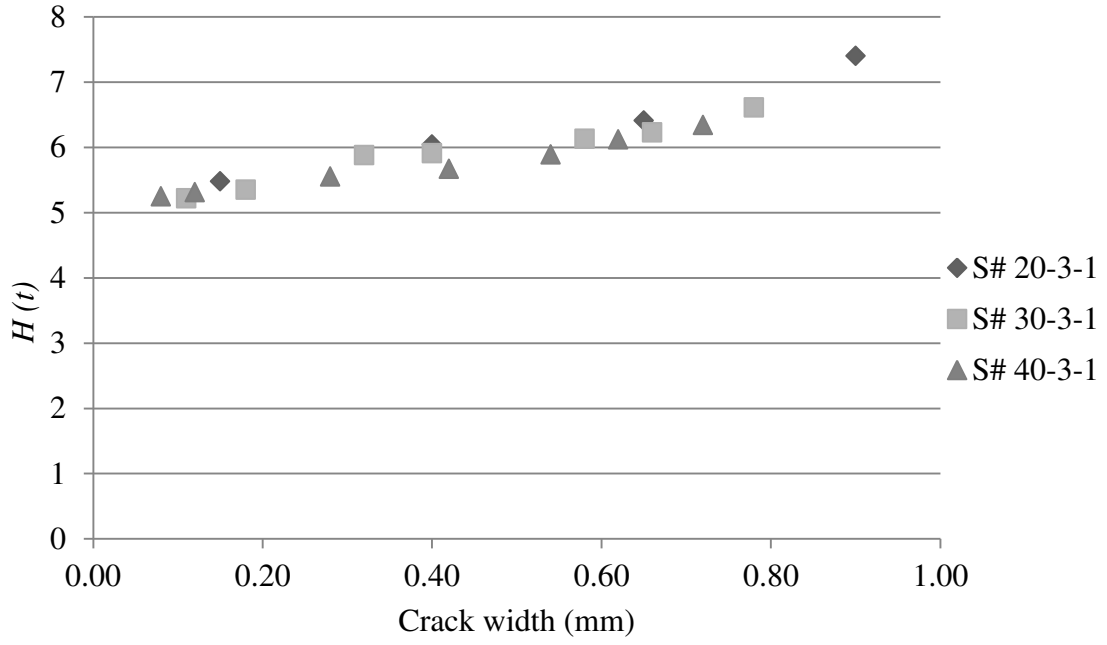

Figure 4.13 *H (t)* versus crack width in samples: 20-3-1, 30-3-1, and 40-3-1

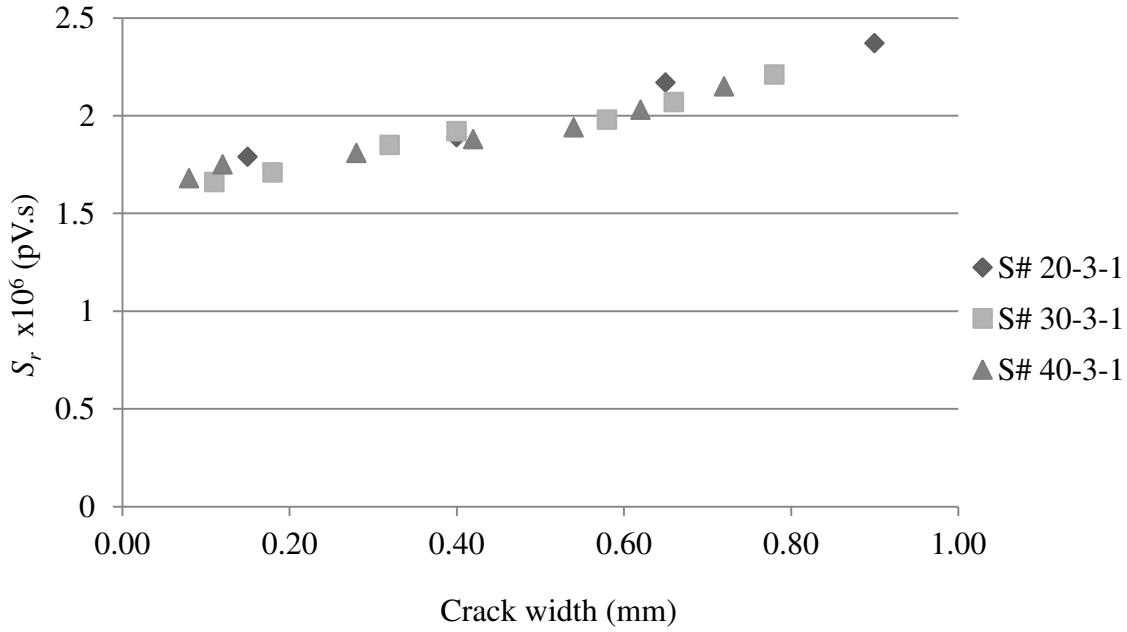

Figure 4.14 S_r versus crack width in samples: 20-3-1, 30-3-1, and 40-3-1

4.10.2 Effect of Cover Thickness on $H(t)/S_r$

The results of the $H(t)$ and S_r for all other tested samples at the end of testing are presented in **Table 4.7**. It can be seen from the table that increasing the steel mass loss from 1% to 5% increased the values of the $H(t)$ and S_r in all tested samples with variable cover thickness. This progression in the percentage of steel mass loss resulted in a continuous growth in the values of cover crack widths. However, the samples with 20 mm cover exhibited higher crack widths than samples with 30 mm and 40 mm cover at all degrees of steel mass loss (see **Table 4.1**). Consequently, the samples with 20 mm cover had higher average values of $H(t)$ and S_r than the average amounts of those samples with both 30 mm and 40 mm covers, as seen in **Table 4.7**. Nonetheless, by comparing the $H(t)$ and S_r values obtained at a certain crack width, samples with different concrete covers were found to have similar values of $H(t)$ and S_r.

The results of crack widths and their corresponding values of $H(t)$ and S_r for all tested specimens were used to develop an intensity classification chart (**Figure 4.15**). This chart is based on the results of cover cracking in reinforced concrete samples with variable cover thickness (20, 30, and 40 mm) due to corrosion of embedded steel. It can be utilized to correlate the different values of historic index and severity calculated based on collecting AE signal strength with the extent of damage in reinforced concrete. These kinds of damage classification charts can be suitable for the assessment of cover cracking in existing concrete structures. It should, however, be mentioned that further investigations are needed to validate the results in this chart using data collected from

actual existing structures, which are exposed to natural deterioration in the form of corrosion of reinforcing steel.

Table 4.7 Results of the *H (t)* and S_r for all tested samples at the end of tests

Sample	*H (t)*	S_r (x10^6) pV.s	Sample	*H (t)*	S_r (x10^6) pV.s	Sample	*H (t)*	S_r (x10^6) pV.s
20-1-1	6.04	1.89	30-1-1	5.11	1.72	40-1-1	5.25	1.87
20-1-2	5.02	1.59	30-1-2	5.21	1.45	40-1-2	4.99	1.55
20-2-1	6.15	1.75	30-2-1	5.71	1.74	40-2-1	5.22	1.67
20-2-2	6.31	1.88	30-2-2	5.89	1.87	40-2-2	5.69	1.81
20-3-1	7.4	2.37	30-3-1	6.61	2.21	40-3-1	6.34	2.15
20-3-2	7.15	2.44	30-3-2	7.25	2.31	40-3-2	6.88	2.36
20-4-1	8.15	2.28	30-4-1	7.47	2.28	40-4-1	7.04	2.25
20-4-2	7.91	2.19	30-4-2	7.66	2.39	40-4-2	7.33	2.12
20-5-1	9.4	2.57	30-5-1	8.17	2.48	40-5-1	7.07	2.37
20-5-2	9.28	2.66	30-5-2	8.23	2.54	40-5-2	7.91	2.49
Average	7.28	2.16	Average	6.73	2.09	Average	6.37	2.06

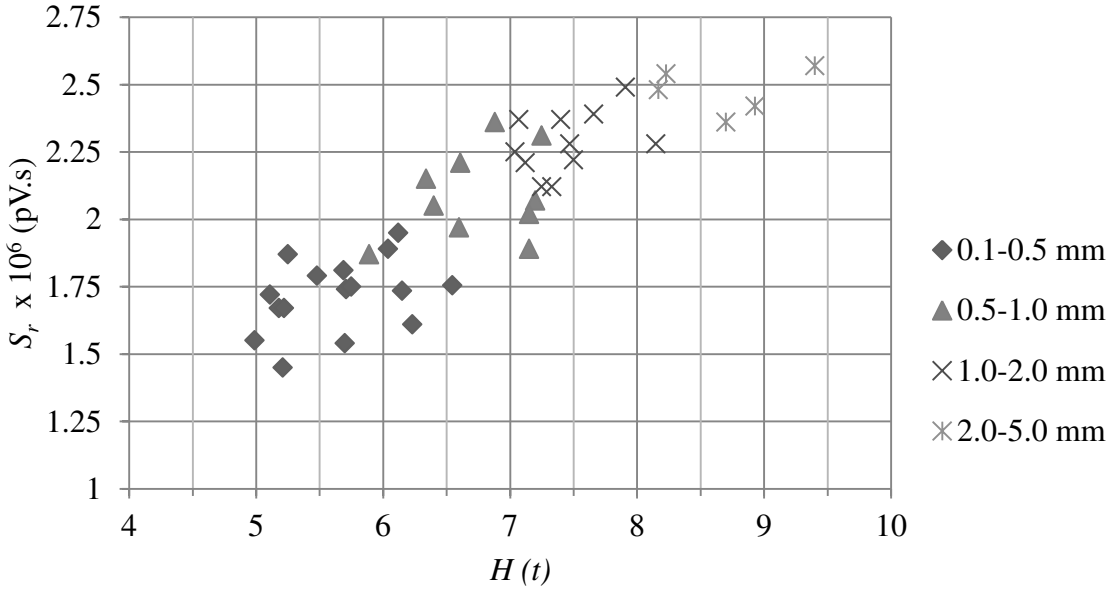

Figure 4.15 Cover crack width classification chart based on the results of the *H (t)* and S_r for all tested samples

4.11 Assessment of Cover Crack Growth by b-value Analysis

The AE data recorded from all tested samples during the accelerated corrosion tests were also utilized to perform a b-value analysis for the purpose of evaluating the cover crack growth resulting from corrosion. This analysis uses the amplitude/number of hits to develop additional parameter defined as b-value. The b-value can then be employed to represent the frequency-magnitude distribution of AE events to aid in evaluating the level of damage. The b-value was constantly calculated for all tested specimens throughout the tests using **Equation 4.3** (Colombo et al., 2003; Kurz et al., 2006; Ohtsu and Tomoda, 2008; Sagar and Prasad, 2013; ElBatanouny et al., 2014; Li et al., 2015; Behnia et al., 2016).

$$log\ N = a - b\ log\ A \qquad \textbf{(4.3)}$$

Where: N = the number of hits having amplitudes larger than A; A = the signal amplitude (dB); a = an empirically derived constant; and b = the b-value (Colombo et al., 2003; Kurz et al., 2006; Ohtsu and Tomoda, 2008; Sagar and Prasad, 2013; ElBatanouny et al., 2014; Li et al., 2015; Behnia et al., 2016).

It is worth noting that, the analysis of the b-value curve may exhibit some nonlinearities, owing to the practical limits of the sensor sensitivity on the low end and the value of maximum amplitude. Therefore, further analysis is recommended to identify and ignore these nonlinearities in the b-value calculation to enhance the accuracy of the results (Butt, 1996). In addition, the use of b-value analysis was only used in this chapter for the purpose of comparison with the intensity analysis.

4.11.1 Effect of Cover Crack Growth on the b-value

Figure 4.16 demonstrates the variations of the magnitudes of b-values throughout the tests for three selected samples with three variable concrete cover thicknesses corroded to 3% of steel mass loss, as an example. Evaluating the changes in the trend of b-values has been used as an indication of the crack evolution in concrete structures (Colombo et al., 2003; Kurz et al., 2006; Sagar and Prasad, 2013; ElBatanouny et al., 2014; Li et al., 2015; Behnia et al., 2016). It can be noticed from **Figure 4.16** that the b-value exhibited a considerable fluctuation throughout the tests in all specimens. However, the three samples showed an overall decreasing trend of b-values until the end of the test, with two zones of sudden increases in b-values. It has been reported that the reduction in the b-values reflects increased AE activity, due to the increase in the number of hits with high amplitudes (Colombo et al., 2003; Kurz et al., 2006; Sagar and Prasad, 2013; ElBatanouny et al., 2014; Li et al., 2015; Behnia et al., 2016). Therefore, the decline of the b-values in these tested samples can be related to the corrosion propagation (depassivation, initiation, micro-cracking, and corrosion-induced crack growth). It is also obvious from **Figure 4.16** that the magnitudes of b-values exhibited lower decline after the visual observation of first crack in all samples (highlighted on the figure) than that before visual cracking. This trend of b-values beyond the detection of visual cracks may be attributed to the attenuation of AE signals through the cracks (ElBatanouny et al., 2014). This impact of signal attenuation was also warranted in other AE parameters considered in this investigation including CE, CSS, $H(t)$, and S_r.

As previously indicated, the b-value curves shown in **Figure 4.16** witnessed two locations of sudden increase in b-values. For example, these two points of sudden increase in the b-values of 40-3-1 can be seen at approximately 120 hr and 205 hr, prior to first visual crack in this sample. Those points can be ascribed to both corrosion and micro-cracking onset, respectively, which were also associated with sudden change in the values of the number of hits and CSS. This finding indicates the effectiveness of the b-value analysis in the early identification of cover cracking (at the micro-cracking stage) prior to visual observation of cracks in all specimens. It is worth noting that, the points of large b-values (representing low AE activity) were contributed to the onset of corrosion and small cracks in a similar study (Ohtsu and Tomoda, 2008). On the contrary, the locations of low b-values can be correlated to the nucleation of relatively large cracks resulting from the bar expansion owing to the accumulation of corrosion products leading to visible cover cracking (Ohtsu and Tomoda, 2008). It should be mentioned that all other tested samples (with varied corrosion levels and cover thicknesses) followed similar trend of variation in the b-values to those described in **Figure 4.16**.

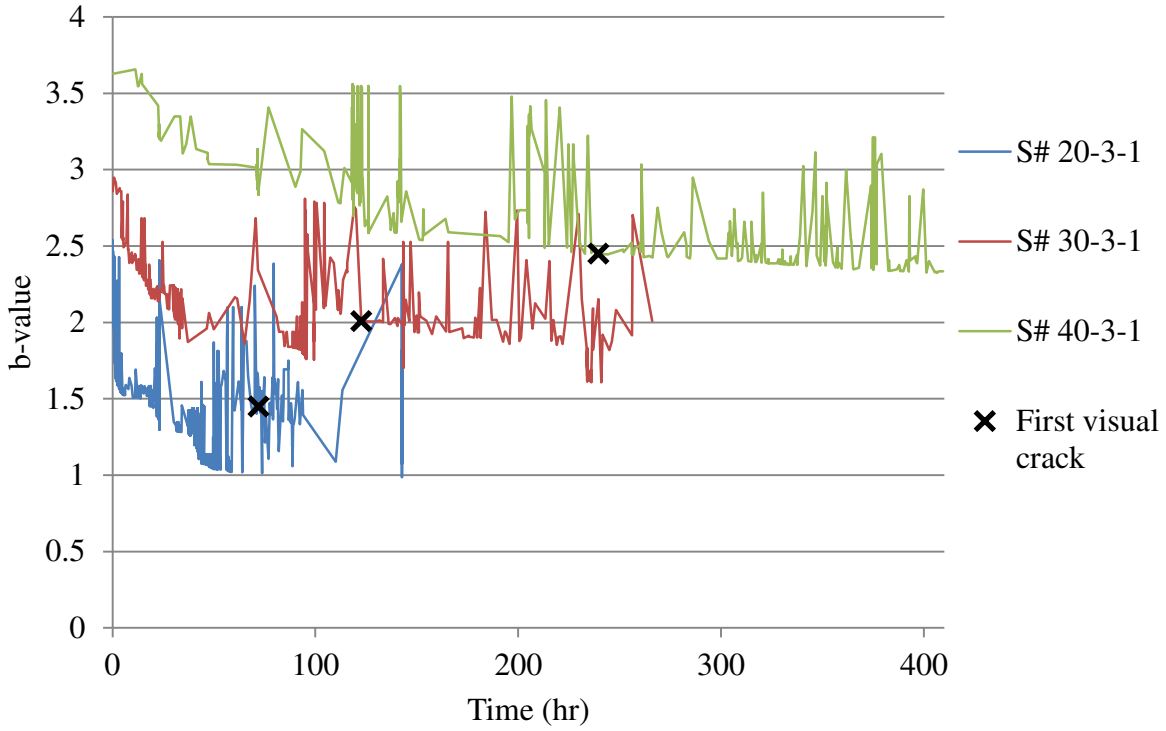

Figure 4.16 b-value versus test time of samples: 20-3-1, 30-3-1, and 40-3-1

4.11.2 Effect of Cover Thickness on the b-value

As previously noted, the growth of cracks in the tested samples throughout the tests was associated with a general decline in the b-values reaching almost the minimum b-value at the end of the test periods (**Figure 4.16**). The b-values of all tested specimens obtained at the end of the tests and their corresponding values of corrosion-induced cover crack widths are demonstrated in **Figure 4.17**. It can be seen from **Figure 4.17** that the increase of cover crack growth was seen to reduce the b-values at all values of cover thicknesses (20, 30, and 40 mm). These trends have been also confirmed in a number of investigations dealing with the b-value analysis of crack development in concrete structures (Colombo et al., 2003; Kurz et al., 2006; Sagar and Prasad, 2013; ElBatanouny

et al., 2014; Li et al., 2015; Behnia et al., 2016). It is also noticeable that the rate of decrease in the b-values was reduced after the formation of relatively large cracks (more than 1 mm) in all samples. It can also be seen that the samples with larger cover thickness yielded higher b-values at similar magnitudes of crack widths. These variations in the b-values can be attributable to the differences in the test durations of the samples with different cover specimens to obtain similar values of final crack widths (**Table 4.1**). These results suggest that intensity analysis parameters ($H(t)$ and S_r) were more sensitive than the b-values to the extent of crack growth irrespective of cover thickness. Therefore, the intensity analysis was solely used in the subsequent chapters to assess the extent of damage of all tested elements.

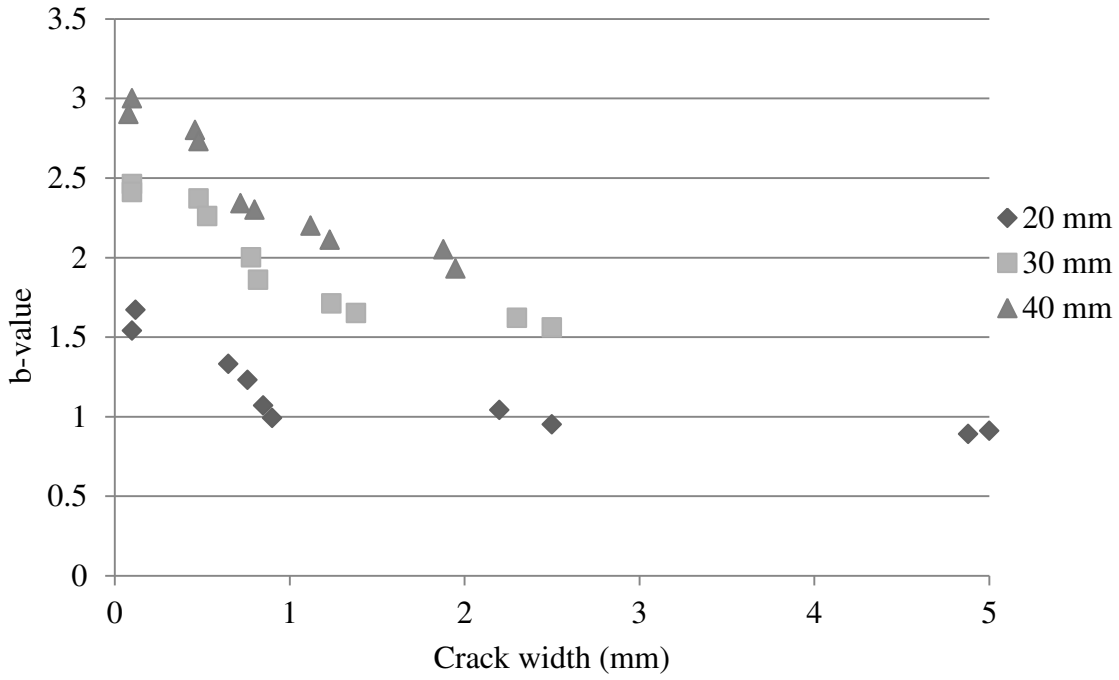

Figure 4.17 b-value versus crack width in all tested samples: 20, 30, and 40 mm cover thickness specimens

5. Discussion of Results from Experimental Study 2: Corrosion Detection and Crack Growth Monitoring in Full-Scale RC Beams

5.1 Introduction

The tested beams in this investigation were subjected to four variable periods of accelerated corrosion process to reach four levels of corrosion in terms of steel mass loss (5%, 10%, 20%, and 30%). These levels of steel mass loss also yielded corrosion cover cracking at the exposed end of all beams, as can be seen from **Table 5.1**. All beams exhibited two cracks observed along the bonded length (subjected to chloride solution) of the two main bars (one crack at each beam side). **Table 5.1** presents the maximum measured values of crack widths at the end of corrosion periods of all beams, which showed larger crack widths with higher percentage of steel mass lass. It can also be seen from **Table 5.1** that the percentages of both the theoretical and actual steel mass loss indicated good agreement in all tested beams.

Table 5.1 Results of the accelerated corrosion tests of all tested beams

Beam	Theoretical mass loss (%)	Actual mass loss (%)	Exposure time (days)	Time to first crack (days)	Maximum crack width (mm)
B1	5	4.5	25	14	0.6
B2	10	9.2	34	15	0.9
B3	20	18.3	52	15	1.2
B4	30	27.9	70	15	2.5
B5	30	29.7	70	14	3.0

5.2 Identification of Corrosion Initiation in Full-Scale RC Beams Using AE Analysis and HCP Test

The analysis of the AE data in this study including AE data filtering and intensity analysis were completed similar to that done in the previous chapter. As previously explained, the variations in the cumulative number of hits and CSS were analyzed throughout the tests to detect corrosion initiation in all tested beams. Besides, the intensity analysis parameters (*H (t)* and S_r) were also used to confirm this detection and to eventually assess the level of corrosion damage. **Figure 5.1** represents the typical variations of these AE parameters for Sensor 2 of B1, as an example for all other tested beams. It can be seen from **Figure 5.1a, b, and d** that the values of cumulative number of hits, CSS, and S_r witnessed an overall increase until the end of corrosion period. This overall increase in these AE parameters can be attributed to both corrosion initiation and propagation in the exposed parts of the steel bars reaching 5% of mass loss and causing a maximum cover crack value of 0.6 mm (**Table 5.1**). The values of *H (t)*, on the other hand, showed fluctuations throughout the test period with some specific points of noticeable peak values of *H (t)*. For example, the first peak point of *H (t)* with a value of 1.41 can be noticed from **Figure 5.1c** at nearly 9.8 days. This point was also associated with a clear slope change in the curves of the cumulative number of hits, CSS, and S_r as shown in **Figure 5.1a, b, and d**. This point of sudden AE activity can be related to the occurrence of corrosion initiation, which is followed by the onset of micro-cracking at the concrete-to-steel interface. The identification of corrosion initiation by locating the points of sudden AE activity was also confirmed in a number of similar experimental studies (Ohtsu et al., 2011; Mangual et al., 2013a, 2013b; Di Benedetti et al., 2013, 2014).

(a)

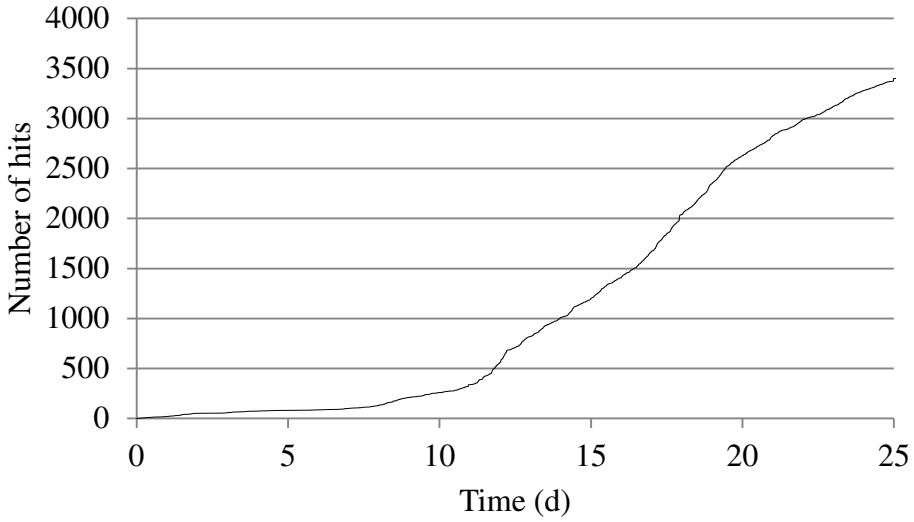
4000
3500
3000
2500
2000
1500
1000
500
0
Number of hits
0
5
10
15
20
25
Time (d)

(b)

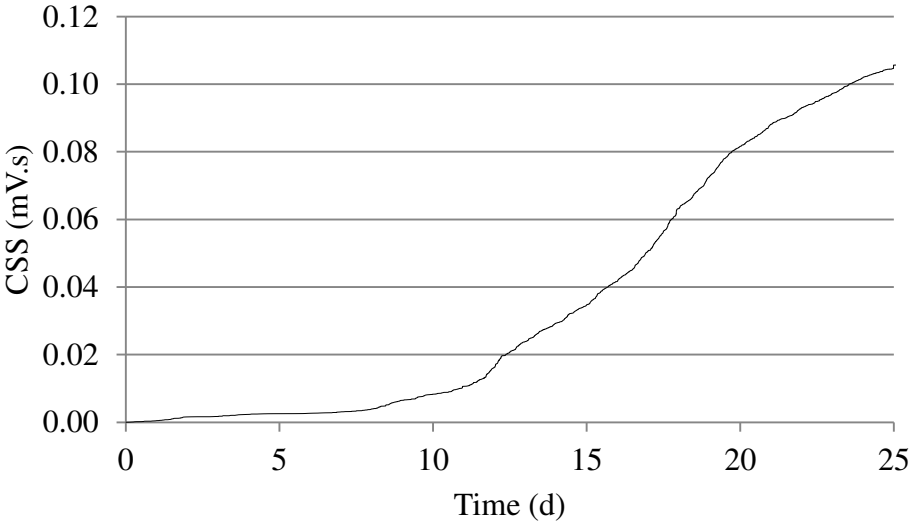
0.12
0.10
0.08
0.06
0.04
0.02
0.00
CSS (mV.s)
0
5
10
15
20
25
Time (d)

(c)

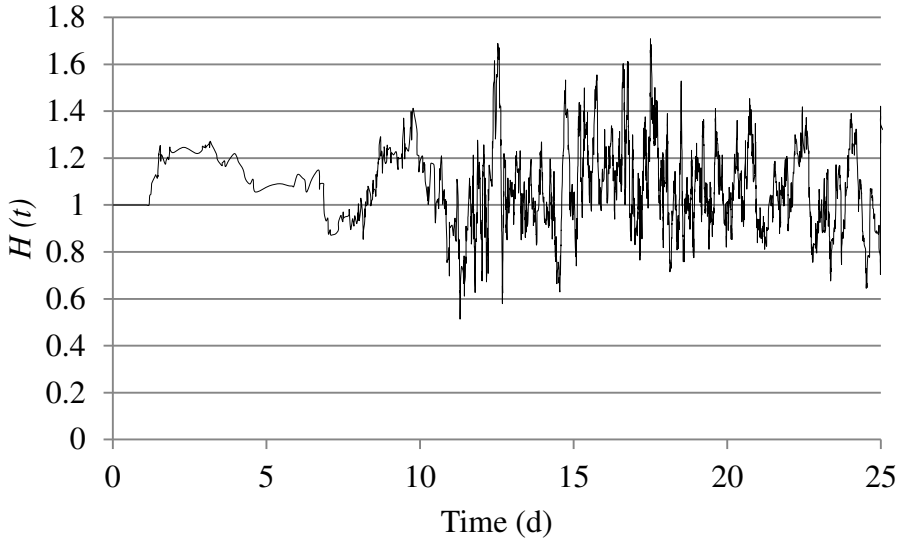

(d)

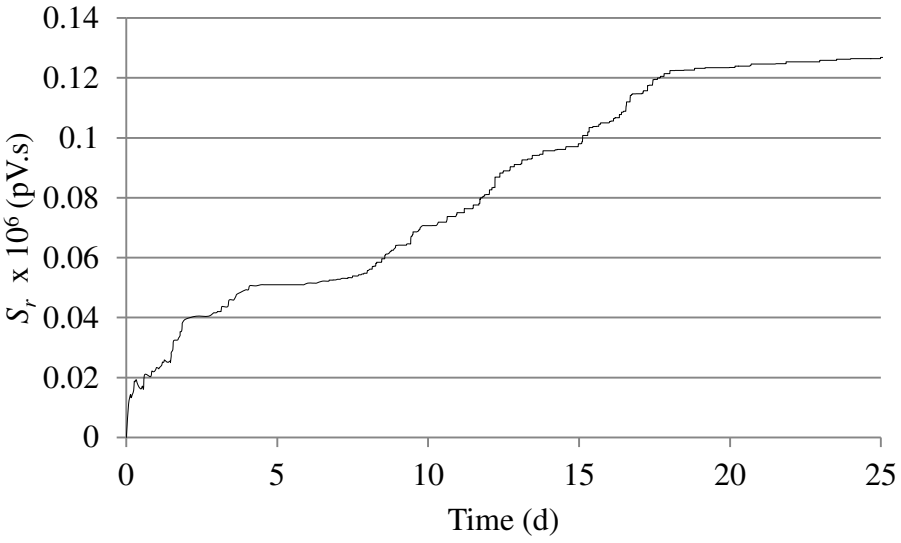

Figure 5.1 Typical variations of AE parameters versus test time of B1 recorded by Sensor 2: (a) cumulative number of hits, (b) CSS, (c) *H (t)*, and (d) S_r

The analysis of AE parameters (cumulative number of hits, CSS, *H (t)*, and S_r) enabled the recognition of corrosion onset (increased AE activity) at times ranged between 9.8 and 10.7 days from all sensors in all tested beams. At these times, no visibe signs of

corrosion or cover cracks were noticed in any of the tested beams. It should be noted that, this detected corrosion activity was expected to be a distributed corrosion along the exposed part of the bar, which was confirmed from the subsequent corrosion propagation. The magnitudes of the previously defined AE parameters at the time of corrosion initiation of all tested beams are summarized in **Table 5.2**. To compare the AE detection of corrosion start in all tested beams, the half-cell potential (HCP) results were reviewed throuhout the test periods, as demonstrated in **Figure 5.2**. The HCP reading of more negative than -350 mV indicates more than 90% probability that reinforcing steel corrosion is occurring according to ASTM C876 (ASTM, 1999). Following this approach, the HCP tests detected corrosion initiation in all tested beams at 13-14 days from the beginning of test. These results manifested the capability of AE monitoring to detect corrosion initiation earlier than both the HCP method and visual observation of corroion-induced cracks. It was also found that all the three sensors within the same beam enabled this early AE detection of corrosion start, with some variations in the absolute values of different AE parameters (**Table 5.2**) among the texted beams. This finding indicated that AE sensors have the ability to detect localized corrosion in RC beams within a range of damage location of 0.2 to 1.505 m. These finding confirmed the outcomes of the previously presented study on the small-scale RC samples (**Chapter 4**). However, the magnitudes of cumulative number of hits, CSS, and S_r at the time of corrosion detection showed to be affected by the specimen size, when compared with those obtained from the small-scale samples. These varied values of AE parameters may be related to the different number of the main reinforcing bars exposed to corrosion between small- and full-scale samples (one bar in small samples versus two bars in all beams). On the other hand, non-

significant changes in the average values of *H (t)* associated with corrosion detection of the teseted beams in comparison to the those values reported in the previous chapter (**Table 5.2**).

Table 5.2 Different AE parameters at corrosion detection in all tested beams

Beam	Cumulative number of hits			CSS (mV.s)			*H (t)*			S_r x 10^6 (pV.s)		
	Sensor 1	Sensor 2	Sensor 3	Sensor 1	Sensor 2	Sensor 3	Sensor 1	Sensor 2	Sensor 3	Sensor 1	Sensor 2	Sensor 3
B1	489	352	165	0.016	0.008	0.004	1.69	1.41	1.31	0.088	0.072	0.055
B2	506	378	173	0.021	0.008	0.005	1.51	1.33	1.29	0.079	0.069	0.046
B3	559	332	176	0.015	0.007	0.004	1.59	1.51	1.18	0.089	0.071	0.049
B4	678	397	191	0.013	0.006	0.003	1.65	1.46	1.23	0.093	0.065	0.057
B5	429	190	46	0.007	0.003	0.001	1.48	1.13	1.05	0.077	0.044	0.032

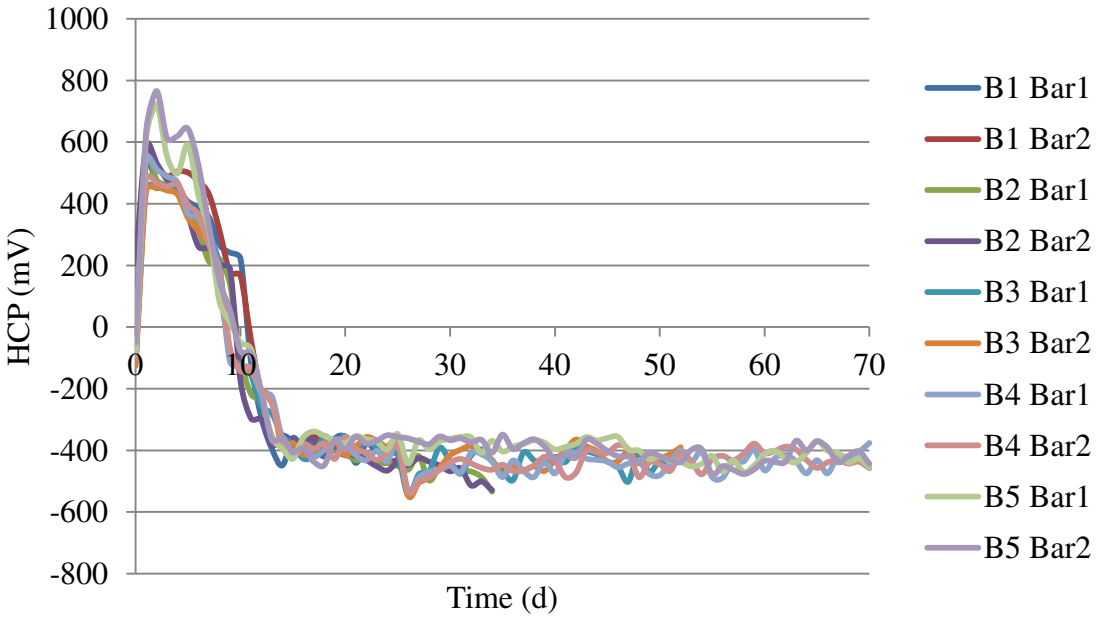

Figure 5.2 HCP versus test time of all tested beams

5.3 Identification of Corrosion-Induced Cover Cracking in Full-Scale RC Beams Using AE Analysis

After corrosion initiation, the analysis of the abovementioned AE parameters was continued to attain an early detection of cover cracking due to the expansive nature of corrosion products. The first visual crack was observed in all tested beams at 14-15 days from the beginning of the corrosion exposure in all tested beams (**Table 5.1**). A second peak in the values of *H (t)* reaching a value of 1.69 was noticed at nearly 12.5 days in B1, as shown in **Figure 5.1c**. At this location, a clear slope change in the curves of the cumulative number of hits, CSS, and S_r was also noticed, as demonstrated in **Figure 5.1a, b, and d**. The high AE activity is mostly ascribed to the growth of macro-cracking leading to cover cracks, which were visually later observed at the side of all tested beams. It is worth noting that the growth of both micro- and macro-cracking is considered one of the important sources of acoustic emission (Fowler et al., 1989). The identification of cover crack growth using the data from the three sensors in all tested beams was similarly performed and showed to occur at approximately 11.2-12.9 days. **Table 5.3** reports the results of AE parameters used to identify the first crack in all tested beams including cumulative number of hits, CSS, *H (t)*, and S_r. These results highlighted the effectiveness of the AE technique in the prognosis of corrosion crack growth earlier than their visual observation in all tested beams, regardless of sensor location. This ability of AE analysis to detect crack initiation was also accomplished using the same approach performed on small-scale RC samples (**Chapter 4**). Nonetheless, the values of AE parameters at the time first crack detection exhibited significant variations between both small- and full-scale elements (**Table 5.3**). These changes may be attributed to the differences in both

patterns and widths of the corrosion-induced cracks observed between small- and full-scale RC samples.

Table 5.3 Different AE parameters at first crack detection in all tested beams

Beam	Cumulative number of hits			CSS (mV.s)			*H (t)*			S_r x 10^6 (pV.s)		
	Sensor 1	Sensor 2	Sensor 3	Sensor 1	Sensor 2	Sensor 3	Sensor 1	Sensor 2	Sensor 3	Sensor 1	Sensor 2	Sensor 3
B1	993	720	389	0.038	0.021	0.014	1.98	1.67	1.25	0.108	0.089	0.071
B2	1066	803	512	0.045	0.019	0.011	1.83	1.51	1.18	0.096	0.076	0.058
B3	963	752	403	0.042	0.021	0.016	2.02	1.63	1.31	0.107	0.078	0.066
B4	1020	863	493	0.051	0.025	0.017	1.79	1.55	1.22	0.127	0.087	0.069
B5	917	251	85	0.031	0.009	0.002	1.69	1.17	1.08	0.089	0.081	0.049

5.4 Impact of Corrosion Damage Progression in Full-Scale RC Beams on AE Parameters

The severe corrosion propagation stages were also monitored in all beams up to a maximum percentage of 30% of steel mass loss. This increase in the percentage of steel mass loss was also associated with an overall increase in the studied AE parameters (cumulative number of hits, CSS, *H (t)*, and S_r). **Table 5.4** highlights the results of these AE parameters at the end of the accelerated corrosion tests corresponding to the successive levels of damage of all beams. It can be noticed from **Table 5.4** that an overall increase in the magnitudes of cumulative number of hits, CSS, *H (t)*, and S_r was attributable to changing the corrosion level from 5% through 30% of steel mass loss. For instance, by comparing the data obtained from Sensor 2 of B1 and B4, the increase in corrosion exposure from 5 to 30% of steel mass loss yielded about 53%, 76%, 66%, and 75% higher cumulative number of hits, CSS, *H (t)*, and S_r. Similar increase in these parameters was also seen from varying corrosion level from 5 to 10%, 10 to 20%, and 20

to 30% from all sensors' data. This general increase in the AE parameters was attributed to both the accumulation of the expansive corrosion products and propagation of cover cracks along the bonded length of the exposed bars. This higher AE activity was also credited to the larger crack width of the corrosion cracks observed in beams with higher corrosion levels (**Table 5.1**). These outcomes proved the feasibility of AE analysis in evaluating the progression of corrosion (in terms of steel mass loss and corrosion-induced cover crack growth) in large-scale RC beams, irrespective of sensor position. It is worth noting that, even lower percentages of steel mass loss investigated in the previous study on small-scale samples (**Chapter 4**) warranted larger crack widths than those obtained from the tested beams in the current study (**Table 5.1**). The reduction of crack widths at higher percentages of steel mass loss in this investigation is ascribed to the confinement contribution of stirrups provided as well as larger concrete cover thickness used in full-scale beams. Therefore, a general decline in the values of AE parameters (cumulative number of hits, CSS, *H (t)*, and S_r) was noticed from increasing the specimen size (small- to full-scale samples, as seen in **Table 5.4** compared to the small-scale data (**Chapter 4**).

Table 5.4 Different AE parameters at the end of corrosion exposure in all tested beams

Beam	Cumulative number of hits			CSS (mV.s)			*H (t)*			S_r x 10^6 (pV.s)		
	Sensor 1	Sensor 2	Sensor 3	Sensor 1	Sensor 2	Sensor 3	Sensor 1	Sensor 2	Sensor 3	Sensor 1	Sensor 2	Sensor 3
B1	4972	3400	907	0.433	0.106	0.031	2.31	1.71	1.43	0.315	0.127	0.075
B2	6252	4556	955	0.602	0.175	0.034	3.72	3.15	1.57	0.483	0.208	0.092
B3	7364	5085	1218	2.12	0.214	0.046	4.97	4.79	1.61	0.536	0.387	0.103
B4	13170	7194	3272	3.21	0.45	0.132	5.73	5.06	1.77	0.781	0.513	0.119
B5	8174	2623	1296	0.702	0.124	0.058	5.66	1.64	1.42	0.638	0.091	0.062

5.5 Influence of Sensor Location on AE Parameters

The results presented in **Tables 5.2-5.4** indicated that the values of all AE parameters obtained from the three sensors in the same beam exhibited significant changes at all levels of damage. These changes were expected from varying the sensor location from the corrosion exposed side from 0.2 to 1.505 m. The increase in the sensor distance from the exposed bars showed to generally reduce the magnitudes of the cumulative number of hits, CSS, $H(t)$, and S_r, in all beams subjected to variable levels of corrosion (corrosion initiation, cover cracking, and end of corrosion exposure). For example, increasing the sensor distance from 0.435 to 1.505 m in B5 at the end of corrosion period resulted in nearly 84%, 92%, 75%, and 90% lower values of the cumulative number of hits, CSS, $H(t)$, and S_r. Similar reductions in the values of these parameters were also obtained from changing the sensor location in all other tested beams at all degrees of damage (**Tables 5.2-5.4**). These overall minimized AE activities can be related to the wave attenuation, which is expected from the signal propagation in concrete due to scattering, reflections, and existence of cracks (Ervin, 2007). This reduced AE activity was also manifested by comparing the magnitudes of AE parameters at different stages of corrosion between small- and full-scale specimens due to increasing the specimen size (farther sensor locations) (**Tables 5.2-5.4** compared to the preceding chapter).

In the meantime, the values of the signal amplitudes showed to decrease by increasing the sensor location, thus reducing the signal strength, CSS, $H(t)$, and S_r. **Figure 5.3** demonstrates the influence of sensor location on the amplitude of the signals detected at the time of corrosion initiation with the three sensors in all tested beams. It can be

observed from **Figure 5.3** that the farther the sensor from the corroded bars, the lower the amplitude of the same signal detected by these sensors in each beam. For instance, by comparing the signal amplitudes recorded by Sensors 1 and 3 in B1, B2, B3, B4, and B5, it was found that increasing sensor distance led to approximately 6%, 7%, 5%, 6%, and 13% lower amplitudes, respectively. These lower amplitudes resulted in a general decline trend in the values of the cumulative number of hits, CSS, $H(t)$, and S_r (**Tables 5.2-5.4**). It was also noticed that B5 exhibited the maximum influence of sensor location on different AE parameters owing to the larger span of this beam compared to other beams. However, all sensors allowed the detection of all degrees of corrosion damage with a maximum sensor distance of 1.505 m from the source of damage investigated in this investigation.

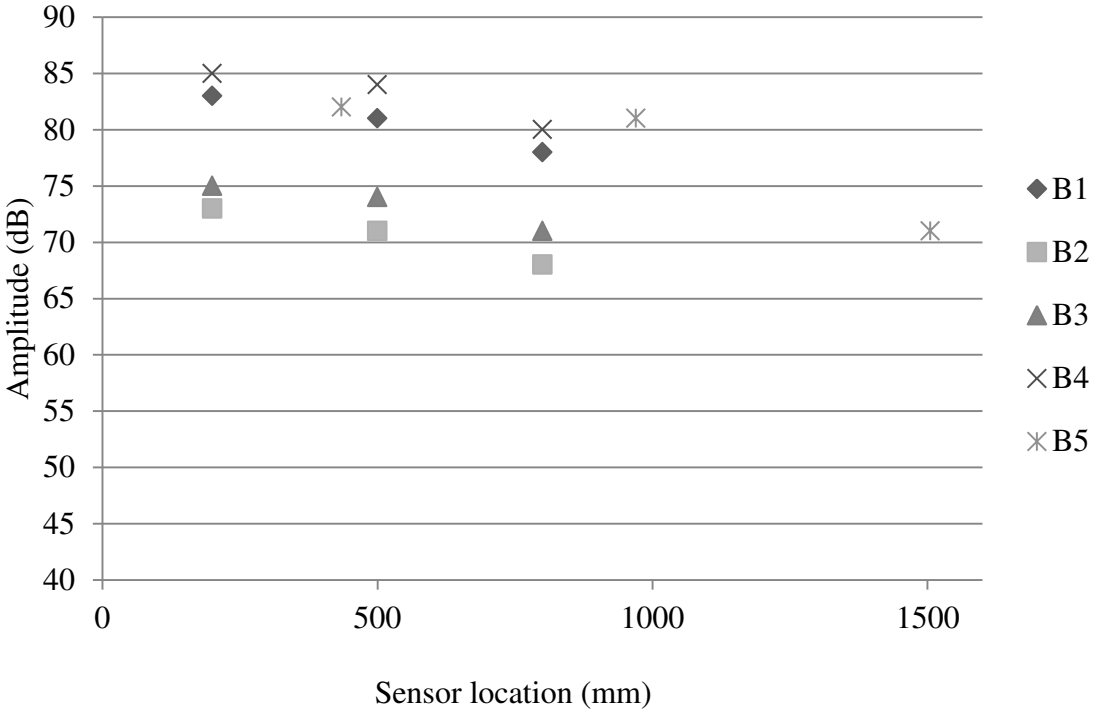

Figure 5.3 Effect of sensor location on the amplitude of the signals detected at corrosion initiation

5.6 Corrosion Damage Quantification in Full-Scale RC Beams Using AE Intensity Analysis

The results of AE parameters analyzed in this study (cumulative number of hits, CSS, *H (t)*, and S_r) showed that these parameters were sensitive to capture the different levels of corrosion degradation until obtaining 30% of steel mass loss. More specifically, the average results of *H (t)* and S_r acquired from the three sensors attached to each beam were calculated and graphed to classify the extent of corrosion propagation. **Figure 5.4** correlates the average *H (t)* and S_r with different stages of corrosion damage including corrosion initiation, first crack detection, 5%, 10%, 20%, and 30% of steel mass loss. Likewise, the ranges of corrosion-induced cover crack widths were related to the

corresponding average values of $H(t)$ and S_r, as described in **Figure 5.5**. This figure categorizes the maximum values of corrosion cover crack growth into four ranges (0.5-0.6 mm, 0.7-0.9 mm, 1.0-2.4 mm, and 2.5-3.0 mm) according to the calculated values $H(t)$ and S_r from all tested beams. Using these classification charts, the severity of corrosion level as well as corrosion-induced crack widths can be predicted using the AE data attained from continuous AE monitoring of corrosion in RC structures. It is worth noting that, further testing on larger number/size beams is required to tolerate the effects of specimen size/sensor location and number/configuration of main and secondary reinforcement. Eventually, these further tests (on larger number/size beams) are expected to improve the accuracy of the developed classification charts (**Figure 5.4-5.5**).

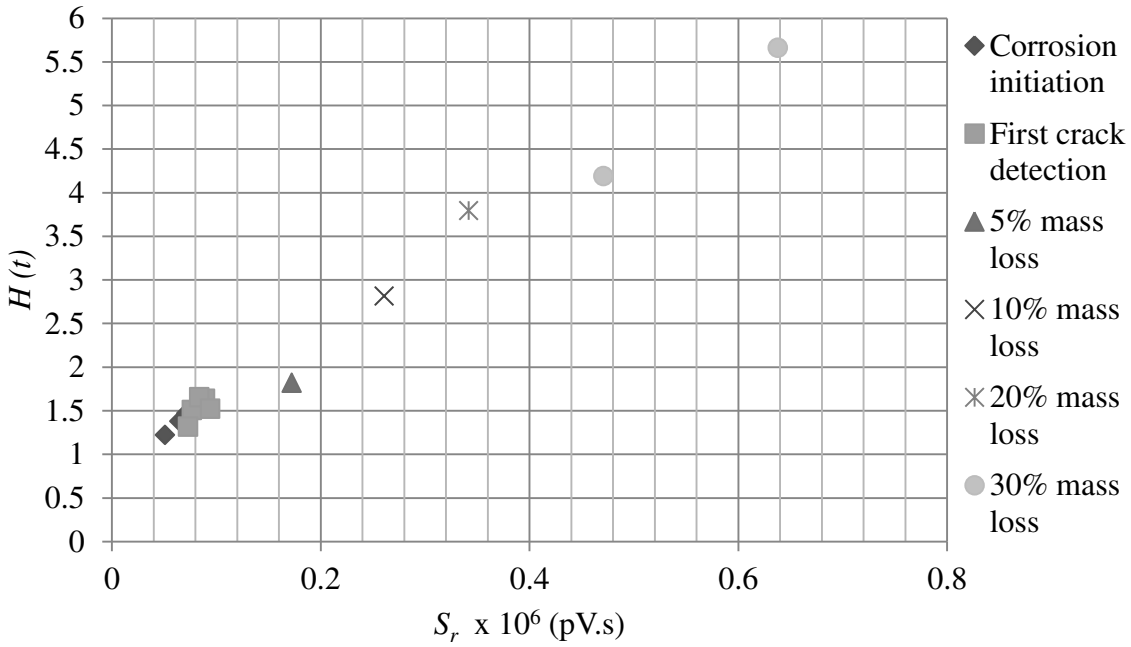

Figure 5.4 Corrosion degree classification chart of full-scale RC beams

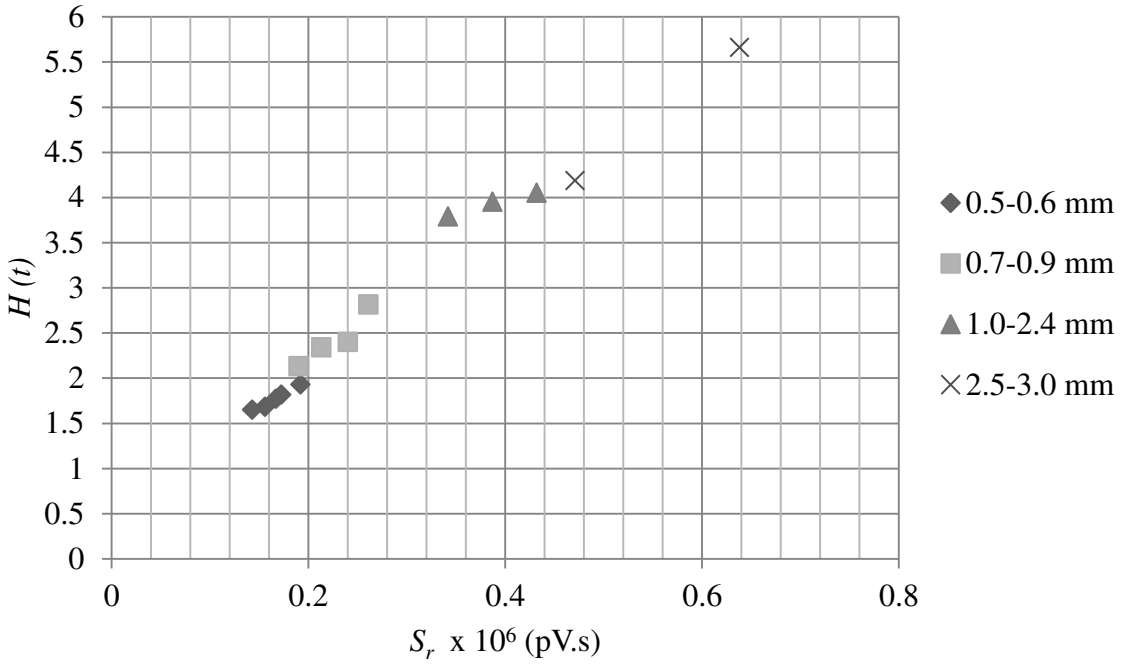

Figure 5.5 Cover crack growth classification chart of full-scale RC beams

6. Discussion of Results from Experimental Study 3: Evaluation of Concrete-Steel Bond Behaviour in Small-Scale Corroded/Un-Corroded RC Samples

6.1 Introduction

Tables 6.1-6.2 summarize the results obtained from the pull-out tests performed on all tested samples (corroded and un-corroded). These results consist of the mode of failure, maximum load, bond strength (bond stress at the maximum recorded load), both the load and stress at the onset of micro-cracking detected using AE analysis, and values of free end slip at maximum load. The results presented in **Tables 6.1-6.2** will be compared to the results acquired from AE monitoring to evaluate the bond behaviour in all tested samples.

Table 6.1 Summary of pull-out tests results for all corroded tested samples

Sample designation	Failure mode	Maximum load (kN)	Bond strength (MPa)	Free end slip at maximum load (mm)	Micro-cracking load (kN) *	Micro-cracking stress (MPa) *
20M20A1-1	Splitting cracks	24	7.64	0.17	18	5.73
20M20A1-2	Splitting cracks	28	8.92	0.19	16	5.10
20M20C1-1	Broken	61	4.86	0.52	45	3.58
20M20C1-2	Broken	65	5.18	0.53	52	4.14
20M20A2-1	Splitting cracks	16	5.10	0.14	12	3.82
20M20A2-2	Splitting cracks	28	8.92	0.17	18	5.73
20M20C2-1	Broken	60	4.78	0.54	48	3.82
20M20C2-2	Broken	57	4.54	0.45	51	4.06
20M20A3-1	Splitting cracks	22	7.01	0.15	16	5.10
20M20A3-2	Splitting cracks	19	6.05	0.14	15	4.78
20M20C3-1	Broken	45	3.58	0.38	40	3.18
20M20C3-2	Broken	55	4.38	0.41	49	3.90
20M20A4-1	Splitting cracks	22	7.01	0.13	16	5.10
20M20A4-2	Splitting cracks	16	5.10	0.09	12	3.82

20M20C4-1	Broken	43	3.42	0.28	38	3.03
20M20C4-2	Broken	47	3.74	0.33	40	3.18
20M20A5-1	Splitting cracks	15	4.78	0.07	12	3.82
20M20A5-2	Splitting cracks	18	5.73	0.08	14	4.46
20M20C5-1	Splitting cracks	34	2.71	0.26	30	2.39
20M20C5-2	Splitting cracks	36	2.87	0.27	33	2.63
20M30A1-1	Splitting cracks	33	10.51	0.24	23	7.32
20M30A1-2	Splitting cracks	32	10.19	0.22	21	6.69
20M30C1-1	Broken	75	5.97	0.71	50	3.98
20M30C1-2	Broken	72	5.73	0.65	46	3.66
20M30A2-1	Splitting cracks	35	11.15	0.25	15	4.78
20M30A2-2	Splitting cracks	25	7.96	0.19	16	5.10
20M30C2-1	Broken	65	5.18	0.65	43	3.42
20M30C2-2	Broken	70	5.57	0.62	39	3.11
20M30A3-1	Splitting cracks	31	9.87	0.18	18	5.73
20M30A3-2	Splitting cracks	23	7.32	0.16	15	4.78
20M30C3-1	Broken	72	5.73	0.45	41	3.26
20M30C3-2	Broken	71	5.65	0.47	49	3.90
20M30A4-1	Splitting cracks	27	8.60	0.16	21	6.69
20M30A4-2	Splitting cracks	24	7.64	0.13	14	4.46
20M30C4-1	Broken	62	4.94	0.42	45	3.58
20M30C4-2	Broken	79	6.29	0.46	53	4.22
20M30A5-1	Splitting cracks	24	7.64	0.13	19	6.05
20M30A5-2	Splitting cracks	26	8.28	0.14	18	5.73
20M30C5-1	Broken	62	4.94	0.45	36	2.87
20M30C5-2	Splitting cracks	31	2.47	0.33	28	2.23
20M40A1-1	Splitting cracks	33	10.51	0.22	25	7.96
20M40A1-2	Splitting cracks	35	11.15	0.21	24	7.64
20M40C1-1	Broken	92	7.32	0.68	66	5.25
20M40C1-2	Broken	90	7.17	0.63	62	4.94
20M40A2-1	Splitting cracks	32	10.19	0.2	20	6.37
20M40A2-2	Splitting cracks	32	10.19	0.19	22	7.01
20M40C2-1	Broken	85	6.77	0.62	49	3.90
20M40C2-2	Broken	81	6.45	0.56	43	3.42
20M40A3-1	Splitting cracks	29	9.24	0.17	23	7.32
20M40A3-2	Splitting cracks	34	10.83	0.22	15	4.78
20M40C3-1	Broken	76	6.05	0.44	45	3.58
20M40C3-2	Splitting cracks	78	6.21	0.61	47	3.74

20M40A4-1	Splitting cracks	31	9.87	0.16	17	5.41
20M40A4-2	Splitting cracks	29	9.24	0.18	13	4.14
20M40C4-1	Splitting cracks	69	5.49	0.48	53	4.22
20M40C4-2	Splitting cracks	73	5.81	0.49	48	3.82
20M40A5-1	Splitting cracks	39	9.42	0.17	19	6.05
20M40A5-2	Splitting cracks	27	8.60	0.12	17	5.41
20M40C5-1	Broken	68	5.41	0.47	43	3.42
20M40C5-2	Splitting cracks	65	5.18	0.41	47	3.74

* Detected at the beginning of micro-cracking using AE analysis

Table 6.2 Summary of pull-out tests results for all un-corroded tested samples

Sample designation	Failure mode	Maximum load (kN)	Bond strength (MPa)	Free end slip at maximum load (mm)	Micro-cracking load (kN) *	Micro-cracking stress (MPa) *
10M20A0-1	Splitting cracks	20	12.74	0.10	13	8.28
10M20A0-2	Splitting cracks	22	14.01	0.18	14	8.92
10M20B0-1	Splitting cracks	33	10.51	0.25	23	7.32
10M20B0-2	Splitting cracks	35	11.15	0.26	24	7.64
10M20C0-1	Broken	43	6.85	0.26	38	6.05
10M20C0-2	Broken	44	7.01	0.26	29	4.62
20M20A0-1	Splitting cracks	32	10.19	0.16	27	8.60
20M20A0-2	Splitting cracks	34	10.83	0.22	24	7.64
20M20B0-1	Splitting cracks	54	8.60	0.33	31	4.94
20M20B0-2	Splitting cracks	48	7.64	0.26	30	4.78
20M20C0-1	Broken	77	6.13	0.51	48	3.82
20M20C0-2	Broken	77	6.13	0.51	61	4.86
35M20A0-1	Splitting cracks	38	6.92	0.26	20	3.64
35M20A0-2	Splitting cracks	36	6.55	0.17	20	3.64
35M20B0-1	Splitting cracks	54	4.91	0.31	34	3.09
35M20B0-2	Splitting cracks	57	5.19	0.53	36	3.28
35M20C0-1	Broken	77	3.50	0.51	66	3.00
35M20C0-2	Broken	98	4.46	0.51	85	3.87
10M30A0-1	Splitting cracks	23	14.65	0.25	15	9.55
10M30A0-2	Splitting cracks	24	15.29	0.12	14	8.92
10M30B0-1	Bar yield	45	NA	NA	NA	NA
10M30B0-2	Bar yield	52	NA	NA	NA	NA
10M30C0-1	Bar yield	46	NA	NA	NA	NA

10M30C0-2	Bar yield	40	NA	NA	NA	NA
20M30A0-1	Splitting cracks	35	11.15	0.36	15	4.78
20M30A0-2	Splitting cracks	39	12.42	0.15	17	5.41
20M30B0-1	Splitting cracks	57	9.08	0.37	37	5.89
20M30B0-2	Splitting cracks	58	9.24	0.31	49	7.80
20M30C0-1	Broken	77	6.13	0.76	52	4.14
20M30C0-2	Broken	103	8.20	0.75	48	3.82
35M30A0-1	Splitting cracks	51	9.28	0.25	36	6.55
35M30A0-2	Splitting cracks	48	8.74	0.26	23	4.19
35M30B0-1	Splitting cracks	88	8.01	0.76	51	4.64
35M30B0-2	Splitting cracks	74	6.73	0.48	45	4.09
35M30C0-1	Broken	87	3.96	0.78	68	3.09
35M30C0-2	Broken	90	4.09	0.74	76	3.46
10M40A0-1	Splitting cracks	25	15.92	0.19	15	9.55
10M40A0-2	Splitting cracks	26	16.56	0.22	16	10.19
10M40B0-1	Bar yield	40	NA	NA	NA	NA
10M40B0-2	Bar yield	42	NA	NA	NA	NA
10M40C0-1	Bar yield	41	NA	NA	NA	NA
10M40C0-2	Bar yield	44	NA	NA	NA	NA
20M40A0-1	Splitting cracks	38	12.10	0.24	21	6.69
20M40A0-2	Splitting cracks	42	13.38	0.26	12	3.82
20M40B0-1	Splitting cracks	60	9.55	0.27	46	7.32
20M40B0-2	Splitting cracks	85	13.54	0.45	55	8.76
20M40C0-1	Broken	124	9.87	0.78	89	7.09
20M40C0-2	Broken	122	9.71	0.65	54	4.30
35M40A0-1	Splitting cracks	64	11.65	0.47	31	5.64
35M40A0-2	Splitting cracks	48	8.74	0.43	27	4.91
35M40B0-1	Broken	107	9.74	0.69	51	4.64
35M40B0-2	Broken	97	8.83	0.74	45	4.09
35M40C0-1	Broken	134	6.10	0.75	74	3.37
35M40C0-2	Broken	156	7.10	1.17	83	3.78

* Detected at the beginning of micro-cracking using AE analysis

6.2 AE Data Filtering from Bond Tests

The raw AE data recorded during all pull-out tests were filtered to reduce any noise-related signals and/or irrelevant wave reflections within the sample's boundaries. An amplitude-duration-based filter, or Swansong II filter (Fowler et al., 1989), was performed on the original AE results acquired from all tests. This filter has previously been implemented in a number of similar studies involving the application of AE monitoring in concrete structures (for example: ElBatanouny et al., 2014; Abdelrahman et al., 2015; Vélez et al., 2015). The concept of this filtering technique is derived from the assumption that real AE signals with high amplitudes are accompanied by long durations, and vice versa (Abdelrahman et al., 2015). Using this procedure, the acceptance criteria were established after the visual inspection of all recorded AE signals, as demonstrated in **Table 6.3**. By applying these criteria, all signals that did not meet these amplitude-duration ranges were filtered and the remaining AE hits were then considered legitimate emissions generated from bond deterioration until failure. These final AE data were consequently analyzed and evaluated, as will be explained in the following sections. It is worth noting that, the characteristics of AE waveforms recorded in this investigation may vary from those anticipated in existing concrete structures. To overcome this issue, the acceptance limits of the filtering approach utilized in this study may require some minor modifications to take into account any possible difference in the AE waveform signatures obtained from monitoring actual concrete structures. This aim can be achieved by verifying the effectiveness of this filtering approach in filtering AE data acquired from

monitoring in-service concrete structures under similar conditions to enhance the sensitivity of the amplitude-duration limits of this filter.

Table 6.3 Acceptance criteria for AE signals from bond tests

Amplitude range (dB)	Duration (μs)		Amplitude range (dB)	Duration (μs)	
	Lower	Upper		Lower	Upper
$40 \leq A < 45$	0	400	$60 \leq A < 65$	300	1000
$45 \leq A < 48$	0	500	$65 \leq A < 70$	500	2000
$48 \leq A < 52$	0	600	$70 \leq A < 80$	1000	4000
$52 \leq A < 56$	0	700	$80 \leq A < 90$	2000	7000
$56 \leq A < 60$	100	800	$90 \leq A < 100$	3000	10000

6.3 AE Intensity Analysis on the Data from Bond Tests

AE intensity analysis similar to that introduced in the previous chapters was exploited to further develop AE parameters that can better identify and characterize the extent of bond damage in concrete structures. These parameters can then be employed to construct damage intensity classification charts based on the acquired AE signal strength data. Intensity analysis was first applied in fibre-reinforced polymer vessels (Fowler et al., 1989) and has also been utilized for the evaluation of various damage mechanisms of concrete structures (Golaski et al., 2002; Nair and Cai, 2010; Rizzo et al., 2010; ElBatanouny et al., 2014; Abdelrahman et al., 2015; Vélez et al., 2015). The AE signal strength data recorded during the pull-out tests (after being filtered) were subjected to an intensity analysis to assess the bond behaviour of corroded/un-corroded reinforcement to concrete in all specimens. This analysis of AE signal strength yielded two additional AE parameters: historic index ($H(t)$) and severity (S_r). $H(t)$ indicates any sudden variation in the slope of the cumulative signal strength (CSS) curve versus test time. The value of H

(t) was calculated using **Equation 6.1** throughout the pull-out test period in all tested samples (Nair and Cai, 2010; ElBatanouny et al., 2014; Abdelrahman et al., 2015).

$$H(t) = \frac{N}{N-K} \frac{\sum_{i=K+1}^{N} S_{oi}}{\sum_{i=1}^{N} S_{oi}} \quad \textbf{(6.1)}$$

Where: N = the cumulative number of hits up to time *(t)* and S_{oi} = signal strength of the ith event.

In the meantime, S_r is based on the average signal strength of the J hits with the maximum algebraic value of signal strength, and was estimated using **Equation 6.2** for all tested samples (Nair and Cai, 2010; ElBatanouny et al., 2014; Abdelrahman et al., 2015).

$$S_r = \sum_{i=1}^{J} \frac{S_{oi}}{J} \quad \textbf{(6.2)}$$

It is worth noting that the values of the constants K in **Equation 6.1** and J in **Equation 6.2** may depend on the damage mechanism and type of structure (Vélez et al., 2015). Parametric analysis similar to that performed in a study on AE monitoring of prestressed concrete piles (Vélez et al., 2015) can be conducted to obtain the most suitable values of these constants according to the damage mechanism/type of structure. However, for the purpose of this preliminary study, the values of these constants (K and J) were chosen based on reviewing a number of investigations dealing with AE monitoring in concrete structures, such as references: (Nair and Cai, 2010; ElBatanouny et al., 2014; Abdelrahman et al., 2015). The selected values of K and J in this study are mostly used in the literature and proved their suitability for the application of AE intensity analysis in reinforced concrete structures (Nair and Cai, 2010). The value of K was assumed according to the cumulative number of hits, as follows: a) N/A: if $N \leq 50$, b) $K = N - 30$:

if $51 \leq N \leq 200$, c) $K = 0.85N$: if $201 \leq N \leq 500$, and d) $K = N - 75$: if $N \geq 501$. On the other hand, J was taken as a constant value of 50, irrespective of the cumulative number of hits (Nair and Cai, 2010; ElBatanouny et al., 2014; Abdelrahman et al., 2015). The magnitudes of both $H(t)$ and S_r were calculated using **Equation 6.1 and Equation 6.2** for all tested samples at all test intervals.

6.4 Bond Behaviour of Corroded/Un-Corroded Samples

It is obvious from **Tables 6.1-6.2** that most samples (corroded/un-corroded) failed by bond splitting failure, which resulted in either splitting cracks along the bonded length at all four faces of the specimen or completely breaking the sample. For instance, the typical splitting failure of sample 20M30B0-1 is shown in **Figure 6.1**. However, fewer un-corroded samples exhibited bar yield before any damage at the steel-concrete interface had occurred. For the purpose of evaluating the AE activities in subsequent discussions, those samples with yielded bars were utilized as a benchmark to other tested samples that failed by splitting cracking. On the other hand, all corroded samples failed by bond splitting failure regardless of corrosion level. These results may be attributed to existence of corrosion cover cracks in all corroded samples before being tested under pull-out tests. **Table 6.4** demonstrates the values of corrosion exposure periods, average electric currents, corrosion cover crack widths, and compares the magnitudes of both actual and theoretical mass loss of steel in all corroded samples.

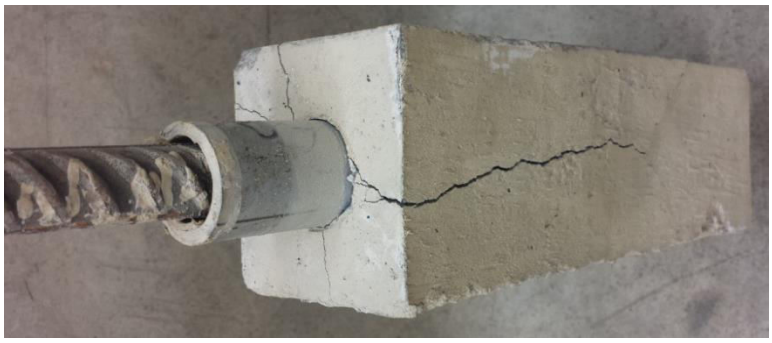

Figure 6.1 Typical bond splitting cracks at failure (example sample: 20M30B0-1)

Table 6.4 Results of accelerated corrosion process of all corroded samples

Sample designation	Corrosion exposure (day)	Average current (mA)	Actual mass loss of steel (%)	Crack width (mm)
20M20A1-1	3	15	0.99	0.11
20M20A1-2	3	17	1.13	0.12
20M20C1-1	3	58	0.97	0.31
20M20C1-2	3	65	1.08	0.34
20M20A2-1	5	19	1.88	0.24
20M20A2-2	5	21	2.07	0.34
20M20C2-1	5	71	1.97	0.58
20M20C2-2	5	69	1.91	0.45
20M20A3-1	6	22	2.92	0.31
20M20A3-2	6	24	2.98	0.32
20M20C3-1	6	89	2.93	0.75
20M20C3-2	6	91	2.89	0.82
20M20A4-1	8	23	3.95	1.04
20M20A4-2	8	22	3.86	0.85
20M20C4-1	8	93	4.02	2.21
20M20C4-2	8	90	3.79	1.85
20M20A5-1	10	24	4.96	1.45
20M20A5-2	10	23	4.69	1.16
20M20C5-1	9	105	5.03	3.45
20M20C5-2	9	98	4.88	2.55
20M30A1-1	6	8	0.96	0.08
20M30A1-2	6	7	0.93	0.06
20M30C1-1	6	29	0.97	0.14

20M30C1-2	6	31	1.03	0.21
20M30A2-1	8	13	2.01	0.28
20M30A2-2	8	11	1.96	0.24
20M30C2-1	8	46	1.95	0.48
20M30C2-2	8	43	1.91	0.43
20M30A3-1	10	14	2.88	0.32
20M30A3-2	10	16	2.93	0.45
20M30C3-1	10	55	3.02	0.58
20M30C3-2	10	53	2.9	0.52
20M30A4-1	12	16	3.59	0.49
20M30A4-2	12	18	3.86	0.65
20M30C4-1	12	64	3.99	1.08
20M30C4-2	12	60	3.78	0.82
20M30A5-1	13	18	4.87	0.89
20M30A5-2	13	20	4.89	1.11
20M30C5-1	15	60	4.99	1.12
20M30C5-2	15	70	5.05	1.21
20M40A1-1	15	5	0.69	0.05
20M40A1-2	15	7	0.87	0.09
20M40C1-1	15	15	0.75	0.24
20M40C1-2	15	18	0.93	0.38
20M40A2-1	16	8	1.89	0.21
20M40A2-2	16	9	1.94	0.23
20M40C2-1	16	19	1.76	0.28
20M40C2-2	16	23	1.93	0.35
20M40A3-1	17	10	2.95	0.31
20M40A3-2	17	11	2.87	0.34
20M40C3-1	17	31	2.92	0.48
20M40C3-2	17	33	3.01	0.52
20M40A4-1	18	12	3.76	0.44
20M40A4-2	18	15	3.99	0.42
20M40C4-1	18	43	4.05	0.91
20M40C4-2	18	39	3.89	0.87
20M40A5-1	19	13	4.87	0.96
20M40A5-2	19	16	5.06	1.08
20M40C5-1	19	47	4.86	1.13
20M40C5-2	19	51	4.93	1.14

6.5 Detection of Micro- and Macro-cracking in Corroded/Un-Corroded Samples Using AE Analysis

The analysis of the AE cumulative number of hits curves has previously been applied to evaluate the bond behaviour (Iwaki et al., 2003) and to detect the different stages of bond damage in reinforced concrete (Gallego et al., 2015). On the other hand, the use of signal strength parameters (CSS, *H (t)*, and S_r) has been found to be more sensitive in detecting various damage mechanisms in concrete structures—for example: (Nair and Cai, 2010; Rizzo et al., 2010; ElBatanouny et al., 2014; Abdelrahman et al., 2015; Vélez et al., 2015). To this end, the AE data (after being filtered) recorded throughout the pull-out test performed on sample 20M40A5-2 (as an example of all corroded samples) are graphed in **Figure 6.2**. The figure presents the variations in the values of AE cumulative number of hits, cumulative signal strength (CSS), historic index (*H (t)*), and severity (S_r) versus the elapsed time during the pull-out test on this specimen. **Figure 6.2a** indicates that the AE cumulative number of hits increased throughout the test until failure, with only one noticeable point of slope change at nearly 55 seconds after the beginning of the test. This increase in the AE cumulative number of hits can be related to the transfer of forces between steel and concrete by means of chemical adhesion and friction up to 55 seconds. After the slope change in this figure, the higher rise in the AE activity (cumulative number of hits) can be attributed to the onset of cover cracking, followed by de-bonding and bar slippage until bond splitting failure occurred in the sample.

In contrast, **Figure 6.2b** shows three locations of slope change in the CSS versus test time at approximately 51, 64, and 89 seconds. These locations can also be noticed in the values of *H (t)* and S_r, as seen from **Figure 6.2c** and **Figure 6.2d**, respectively. These figures

manifest sudden increases in the values of $H(t)$ and S_r at these three locations, which can be correlated to the successive stages of bond deterioration until failure. The first slope change in the CSS and S_r curves was associated with a clear increase in the value of $H(t)$ reaching a value of 1.52. This point is mostly related to the initiation of the micro-cracking at the concrete-steel interface, which was seen at a bond stress of 5.41 MPa. This bond stress represents 1.43 f_{ct} that is located in the range of 0.8–3.0 f_{ct}. It has been reported in the literature that this range of bond stress is normally accompanied by the presence of micro-cracking at the concrete-steel interface, which is followed by the initiation of bar slippage and macro-cracking of the concrete core (CEB-FIP, 2000; Gallego et al., 2015). The second slope change in the CSS and S_r curves was noted at the maximum detected value of $H(t)$, which is 2.52, as shown in **Figure 6.2c**. This point can be attributed to the onset of macro-cracking in the concrete core surrounding the bar, which preceded the occurrence of bar slippage. The detection of macro-cracking was also confirmed by visual inspection of the sample during the test and observing the cover cracking starting at about 72 seconds. The observation of the first visual crack was carefully noticed in all tested samples during the execution of the pull-out experiments. The identification of splitting cracking was further confirmed by reviewing the recorded values of the applied load through each test, which exhibited a small drop in the load versus time curve at the time of first visual crack detection.

The results of CSS and S_r continued to increase after the second slope change, corresponding to further cover cracking and bar slippage, until the results reached a third slope change at 89 seconds, as shown in **Figure 6.2b** and **Figure 6.2d**. This location showed the last significant increase in the value of $H(t)$ (1.83) just before the sample

failed by bond splitting mode. This value of *H (t)* was lower than that obtained at the detection of macro-cracking (2.52). This reduction in the magnitude of *H (t)* before failure can be attributed to the wave attenuation resulting from the existence of splitting cracks in the concrete cover, which would lead to lower signal strength and *H (t)*. Nonetheless, the results of AE cumulative number of hits, CSS, and S_r kept increasing until bond splitting failure occurred, as indicated by the horizontal part of the curves in **Figure 6.2**. It should be mentioned that all other tested samples (both corroded and un-corroded) followed a similar trends in the curves of the cumulative number of hits, CSS, *H (t)*, and S_r versus test time of sample 20M40A5-2 (but with different magnitudes of these AE parameters).

Similarly, **Figure 6.3** demonstrates the variations of the CSS and *H (t)* versus test time of two typical un-corroded samples (10M30B0-2 and 20M30B0-1). Sample 20M30B0-1 represents un-corroded samples that failed by typical bond splitting failure, and sample 10M30B0-2 represents bar yielded samples associated with no damage at the steel-concrete interface. It can be seen from **Figure 6.3a** that sample 10M30B0-2's CSS curve followed an almost linear increasing trend corresponding to the increase in loading until the bar yielded. Since no splitting failure occurred in sample 10M30B0-2, the increase in CSS of this sample may be attributed to the transfer of force between steel and concrete by means of chemical adhesion before the occurrence of micro-cracking. In contrast, **Figure 6.3c** indicates that the slope of the CSS curve witnessed two noticeable changes at nearly 220 s and 260 s from the beginning of the test. The first slope change in sample 20M30B-1 was detected at a stress value of 5.89 MPa (**Table 6.2**). This stress value corresponds to approximately 1.55 f_{ct}, which lies in the range of 0.8–3.0 f_{ct}.

After the first slope change of sample 20M30B0-1, the CSS curve continued to increase due to further micro-cracking and growth of macro-cracking. The second slope change of the CSS curve, with further increase of loading, can be related to the formation of macro-cracking (splitting cracks) as a result of the expected wedging action in small concrete cover thicknesses. The CSS curve also exhibited a slight rise after the second slope change until failure. This short rise in the CSS curve may be related to the increasing bar slippage values as well as widening of the splitting cracks until failure, which resulted in continuous AE activity. The initiation of micro- and macro-cracking stages was likewise distinguished by analyzing the *H (t)* curves in **Figure 6.3b**, **d**, which show that the values of *H (t)* fluctuated throughout the test period of sample 10M30B0-2 with no major variations (0.6–1.3). Conversely, as shown in **Figure 6.3d**, *H (t)* showed significant changes in the other sample (20M30B0-1). The first sudden increase in the values of *H (t)* for sample 20M30B-1 can be observed around 220 s (at the location of slope change in the CSS curve) with a value of 1.7. After this point, the values of *H (t)* continued to increase owing to the splitting cracks growth until reaching a maximum value of 6.05 at nearly 260 s. This maximum value also matched the point of the second slope change of the CSS curve (macro-cracking) a little before sample 20M30B0-1 underwent splitting failure. On the other hand, the variations in the curves of cumulative number of hits and S_r were found to be very similar to those observed in the CSS; therefore, only the CSS and *H (t)* curves were included in **Figure 6.3**.

On this basis, the stage of micro-cracking in all corroded/un-corroded samples (except those ones with bar yield) was identified and the corresponding magnitudes of load and stress are reported in **Tables 6.1-6.2**. In addition, **Tables 6.5-6.6** show the AE parameter

values—i.e., cumulative number of hits, CSS, *H (t)*, and S_r—at both the micro- and macro-cracking stages for all corroded/un-corroded samples. The tables also include the amplitude values of the signals detected at these stages of bond damage. It can also be noticed that the variations in bar diameter, concrete cover thickness, corrosion level, and embedded length yielded significant changes in the results of bond behaviour among the tested samples, as will be explained in the following sections. It should be noted that, the identification of bond damage (micro- and macro-cracking) using the variations of CSS, *H (t)*, and S_r presented in this study is based on the range of tested variables in this investigation. Further studies are needed to examine the effects of other factors exist in real concrete structures (such as varying the bar confinement, specimen size, and ambient conditions) on AE parameters in order to complement/confirm these results.

The AE waveform parameters detected prior to micro- and macro-cracking were characterized by relatively low amplitude signals (average of 50 dB). Whilst, higher amplitude signals (average of 75 dB) were associated with the detection of both micro- and macro-cracking, with no clear differences observed between the amplitudes of these signals (**Tables 6.5-6.6**). Thus, the analysis of the amplitude values of the collected AE waves may be used for detecting the damage, but is not a feasible method for identifying different levels of bond damage. This was due to the non-significant changes of the amplitudes of the signals detected at both micro- and macro-cracking for all tested samples. It should be mentioned that all other AE signal parameters (duration, energy, rise time, average frequency, counts, and peak frequency) also showed non-significant variations between tested samples acquired both at micro-cracking initiation and macro-cracking. Therefore, only the cumulative number of hits, CSS, *H (t)*, and S_r parameters

(**Tables 6.5-6.6**) were considered in evaluating the effects of bar diameter, bonded length, corrosion level, and cover thickness on the bond behaviour, as will be explained in the following sections.

(a)

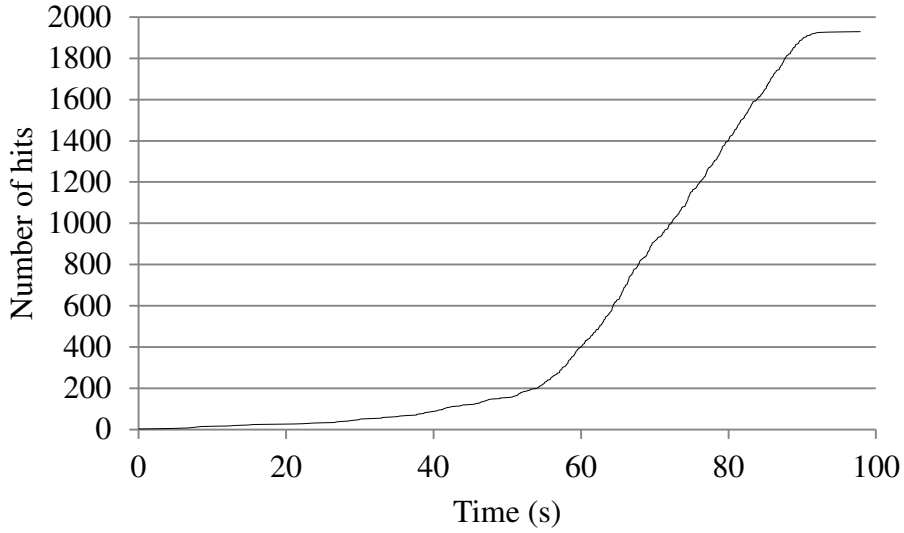

(b)

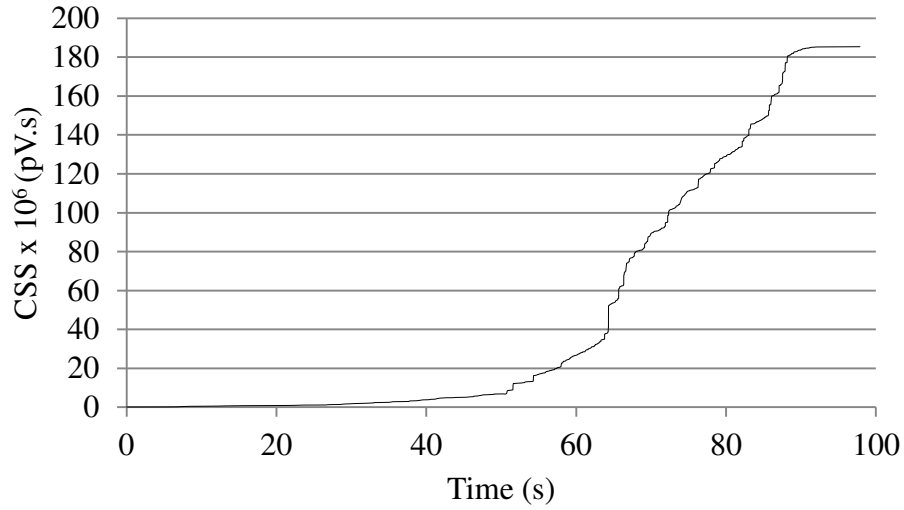

(c)

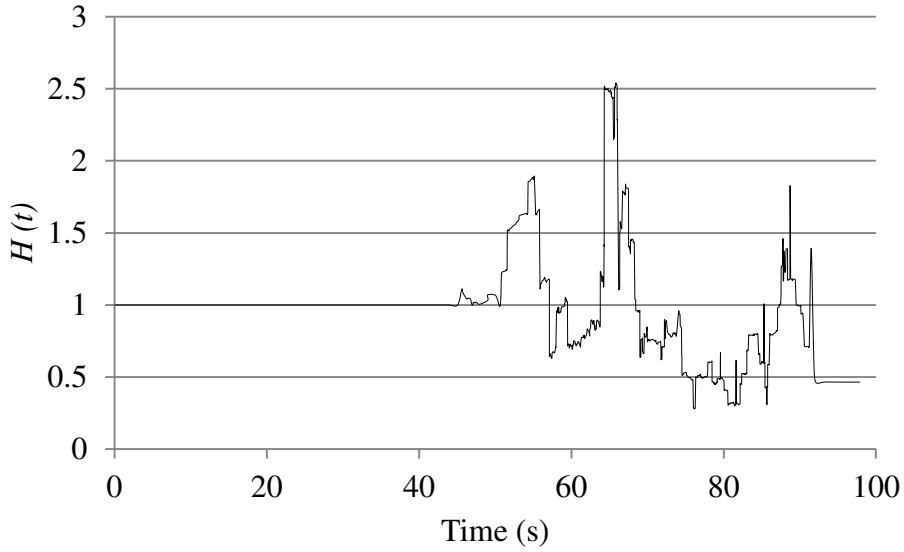

(d)

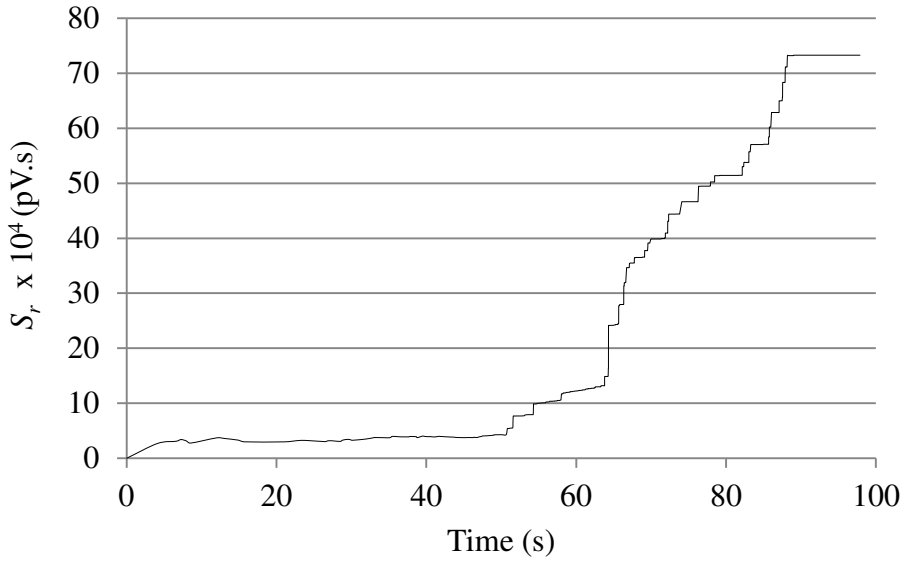

Figure 6.2 Variations of AE parameters versus test time for typical corroded sample (20M40A5-2): (a) cumulative number of hits, (b) CSS, (c) *H (t)*, and (d) S_r

(a)

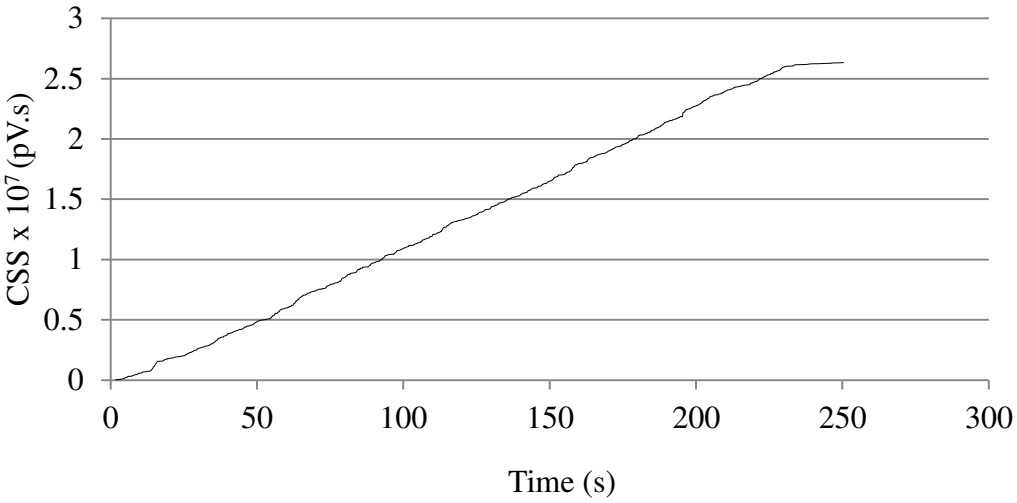
3
2.5
2
1.5
1
0.5
0
CSS x 10^7 (pV.s)
0
50
100
150
200
250
300
Time (s)

(b)

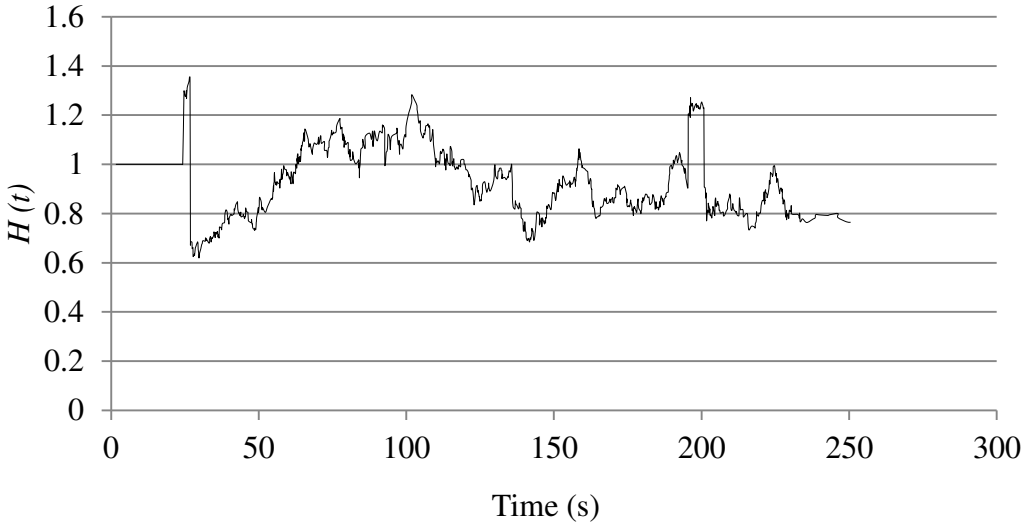
1.6
1.4
1.2
1
0.8
0.6
0.4
0.2
0
H (t)
0
50
100
150
200
250
300
Time (s)

(c)

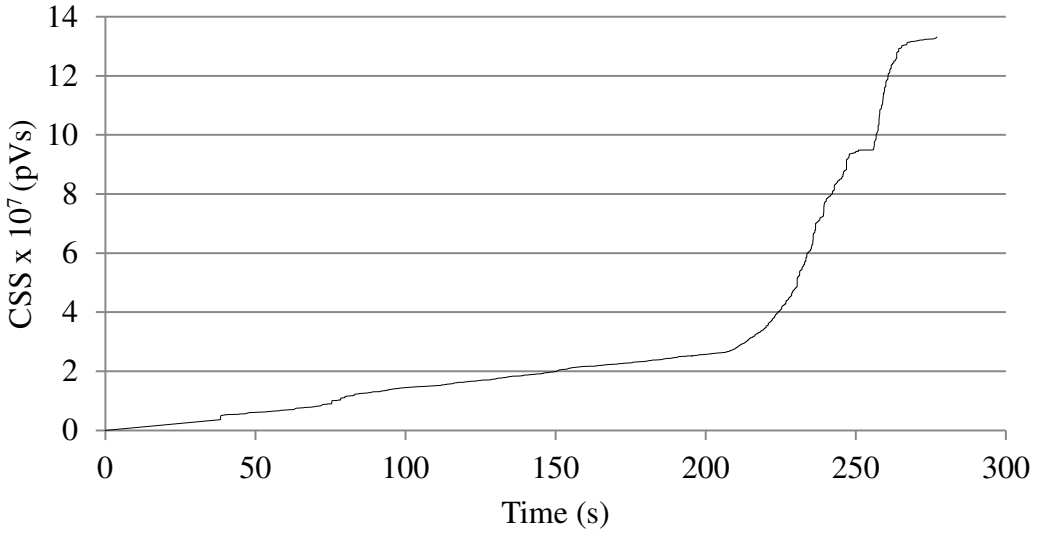

(d)

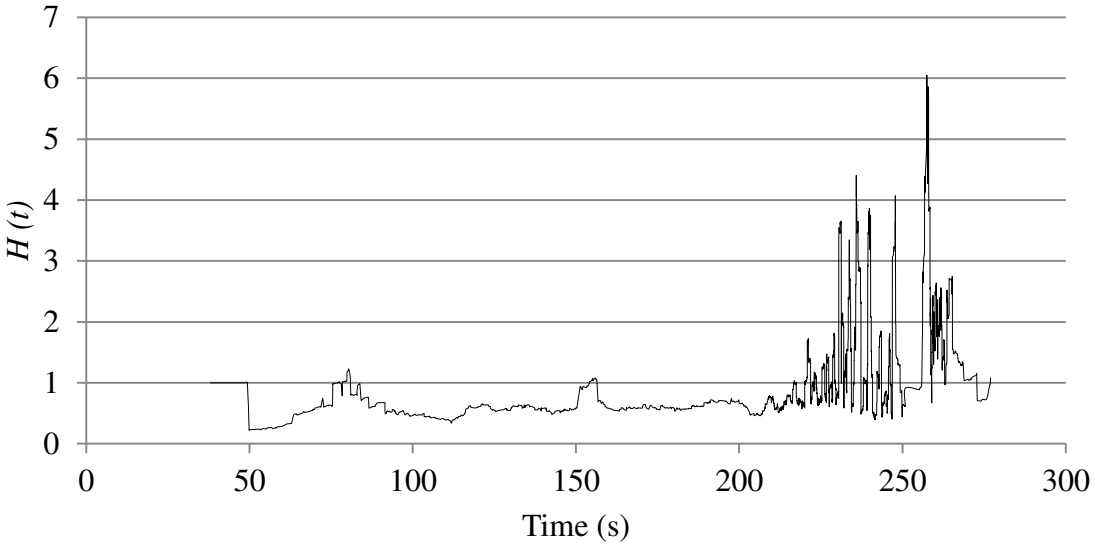

Figure 6.3 CSS and *H (t)* curves for typical un-corroded samples (10M30B0-2 and 20M30B0-1): (a) CSS versus test time for sample 10M30B0-2, (b) *H (t)* versus test time for sample 10M30B0-2, (c) CSS versus test time for sample 20M30B0-1, and (d) *H (t)* versus test time for sample 20M30B0-1

Table 6.5 Different AE parameters at micro- and macro-cracking stages of all corroded samples

Sample designation	Cumulative number of hits		CSS (pV.s) x 10^6		Amplitude (dB)		*H (t)*		S_r (pV.s) x 10^4	
	Micro-cracking	Macro-cracking	Micro-cracking	Macro-cracking	Micro-cracking	Macro-cracking	Micro-cracking	Macro-cracking	Micro-cracking	Macro-cracking
20M20A1-1	509	763	13.15	81.38	71	69	1.44	2.83	6.49	14.12
20M20A1-2	411	905	11.51	69.90	67	71	1.53	2.55	5.95	11.98
20M20C1-1	1556	2364	81.04	121.73	70	68	1.55	5.06	15.33	84.54
20M20C1-2	1731	2358	83.65	128.81	68	71	1.48	5.07	14.53	87.25
20M20A2-1	401	735	11.81	71.49	66	69	1.40	2.40	4.64	11.55
20M20A2-2	365	841	8.92	76.30	70	72	1.42	2.26	5.11	12.80
20M20C2-1	1602	2059	83.20	116.09	74	75	1.55	4.04	15.06	88.04
20M20C2-2	1321	1736	80.45	123.05	76	73	1.54	3.69	13.33	84.30
20M20A3-1	399	726	9.52	63.58	70	70	1.45	2.21	4.46	10.29
20M20A3-2	331	590	9.09	60.45	76	73	1.38	2.05	4.10	11.31
20M20C3-1	1581	1884	81.18	111.32	73	71	1.40	3.44	12.07	84.68
20M20C3-2	1370	1755	78.79	97.81	71	74	1.58	3.28	12.03	85.58
20M20A4-1	308	595	8.00	55.27	68	70	1.38	2.01	4.60	10.12
20M20A4-2	291	1603	9.56	52.74	67	76	1.45	2.02	4.84	10.06
20M20C4-1	1267	1827	69.27	103.45	71	74	1.40	2.60	8.89	81.90
20M20C4-2	1261	1649	78.40	97.04	67	71	1.44	3.01	10.61	82.38
20M20A5-1	302	557	7.42	47.67	72	69	1.51	1.91	5.02	10.20
20M20A5-2	264	538	6.78	43.84	68	71	1.31	1.81	3.53	9.30
20M20C5-1	1101	1745	68.64	88.01	71	72	1.37	2.11	7.04	75.80
20M20C5-2	1151	1482	68.80	91.36	77	73	1.60	1.95	9.51	80.60
20M30A1-1	460	770	14.02	95.67	66	70	1.44	2.79	9.06	29.03
20M30A1-2	473	695	12.06	84.37	77	66	1.38	3.05	9.13	37.99
20M30C1-1	2015	2691	133.69	190.17	69	68	1.53	4.86	16.87	91.97
20M30C1-2	2307	2436	128.36	171.15	73	71	1.55	4.67	14.89	80.99
20M30A2-1	426	688	14.02	90.19	81	71	1.33	2.72	8.99	34.78
20M30A2-2	441	773	10.36	79.87	66	69	1.29	2.63	8.63	30.69
20M30C2-1	1839	2203	143.28	178.69	67	71	1.60	3.97	12.79	80.01
20M30C2-2	2005	2421	116.30	154.13	69	70	1.48	4.02	15.08	89.45
20M30A3-1	401	680	10.98	77.15	74	72	1.47	2.34	7.45	25.25
20M30A3-2	423	641	11.08	80.39	73	80	1.36	2.49	8.16	36.07
20M30C3-1	1907	2336	119.36	145.23	71	67	1.51	3.55	14.09	77.09
20M30C3-2	1856	2103	106.97	139.66	69	68	1.46	3.43	13.01	73.97

20M30A4-1	351	590	9.69	70.36	66	70	1.60	2.46	7.22	31.02
20M30A4-2	336	613	8.77	65.37	80	68	1.39	2.22	6.88	23.12
20M30C4-1	1697	1987	109.04	137.14	66	73	1.61	3.04	12.36	69.19
20M30C4-2	1783	2107	90.58	110.28	68	72	1.44	2.89	10.99	60.07
20M30A5-1	310	567	7.82	52.19	75	76	1.42	2.39	7.15	29.20
20M30A5-2	319	591	8.19	60.37	69	71	1.52	2.06	6.13	21.09
20M30C5-1	1306	1882	90.16	112.71	75	76	1.42	2.32	10.69	53.40
20M30C5-2	1508	2203	85.34	96.87	70	67	1.37	2.67	11.28	57.09
20M40A1-1	669	908	12.77	78.09	70	68	1.37	2.99	7.66	28.36
20M40A1-2	587	963	15.19	86.02	71	72	1.58	3.19	12.92	36.19
20M40C1-1	2411	3652	161.23	199.63	67	70	1.46	5.97	18.66	96.24
20M40C1-2	2569	4120	148.69	215.15	73	69	1.60	5.23	17.69	88.19
20M40A2-1	539	798	12.02	74.87	69	69	1.42	3.05	10.69	32.21
20M40A2-2	510	888	12.66	76.98	70	72	1.48	2.83	9.29	31.39
20M40C2-1	2109	3098	119.39	177.98	80	70	1.39	5.01	18.04	89.63
20M40C2-2	2262	3436	143.69	193.05	69	67	1.19	4.57	16.40	82.90
20M40A3-1	493	819	10.38	68.12	67	80	1.51	3.02	10.08	32.90
20M40A3-2	462	769	11.01	69.09	67	67	1.43	2.95	8.88	29.80
20M40C3-1	2039	2769	106.12	129.69	69	66	1.37	3.87	14.12	71.39
20M40C3-2	1966	2912	122.09	166.37	77	69	1.46	4.02	16.05	80.63
20M40A4-1	402	802	9.88	66.19	76	74	1.28	2.49	9.55	30.13
20M40A4-2	389	713	8.66	60.28	73	80	1.39	2.88	8.12	26.12
20M40C4-1	1903	2697	103.78	147.98	75	68	1.71	3.69	14.97	73.88
20M40C4-2	1706	2467	97.01	130.69	70	72	1.58	3.25	13.67	66.12
20M40A5-1	427	654	6.05	64.01	68	70	1.39	2.64	8.87	29.64
20M40A5-2	174	598	11.99	52.07	69	74	1.52	2.52	7.64	24.15
20M40C5-1	1832	2558	94.02	122.36	74	79	1.46	2.67	11.29	64.30
20M40C5-2	1603	2109	86.69	100.15	67	69	1.42	2.82	12.69	69.15

Table 6.6 Different AE parameters at micro- and macro-cracking stages of all un-corroded samples

Sample designation	Cumulative number of hits		CSS (pV.s) x 10^6		Amplitude (dB)		*H (t)*		S_r (pV.s) x 10^4	
	Micro-cracking	Macro-cracking	Micro-cracking	Macro-cracking	Micro-cracking	Macro-cracking	Micro-cracking	Macro-cracking	Micro-cracking	Macro-cracking
10M20A0-1	187	278	6.14	8.89	69	73	1.87	2.46	5.86	10.23
10M20A0-2	342	775	11.47	17.18	72	73	1.87	2.98	6.53	14.54

10M20B0-1	669	816	16.33	23.64	78	76	1.83	3.69	7.68	24.37
10M20B0-2	742	1104	17.04	19.59	72	86	1.77	4.19	11.95	30.71
10M20C0-1	858	1341	20.30	25.14	72	78	1.98	3.86	14.50	31.37
10M20C0-2	985	1551	19.57	26.36	69	80	1.94	4.44	16.00	31.06
20M20A0-1	521	764	11.70	84.17	70	76	1.97	2.83	7.84	17.57
20M20A0-2	810	945	14.23	91.17	77	75	2.05	2.89	6.18	12.92
20M20B0-1	1196	2780	59.26	139.49	70	83	2.01	3.81	11.15	20.01
20M20B0-2	1556	2387	72.38	122.98	73	79	2.17	3.97	10.89	30.00
20M20C0-1	2261	3599	92.04	145.72	71	80	2.23	7.03	17.16	77.90
20M20C0-2	1606	2525	86.56	130.68	70	80	1.91	5.51	15.09	101.17
35M20A0-1	887	1180	16.32	54.79	69	78	1.93	2.79	8.38	55.12
35M20A0-2	840	1184	12.88	39.74	71	79	1.91	2.78	8.13	35.65
35M20B0-1	1297	1729	57.48	85.07	72	72	2.21	3.95	12.09	73.47
35M20B0-2	1553	1889	72.42	89.91	80	71	2.07	5.13	11.22	89.94
35M20C0-1	2415	3538	104.77	140.67	74	78	2.02	6.18	18.91	98.73
35M20C0-2	2282	4059	125.26	140.75	74	72	1.74	6.45	13.26	110.60
10M30A0-1	294	685	12.12	19.77	73	82	1.85	2.27	5.89	14.19
10M30A0-2	353	558	12.30	16.17	72	74	2.01	3.28	7.39	17.54
10M30B0-1	NA	1908	NA	56.09	NA	49	NA	0.87	NA	20.81
10M30B0-2	NA	816	NA	25.03	NA	48	NA	0.81	NA	26.90
10M30C0-1	NA	2401	NA	83.14	NA	50	NA	0.84	NA	35.13
10M30C0-2	NA	2717	NA	86.12	NA	51	NA	0.84	NA	44.10
20M30A0-1	346	762	11.98	42.88	70	78	2.12	3.57	11.36	48.15
20M30A0-2	494	872	15.97	30.28	70	70	1.75	3.01	7.73	21.89
20M30B0-1	1062	2111	32.51	94.08	73	75	1.60	4.19	13.78	85.14
20M30B0-2	1421	1568	25.56	36.99	72	79	2.22	4.58	12.95	28.59
20M30C0-1	3880	5039	174.35	243.20	80	84	2.11	5.93	20.09	138.29
20M30C0-2	1471	2453	143.44	102.09	72	82	1.62	5.35	17.69	84.44
35M30A0-1	587	1033	17.28	39.38	71	81	1.88	3.14	10.21	30.85
35M30A0-2	585	1201	19.27	43.66	69	79	1.78	3.81	13.72	32.24
35M30B0-1	1002	1884	65.37	131.53	77	84	2.08	4.45	18.45	144.11
35M30B0-2	1967	2780	69.05	114.59	73	83	1.99	4.49	15.43	82.82
35M30C0-1	2727	3532	197.22	219.45	78	81	2.03	6.34	17.89	165.83
35M30C0-2	2671	3461	108.25	126.40	81	76	2.06	6.16	20.15	102.60
10M40A0-1	NA	779	NA	17.70	NA	48	NA	0.87	NA	16.65
10M40A0-2	352	788	13.78	18.99	72	73	1.92	3.17	8.28	16.24
10M40B0-1	NA	1589	NA	46.28	NA	48	NA	0.84	NA	26.97
10M40B0-2	NA	1766	NA	63.33	NA	49	NA	0.75	NA	36.64
10M40C0-1	NA	2597	NA	90.69	NA	49	NA	1.10	NA	49.05
10M40C0-2	NA	2273	NA	80.84	NA	52	NA	0.91	NA	43.66

20M40A0-1	628	992	22.16	33.27	71	73	1.99	3.11	16.83	26.41
20M40A0-2	707	917	9.25	54.39	75	83	1.78	3.57	6.74	15.08
20M40B0-1	1578	1761	44.74	54.00	71	77	1.86	4.96	17.18	32.48
20M40B0-2	1728	2185	16.64	31.25	74	72	2.07	3.94	16.22	38.45
20M40C0-1	2713	3477	145.54	207.23	72	83	2.20	9.40	19.86	104.58
20M40C0-2	2497	4732	188.38	268.46	72	82	2.02	7.07	18.54	100.65
35M40A0-1	714	1107	16.79	54.59	72	76	1.80	4.64	12.26	68.08
35M40A0-2	817	1082	18.93	54.21	72	78	1.93	3.46	17.46	56.53
35M40B0-1	1823	2662	38.14	62.61	76	73	2.07	5.17	22.04	78.19
35M40B0-2	2135	3284	29.59	69.31	77	79	2.32	5.78	12.78	54.34
35M40C0-1	2968	3812	192.26	256.48	73	77	2.22	5.68	25.02	83.82
35M40C0-2	3145	4033	183.72	284.48	75	84	1.83	9.60	19.00	164.02

6.6 Effect of Bar Diameter on Different AE Parameters

It can be noted from **Table 6.2** that larger bar diameters resulted in lower bond strength in all un-corroded samples, as expected. **Table 6.6** indicates that increasing the bar diameter warranted higher average values of cumulative hits, CSS, and S_r, both at micro- and macro-cracking, for all cover thicknesses and bonded lengths. For example, the change of bar diameters from 10 to 20 mm in specimens 10M20A0-1 and 20M20A0-1 (with constant cover thickness and bonded length) resulted in nearly a 178%, 91%, and 34% increase in cumulative hits, CSS, and S_r at micro-cracking, respectively, and roughly a 175%, 847%, and 72% increase in cumulative number of hits, CSS, and S_r at macro-cracking, respectively. This increase may be correlated to the larger surface area of the steel-concrete interface, which resulted in higher friction and rib bearing resistance, thus emitting more AE activities. Nonetheless, the change in bar diameter showed no significant influence on the magnitude of $H(t)$ at the micro-cracking stage. Furthermore, increasing the bar diameter at macro-cracking seemed to slightly increase the average value of $H(t)$. For example, in specimens 10M20A0-1 and 20M20A0-1, which had equal

cover thickness and embedded length, this increase was approximately 15% as a consequence of increasing the bar diameter from 10 to 20 mm. It should be mentioned that the AE parameters considered (cumulative number of hits, CSS, *H (t)*, and S_r) showed more correlation to the contact area of the steel-concrete interface than the bond strength. This correlation was also noticed when the embedded length of the bar increased, in which the AE activity increased while the bond strength decreased (Section 6.9). In the meantime, no evident differences in the waveform parameters (amplitude, duration, energy, rise time, average frequency, counts, and peak frequency) were observed in all tested samples with different bar diameters at all stages of damage.

6.7 Effect of Corrosion Level on Different AE Parameters

Prior to the pull-out testing, 60 samples were previously exposed to different levels of corrosion ranging between 1 to 5% of steel mass loss. The increase in corrosion level from 0 to 5% resulted in an average reduction in the bond strength of 52%, 40%, and 38% in samples with cover thicknesses of 20 mm, 30 mm, and 40 mm, respectively (**Tables 6.1-6.2**). This decrease in bond strength was also noticed by increasing the corrosion level, regardless of bar bonded length or cover thickness. The AE data corresponding to two stages of bond loss (micro- and macro-cracking) in the tested samples are presented in **Tables 6.5-6.6** and were used as a basis for comparing samples exposed to different degrees of corrosion. The increase in corrosion level resulted in an overall decrease in the values of AE cumulative number of hits, CSS, and S_r, at both micro- and macro-cracking stages. On the other hand, by increasing the percentage of steel mass loss, the results of *H (t)* decreased at the macro-cracking stage only. For instance, by comparing samples

20M20A0-1 with 20M20A5-1 (same bonded length and cover thickness), it was found that increasing corrosion from 0 to 5% yielded lower cumulative number of hits (by 42%), CSS (by 37%), and S_r (by 36%) at the micro-cracking stage. This general reduction in AE parameters at micro-cracking can be attributed to the lower contribution of chemical adhesion and friction between concrete and steel resulting from steel corrosion. The corrosion products that accumulate around the bar surface can significantly reduce the rebar-concrete adhesion, especially at high degrees of corrosion. In addition, increasing the accumulation of the corrosion product caused expansion of the bar volume and cover cracking, which reduced the rebar-concrete confinement and friction. This can be seen from **Table 6.4**, which denotes higher crack widths when the corrosion level increases from 1 to 5%.

The decrease in AE parameters because of reinforcement corrosion was also obtained by comparing the same samples (20M20A0-1 versus 20M20A5-1) at the macro-cracking stage. For example, the increase in mass loss from 0 to 5% caused a general reduction in AE parameters: cumulative number of hits (by 27%), CSS (by 43%), *H (t)* (by 33%), and S_r (by 42%), at macro-cracking stage (**Tables 6.5-6.6**). This reduced AE activity can be related to the lower contribution of rib bearing in resisting additional forces due to its minimized size following corrosion propagation. This reduction can also be correlated to the presence of corrosion cover cracks, which may lead to less signal strength as a result of any possible signal attenuation. The latter can be justified by the slight decrease (6%) in the average amplitude of the signal detected in non-corroded samples when compared to the average amplitude of all corroded samples, as shown in **Tables 6.5-6.6**. It is worth

noting that these minimized AE parameters, owing to higher corrosion levels, were noted in all other tested samples with varied bonded length and cover thickness.

6.8 Effect of Cover Thickness on Different AE Parameters

The changes in the bar confinement (in terms of varied concrete cover thickness) yielded significant effects on both bond strength and AE parameters both in corroded and un-corroded samples (**Tables 6.1-6.2 and Tables 6.5-6.6**). It can be seen from the tables that increasing the cover thickness (20 to 30 mm and 30 to 40 mm) led to both higher average bond strength and higher AE parameters at the micro-cracking stage (cumulative number of hits, CSS, and S_r). For example, the increase of cover thickness in samples 20M20A5-2 and 20M30A5-2 (with the same bonded length and steel mass loss) resulted in higher AE cumulative number of hits (by 21%), CSS (by 21%), and S_r (by 74%) at the micro-cracking stage. This increase in AE parameters at micro-cracking can be correlated to the higher loads resisted by those samples with larger cover thickness prior to the micro-cracking initiation (leading to higher friction and AE activity). On the contrary, no clear variations in the magnitudes of *H (t)* can be seen at the micro-cracking stage of all tested samples regardless of cover thickness (**Tables 6.5-6.6**).

On the other hand, it can be noticed that increasing the cover thickness from 20 to 30 mm and from 30 to 40 mm (**Tables 6.5-6.6**) increased overall the average values of AE cumulative number of hits, CSS, *H (t)*, and S_r at the macro-cracking stage. For instance, the change in cover thickness from 20 to 30 mm in samples 20M20A5-2 and 20M30A5-2 increased the AE cumulative number of hits (by 10%), CSS (by 38%), *H (t)* (by 14%), and S_r (by 127%). This higher AE activity can be related to the enhanced bond capacity of

the sample by using larger cover thicknesses. This increased AE activity can also be attributed to the lower widths of corrosion cracks obtained in samples with larger cover thickness and vice versa, as shown in **Table 6.4**. Another reason for increased AE parameters with higher concrete cover thickness is the growth of splitting cracks, which increased owing to larger cover thicknesses. These findings also highlight the correlation of AE parameters (cumulative number of hits, CSS, *H (t)*, and S_r) to the size of splitting cracks associated with bond degradation in all corroded and un-corroded specimens. It should be mentioned that higher values of cover thickness were expected to contribute to the wave attenuation, resulting in AE signals with lower values of signal strength. However, this phenomenon was not pronounced in the results due to the use of relatively small values of cover thickness.

6.9 Effect of Embedded Length on Different AE Parameters

As previously noted, three embedded lengths were used to investigate the effect of embedded length on the cumulative number of hits, CSS, *H (t)*, and S_r at all stages of bond deterioration. The increase in the bonded length from 50 to 200 mm resulted in lower values of bond strength for all tested samples regardless of bar diameter, cover thickness, or steel mass loss (**Tables 6.1-6.2**). **Tables 6.5-6.6** indicate that increasing the embedded length from 50 to 100 mm and from 100 to 200 mm resulted in a higher average cumulative number of hits, CSS, and S_r in all tested samples (corroded and un-corroded) at the micro-cracking stage. For example, by comparing two samples with the same bar diameter and cover thickness (10M20A0-1 versus 10M20B0-1), it was found that nearly 257% higher cumulative number of hits, 166% increase in CSS, and 57%

higher S_r were obtained after increasing embedded length from 50 to 100 mm. This increase in the cumulative number of hits, CSS, and S_r was also seen at all values of bar diameters, corrosion level, and cover thicknesses. This high AE activity can be attributed to the higher number of ribs included in the bonded length, which led to additional adhesion, friction, and rib-bearing forces. However, longer embedded lengths were found to have a non-significant effect on the values of *H (t)* corresponding to micro-cracking inception with an average value of *H (t)* of 1.97 in un-corroded samples. It is worth noting that the values of *H (t)* and S_r are not similar to those of cumulative number of hits and CSS, which are based on cumulative values rather than damage indices. This result indicates the effectiveness of *H (t)* and S_r to represent the damage extent at the steel-to-concrete bond interface, regardless of the value of the embedded length.

At the macro-cracking level, the results of all AE parameters increased by using longer bonded lengths in all tested specimens regardless of bar diameter, concrete cover, or corrosion degree (**Tables 6.5-6.6**). For instance, the values of cumulative number of hits, CSS, *H (t)*, and S_r increased by about 194%, 166%, 50%, and 138%, respectively, after the bonded length was increased from 50 to 100 mm in samples 10M20A0-1 and 10M20B0-1 (which had identical bar diameter and cover thickness). This overall rise in the magnitude of cumulative number of hits, CSS, *H (t)*, and S_r at macro-cracking can be related to the fact that longer embedded length samples exhibited longer splitting cracks (i.e., larger crack sizes). This trend was also confirmed in all tested samples, including corroded and un-corroded, irrespective of the value of bar diameter, cover thickness, or percentage of steel mass loss (**Tables 6.5-6.6**). Owing to the cumulative nature of the cumulative number of hits and CSS, it may be more accurate to use *H (t)* and S_r to

identify the variable crack sizes. The results of visual inspection of samples with variable bonded length indicated that longer bonded length samples exhibited longer splitting cracks, which propagated almost through the same length as the bonded length. These results highlight the effectiveness of intensity analysis parameters in estimating the size of splitting cracks resulting from bond failure.

6.10 Damage Quantification of Corroded/Un-Corroded Samples Using AE Intensity Analysis

The preceding sections mentioned that the analysis of AE parameters enabled the detection of two early stages of bond deterioration before failure of all samples (micro- and macro-cracking stages). It was also noted that these AE parameters were well correlated with the bar diameter, bonded length, cover thickness, and degree of corrosion in all tested samples. More specifically, the results of intensity analysis on AE signal strength yielded two parameters (*H (t)* and S_r) that showed high sensitivity to the extent of bond damage in all specimens. These parameters have been exploited in a number of previous studies to represent different damage mechanisms in concrete structures (for example: Nair and Cai, 2010; Abdelrahman et al., 2015; ElBatanouny et al., 2014). The values of *H (t)* and S_r corresponding to the detection of both micro- and macro-cracking for all corroded and un-corroded specimens are plotted in **Figures 6.4-6.5**, respectively, to develop intensity classification charts.

These charts can be utilized to distinguish between the micro- and macro-cracking stages of bond damage of corroded and un-corroded reinforcing bars. For instance, if the values of *H (t)* and S_r were located in the ranges of 1.19-1.71 and 3.53-18.66 x 10^4 pV.s,

respectively, then micro-cracking is anticipated at the concrete-steel interface. On the other hand, the macro-cracking stage is expected, if the values of *H (t)* and S_r were located in the ranges of 1.81-5.97 and 9.30-96.24 x 104 pV.s, respectively, for corroded specimens (**Figure 6.4**). Similarly, if the values of *H (t)* and S_r range between 1.51-2.49 and 5.15-29.89 x 10^4 pV.s, respectively, micro-cracking of concrete is expected to be present at the steel-concrete interface. Beyond *H (t)* and S_r readings of 2.49 and 29.89x 10^4 pV.s, respectively, macro-cracking in the surrounding concrete core around the steel bar is anticipated in un-corroded samples (**Figure 6.5**). It can be noticed from the charts (**Figures 6.4-6.5**) that the magnitudes of *H (t)* and S_r at the stage of macro-cracking showed a wide range of increase following the micro-cracking region. These wide ranges were attributed to the large differences in the sizes of splitting cracks and the significant impact of using variable bar diameters, bonded lengths, cover thicknesses, and corrosion levels on the AE intensity analysis parameters. However, this chart may be especially beneficial for early detection of bond deterioration between concrete and steel at the micro-cracking stage. At this stage, no visible signs of cracking or bar slippage were detected in all tested samples. It is worth noting that the ranges presented in this chart are only based on the range of bar diameters (10-35 mm), bonded lengths (50-200 mm), cover thicknesses (20-40 mm), and percentages of steel mass loss (1-5%) obtained from the 114 samples tested herein.

Moreover, the evaluation of *H (t)* results enabled the differentiation between un-corroded samples failed by bar yield from those subjected to bond splitting failure. For example, an average *H (t)* value of 0.87 was obtained from the samples that exhibited bar yield with no damage in the bond integrity (**Table 6.6**). This average value corresponds to the

maximum load recorded right before the bar yield (**Table 6.2**). These observations illustrate the accuracy of the *H (t)* in both detecting the onset of micro-cracking and representing mode of failure among the un-corroded tested specimens. It should also be noted that further verification of the results in this chart are needed to generalize those parameters based on testing full-scale reinforced concrete elements (**Chapter 7**).

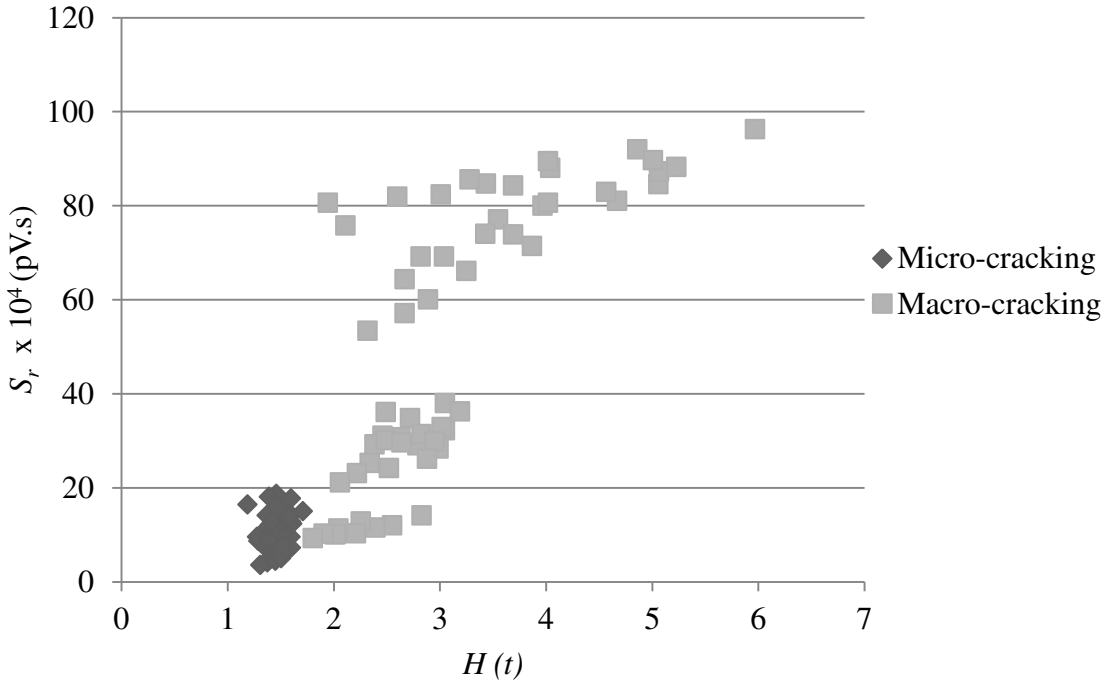

Figure 6.4 Classification chart for bond damage stages of corroded samples

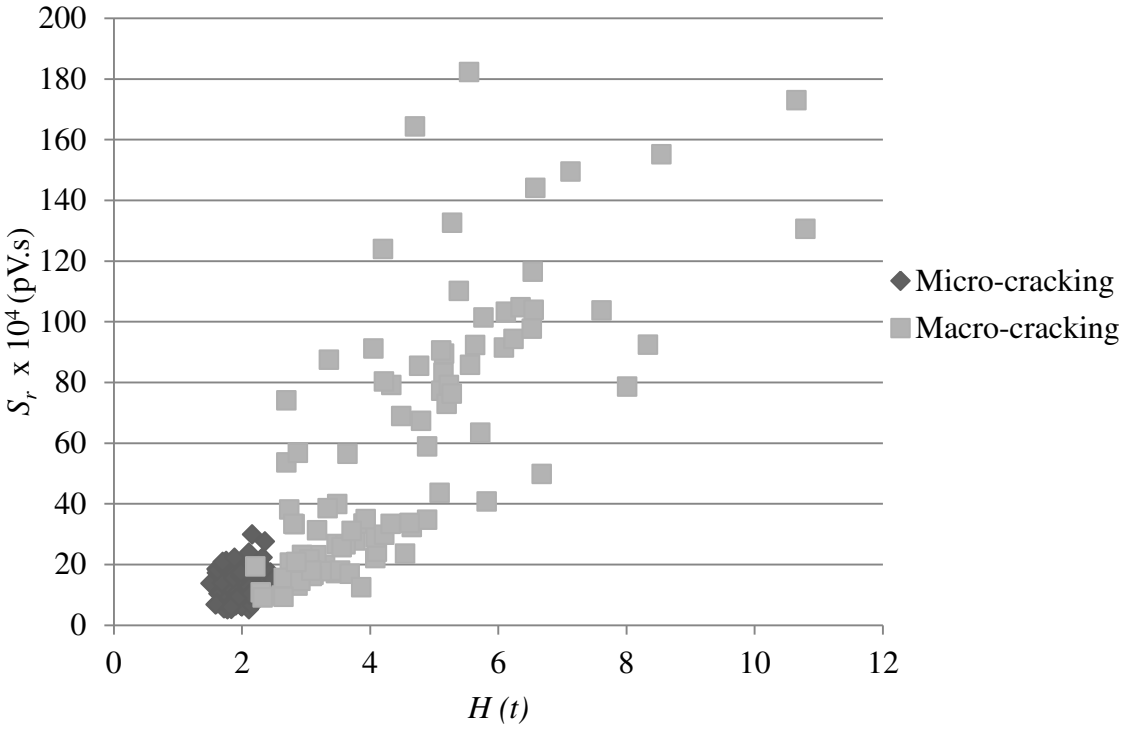

Figure 6.5 Classification chart for bond damage stages of un-corroded samples

Similar to the classification charts presented in **Figures 6.4-6.5**, other classification charts were also developed using the results of *H (t)* and S_r and their corresponding magnitude of free end slip (**Tables 6.1-6.2**) to identify the range of bar slip of corroded and un-corroded bars, as shown in **Figures 6.6-6.7**, respectively. These charts can classify the value of the bar slippage into four successive ranges: 0 to 0.25 mm, 0.25 to 0.5 mm, 0.5 to 0.75 mm, and 0.75 to 1.2 mm according to the values of *H (t)* and S_r obtained using AE monitoring of existing concrete structures. It can be seen from the chart that both values of *H (t)* and S_r were in a good correlation with the amount of bar slip in all tested samples. It is clear from the figure that lower values of bar slippage were associated with lower magnitudes of *H (t)* and S_r. This decrease in *H (t)* and S_r with lower slip values may be related to the reduction of bond strength in these samples, which was accompanied by

lower bar slippage (**Tables 6.1-6.2**). It should be mentioned that the variations in the values of *H (t)* and S_r within the same range of bar slip in **Figures 6.6-6.7** can be attributed to the inclusion of samples with different bar diameters, bonded length, cover thickness, and percentage of steel mass loss in the same range. In addition, the values of *H (t)* and S_r in this chart were calculated based on the average of the AE signals recorded using two sensors in each tested sample.

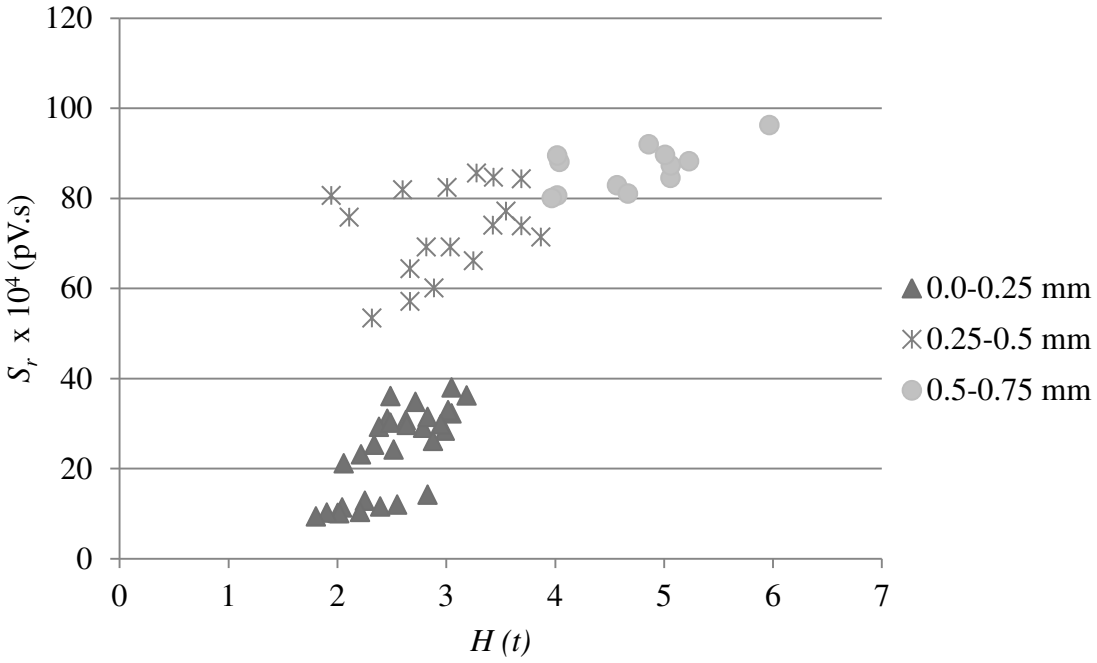

Figure 6.6 Free end slip intensity quantification chart for corroded samples

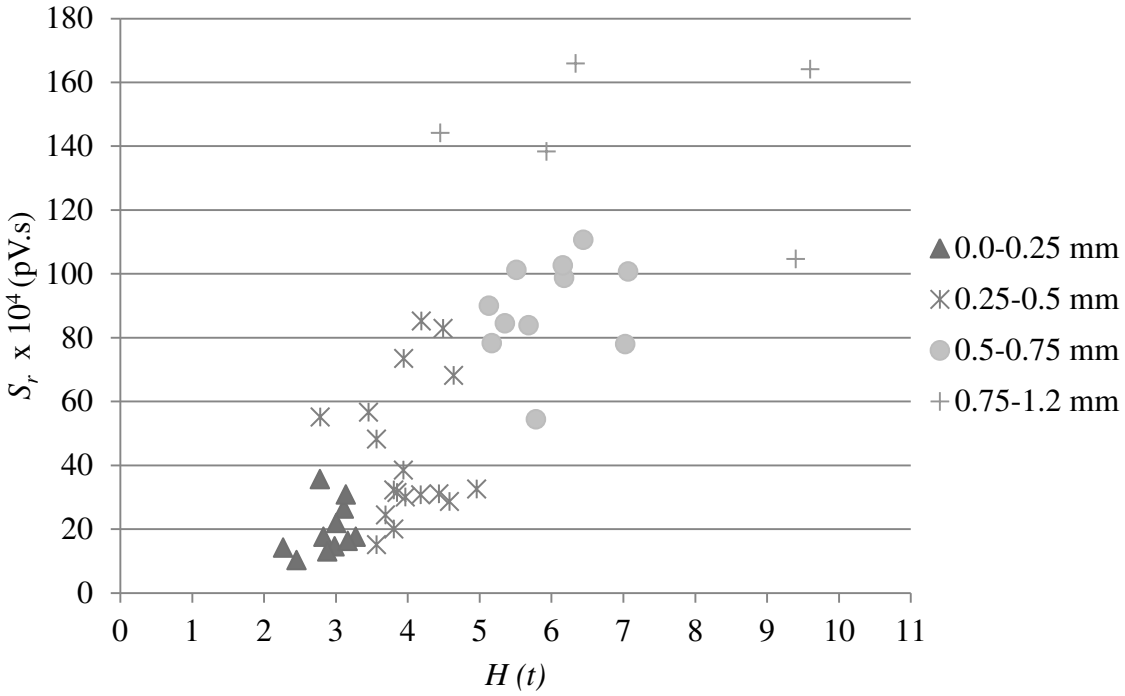

Figure 6.7 Free end slip intensity quantification chart for un-corroded samples

7. Discussion of Results from Experimental Study 4: Evaluation of Concrete-Steel Bond Behaviour in Full-Scale Corroded/Un-Corroded RC Beams

7.1 Introduction

This chapter evaluates the bond behaviour of five corroded and five un-corroded full-scale beams by using the analysis of AE data obtained from four-point load tests. The corroded beams were exposed to accelerated corrosion process before bond testing.

7.2 Results of Corroded Beams after Corrosion Exposure

Four levels of corrosion were targeted in this study including 5%, 10%, 20%, and 30% of steel mass loss. To this end, the corroded beams were subjected to four variable accelerated corrosion exposure periods, as previously explained in **Chapter 5**. The actual percentages of steel mass loss in the corroded parts of the bars were measured at the end of the four-point bond tests and a typical picture of these bars is demonstrated in **Figure 7.1**. The values of both theoretical and actual steel mass loss were also compared in **Table 5.1** (**Chapter 5**) that showed well agreement in all beams.

Figure 7.1 Typical picture of the corroded parts of the bars of all tested beams

7.3 Overall Behaviour and Bond Strength of Tested Beams

7.3.1 Corroded Beams

The occurrence of visual cracks was carefully observed during the load application along the span of all beams. At nearly 25% of average maximum applied loads, all corroded beams exhibited one flexural crack almost at the mid-span. With further loading, three additional flexural cracks were noticed between the loading points of only B5 (long span beam). The increase of load up to approximately 60% of the average maximum applied loads was then found to initiate bar slippage, as detected by one of the LVDTs. The amount of bar slippage increased with continued load application. A typical load versus free end slip curve recorded using one of the left LVDTs (L2) is shown in **Figure 7.2** (taken from B3, as an example). Using the load-slip curves from all LVDTs, the initial

slippage was identified at the time of first significant increase of bar slip in these curves. The LVDT that first detected initial slip in all tested beams is identified in **Table 7.1**. Before failure, all beams (short and long) exhibited an additional diagonal crack at one of the anchorage zones. Also, as mentioned before, all corroded beams had horizontal cracks extending along the bonded length. The width of these cracks increased at the time of failure in all corroded beams. The pictures of a typical bond failure of tested beams can be seen in **Figure 7.3** and the total number of cracks at failure is shown in **Table 7.1**. All corroded beams (B1 through B5) underwent anchorage failure at the corroded side, as expected. The amount of load at first crack and initial slip detection and maximum load resisted by the beam along, with its corresponding value of bar slippage and location of anchorage failure in corroded beams, are all presented in **Table 7.1**. The values of maximum load of each beam were utilized to calculate both steel stress and bond strength using the equations recommended by RILEM committee (Rilem-Fip-Ceb, 1973).

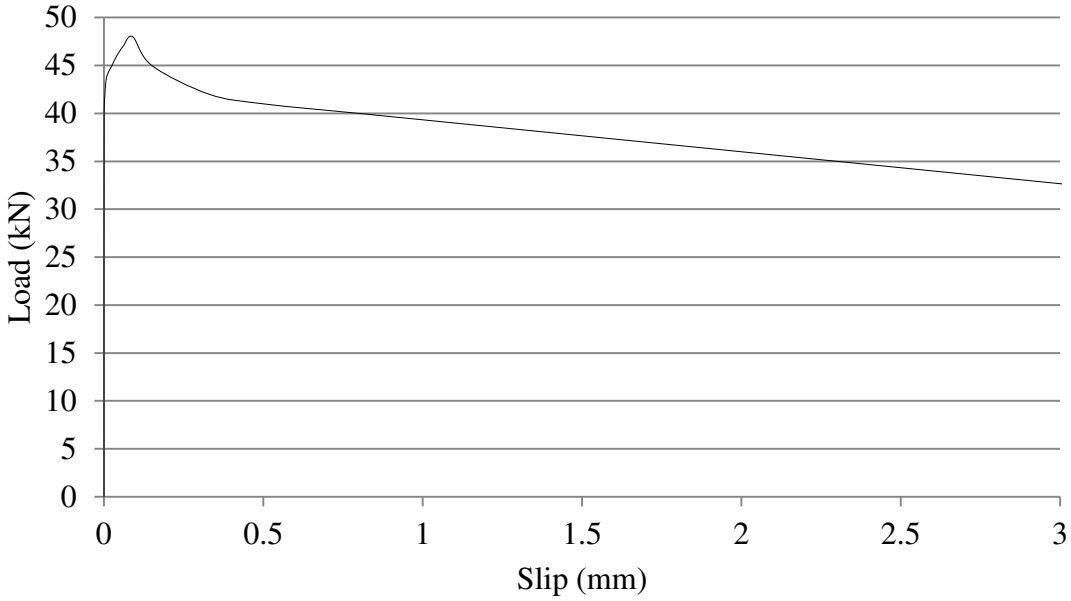

Figure 7.2 Typical load-slip curve for corroded beams (B3)

Figure 7.3 Typical bond failure of corroded beams (Left: anchorage cracking; Right: bars slip)

Table 7.1 Results of four-point load tests of corroded beams

Beam	Load at first flexural crack (kN)	Load at initial slip (kN)	First LVDT detected slip	Maximum load (kN)	Free end slip at maximum load (mm)	Number of cracks at failure	Location of anchorage failure	Calculated steel stress (MPa)	Calculated bond strength (MPa)
B1	26	62	L1	97	0.10	2	Left	242.47	11.88
B2	29	50	L1	85	0.08	2	Left	212.88	10.43
B3	24	43	L2	48	0.09	2	Left	120.62	5.91
B4	22	28	L2	38	0.07	2	Left	94.70	4.64
B5	20	29	L2	35	0.05	5	Left	88.17	4.32

7.3.2 Un-Corroded Beams

All un-corroded beams also exhibited one crack approximately at the mid-span within the constant moment region before reaching 25% of the maximum load. The amount of load recorded at the first crack of all un-corroded beams is reported in **Table 7.2**. After the detection of first crack, the increase of loading resulted in increasing widths of the first crack with no new visible cracks until the occurrence of bar slip in B6, B7, B8, and B9. In contrast, B10 showed an additional three cracks in the constant moment region prior to bar slippage. This could be attributed to the longer length of the constant moment zone in B10 compared to all other tested beams. It should be mentioned that the main purpose of this study was to detect bond failure not first cracking at beam mid-span. However, all tested beams showed mid-span (flexural) cracks before the occurrence of bond damage at one of the anchorage ends. The detection of the initial slip was achieved using the data obtained from the four LVDTs mounted on the bar ends. The LVDT that first identified the slip, magnitude of corresponding load, and location of the LVDT (left or right) in un-corroded beams are all identified in **Table 7.2**.

By further increasing the load, the amount of bar slippage was increased and a new crack appeared in one of the anchorage zones of all un-corroded beams just before failure. It was found that all un-corroded beams also underwent bond failure after the formation of this anchorage crack, as expected. As can be seen from **Table 7.2**, both steel stress and bond strength were also calculated using the equations specified in the RILEM recommendation for obtaining the bond strength of beam specimens (Rilem-Fip-Ceb, 1973). The number of cracks at failure, maximum vertical load resisted by all beams, and corresponding free end bar slip are also shown in **Table 7.2**. Meanwhile, a typical bond stress-slip curve of un-corroded beams (B6) is shown in **Figure 7.4**. It can be noticed from the curve that the amount of bar slip significantly increased after the point of maximum load due to the presence of anchorage crack. Nonetheless, the amounts of bar slip shown in **Table 7.2** are taken at the location of maximum load. These values of bar slip showed to increase by increasing the bonded length (B6 through B9). This increasing trend can be correlated to the higher load resisted by those un-corroded beams associated with larger bonded length as seen in **Table 7.2** This trend matched the results of similar experimental investigations available in the literature (For example: Mangat and Elgarf, 1999; Craig and Soudki, 2005).

Table 7.2 Results of four-point load tests of un-corroded beams

Beam	Load at first visual crack (kN)	Load at initial slip (kN)	Maximum load (kN)	Number of cracks at failure	Calculated steel stress at maximum load (MPa)	Calculated bond strength at maximum load (MPa)	Bond slip location	First LVDT detected slip	Free end slip at maximum load (mm)
B6	16	31	68	2	168.89	16.55	Left	1	0.07
B7	21	55	121	2	303.50	14.87	Right	3	0.12
B8	22	78	159	2	397.69	12.99	Left	2	0.29
B9	25	93	166	2	413.91	10.14	Left	1	0.45
B10	13	61	125	5	312.68	15.32	Right	4	0.15

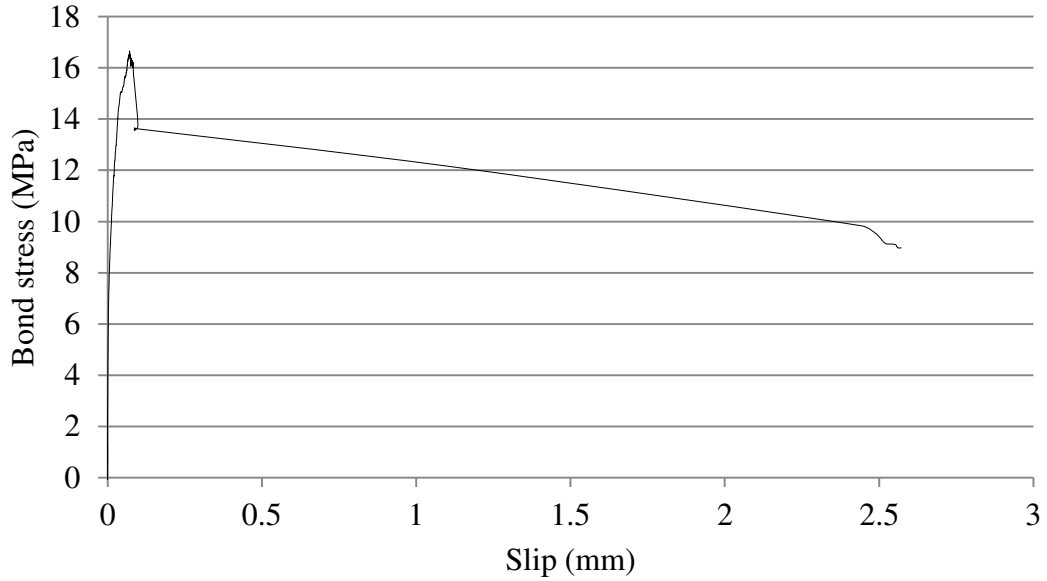

Figure 7.4 Typical load-slip curve for un-corroded beams (B6)

7.4 Bond Damage Identification of Corroded/Un-Corroded Beams Using AE Analysis

The raw AE data attained from the four-point load tests of all tested beams were filtered using the same approach presented in **Chapter 6**. Besides, an intensity analysis on the

signal strength results was also completed as previously explained in **Chapter 6** to obtain the magnitudes of historic index (*H (t)*) and severity (S_r). In this study, the variations of AE number of hits, cumulative signal strength (CSS), *H (t)*, and S_r versus test time were analyzed to achieve an early detection of damage in all beams. **Figures 7.5**-**7.6** present the changes of these AE parameters through the test time of B3 and B9 obtained from Sensor 1 (as an example of corroded and un-corroded beams, respectively). It can be noticed that the AE number of hits, CSS, and S_r values obtained from the same sensor followed a very similar trend of variation within all tested beams. Multiple researchers have found that the locations of sudden changes in these AE parameters can be correlated to damage progression in concrete structures (Mangual et al., 2013a; 2013b; Di Benedetti and Nanni, 2014; ElBatanouny et al., 2014; Abdelrahman et al., 2015; Gallego et al., 2015). On this basis, the analysis of these parameters was done in conjunction with the results of visual inspection of cracks and data recorded using LVDTs to attain an early identification of damage, as explained in the following subsections. It is worth noting that, in potential field application of AE monitoring, similar analysis of AE signal parameters should be implemented in order differentiate between the AE events related to bond damage from other AE sources.

(a)

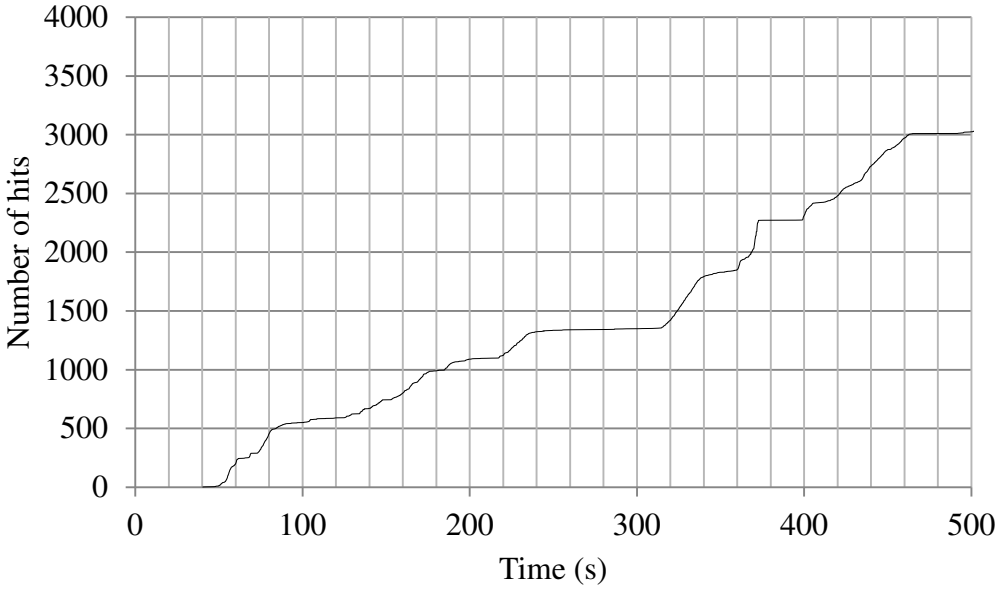
4000
3500
3000
2500
2000
1500
1000
500
0
Number of hits
0
100
200
300
400
500
Time (s)

(b)

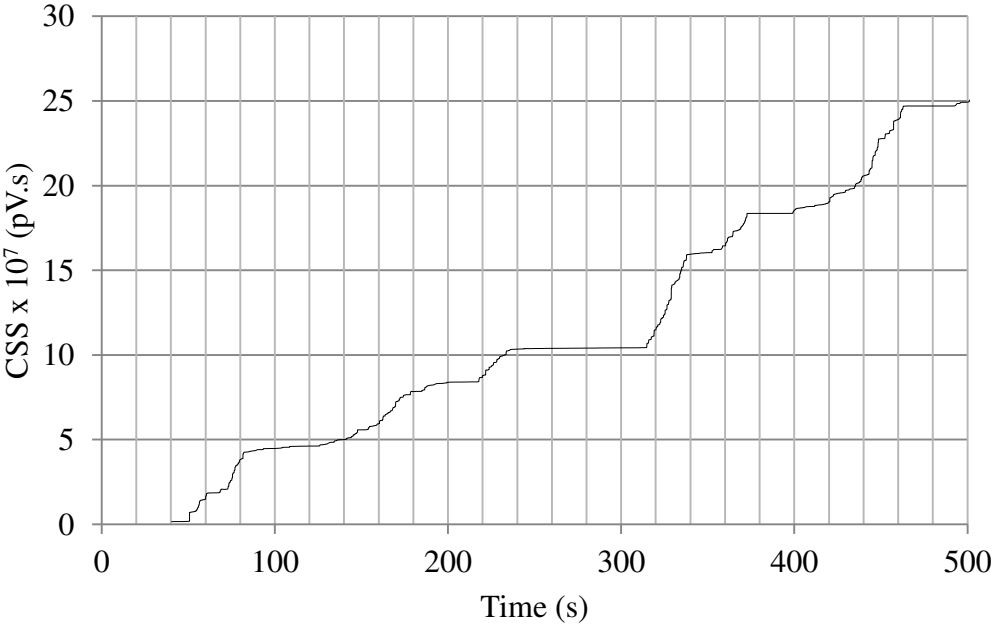
30
25
20
15
10
5
0
CSS x 10^7 (pV.s)
0
100
200
300
400
500
Time (s)

(c)

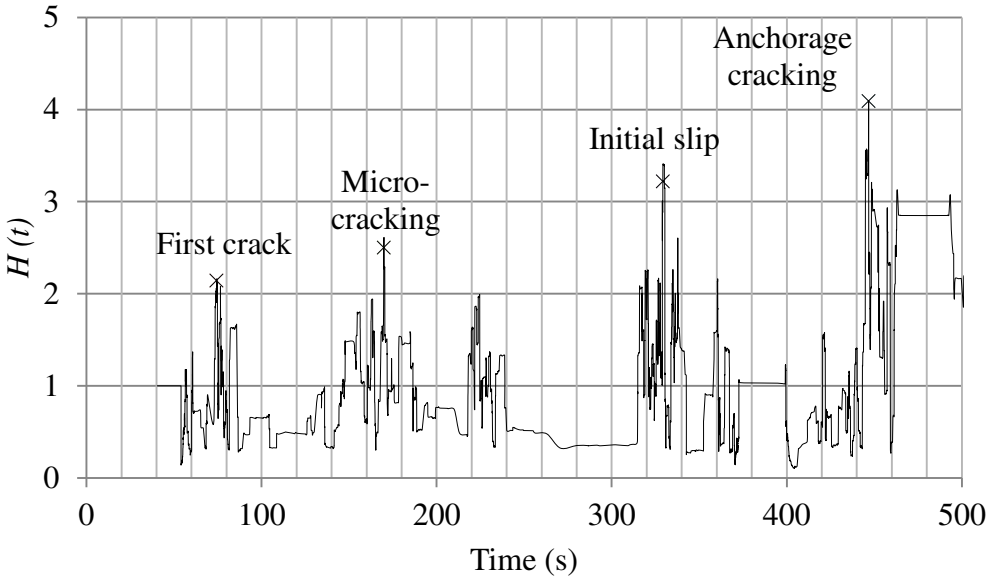

(d)

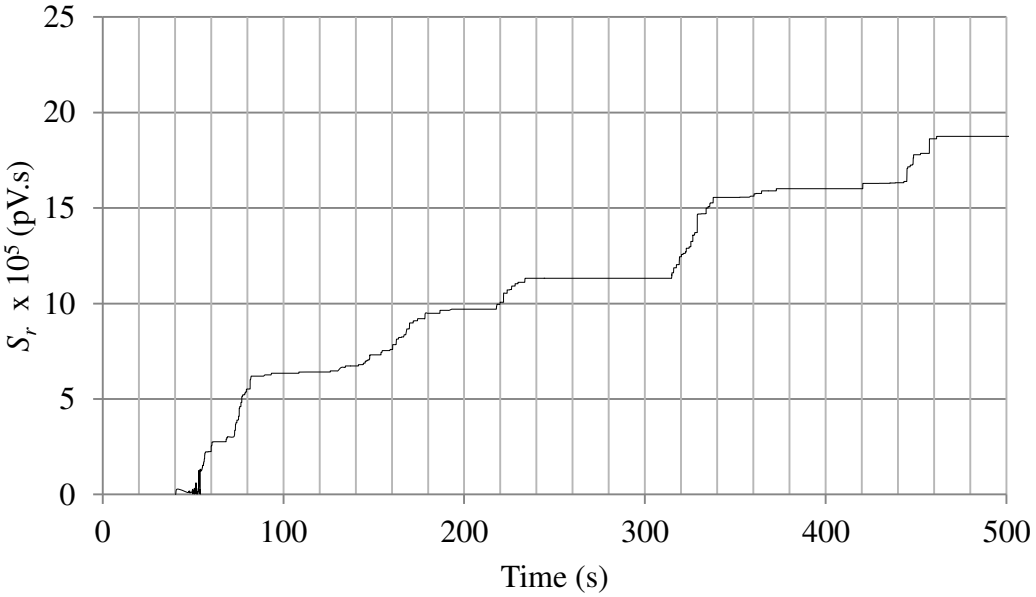

Figure 7.5 Variations in AE parameters versus test time of B3 recorded by Sensor 1: (a) number of hits, (b) CSS, (c) *H (t)*, and (d) S_r

(a)

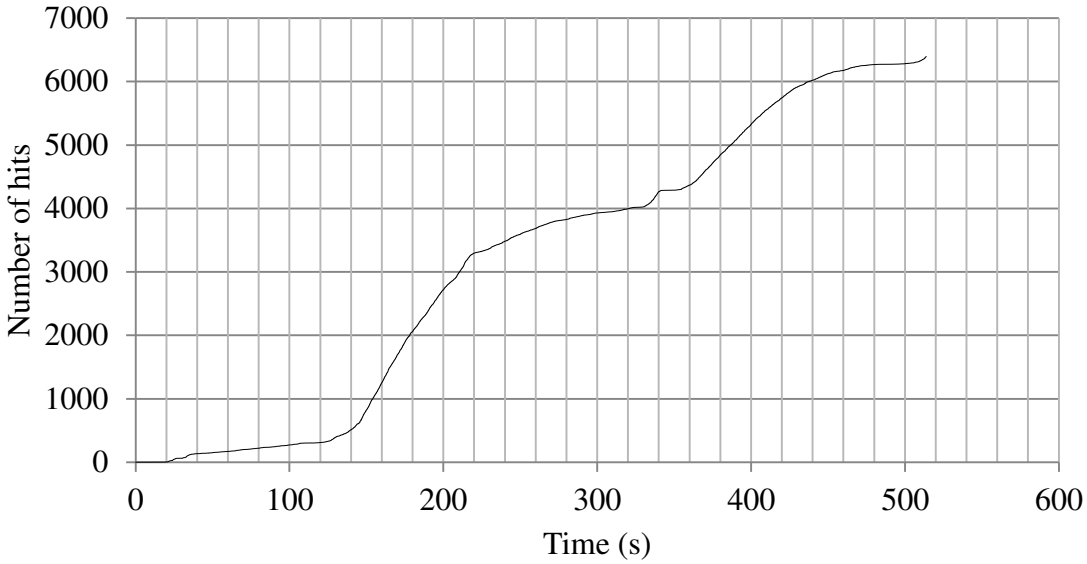
Number of hits
7000
6000
5000
4000
3000
2000
1000
0
0
100
200
300
400
500
600
Time (s)

(b)

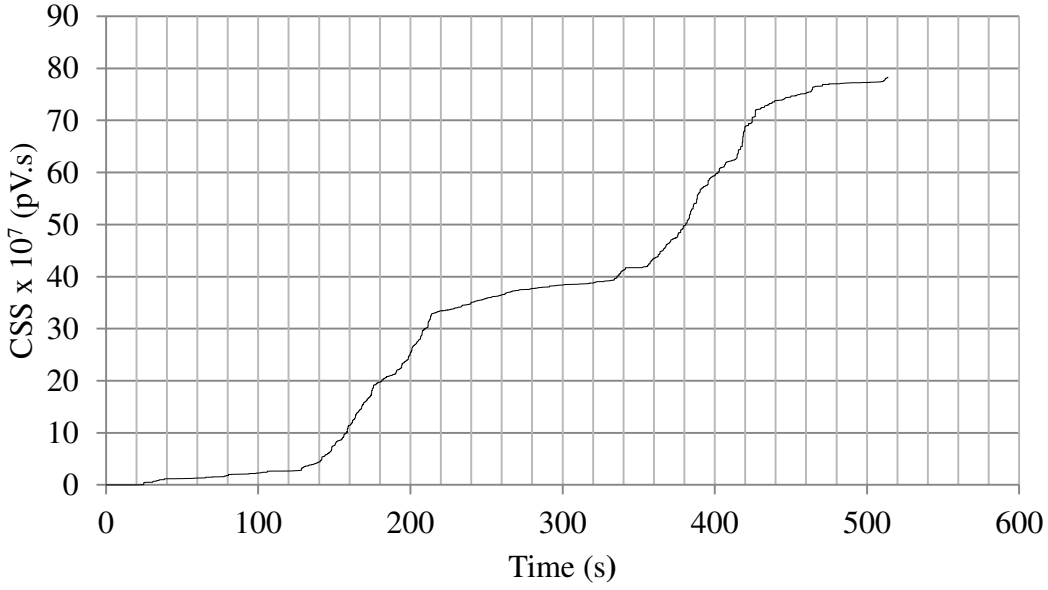
CSS x 10^7 (pV.s)
90
80
70
60
50
40
30
20
10
0
0
100
200
300
400
500
600
Time (s)

(c)

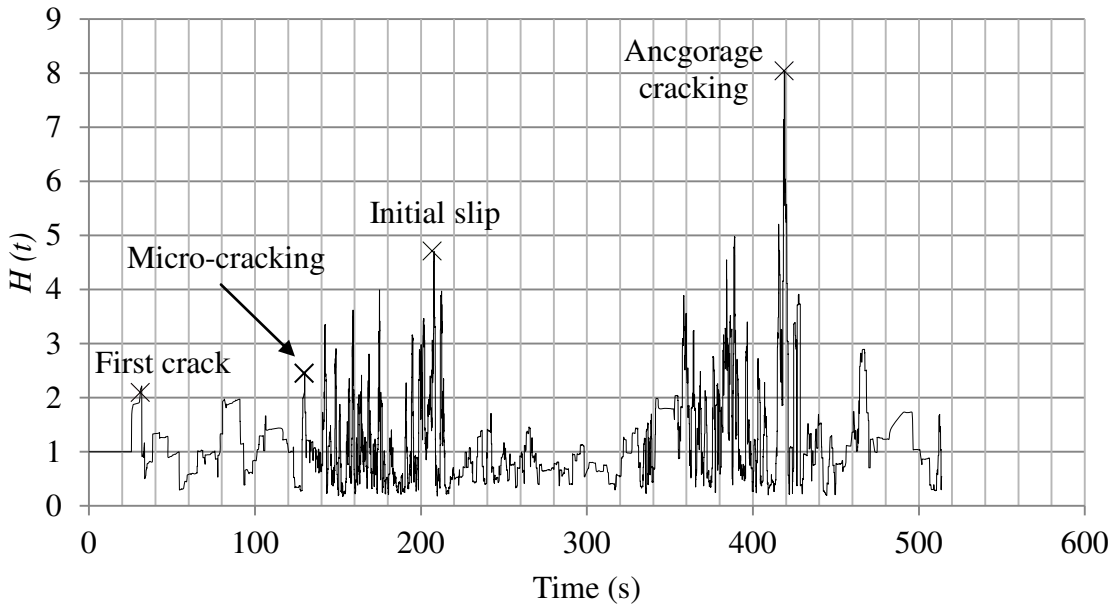

(d)

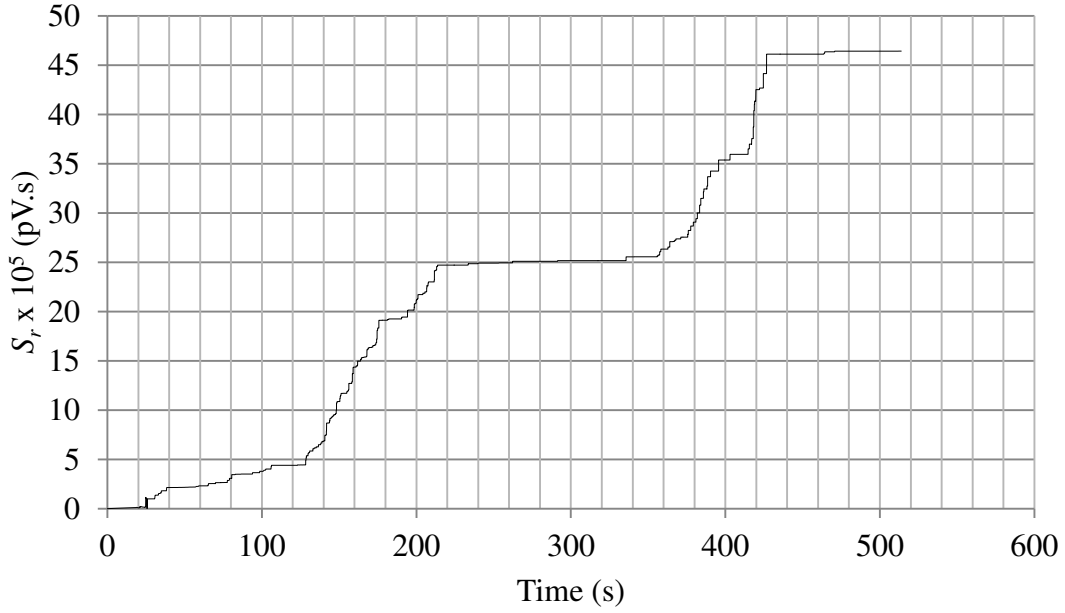

Figure 7.6 Variations in AE parameters versus test time in B9 recorded by Sensor 1: (a) number of hits, (b) CSS, (c) *H (t)*, and (d) S_r

7.4.1 Detection of First Crack

The values of the number of hits, CSS, and S_r in **Figure 7.5** witnessed an overall increase throughout the test time until bond failure of B3 occurred at 478 s. Sudden variations in the number of hits, CSS, and S_r graphs (slope change) can be noticed at certain locations throughout the test. These locations were also accompanied by sudden jumps in the values of *H (t)* as shown in **Figure 7.5b**. The first point of sudden change in the number of hits, CSS, *H (t)*, and S_r values can be observed from **Figure 7.5** at 74 s, which can be related to the growth of the first crack. This crack was visually observed during the test at approximately 84 s near the mid-span of all seven beams. The detection of this crack was also confirmed using the load versus time history, which indicated a small drop in the load at that time of first crack development. It is worth noting that both micro-cracking and crack growth are significant sources of acoustic emission in reinforced concrete (Fowler et al., 1998).

Likewise, **Figure 7.6a, b** that the first noticeable increase (at the points of slope change) in the number of hits and CSS are located at nearly 31 seconds from the beginning of the test. Meanwhile, a sharp increase in the values of *H (t)* and S_r was also found at 31 seconds (**Figure 7.6c, d**). This significant increase in AE activity can be correlated to the growth of first crack, which was visually detected during the test on B9 noted at approximately 38 seconds from the test beginning. It is worth noting that best efforts were done to allow the synchronization between visual observation of cracks and AE/LVDT data acquisition systems. This target was achieved by looking at the start time of recording data and correcting any shift between the starting times of all acquired data.

The identification of first crack using AE analysis was similarly conducted in all other beams (corroded and un-corroded) and enabled earlier detection than visual inspection. **Table 7.3** demonstrates the values of AE parameters including signal amplitude, number of hits, CSS, *H (t)*, and S_r at the time of detecting first crack in all corroded and un-corroded beams (using the analysis of CSS and *H (t)*). It was also found that the AE signals recorded at the time of first crack in all beams were characterized by higher amplitudes (normally > 65 dB) than those recorded prior to first crack observation (**Table 7.3**). It should be noted that both *H (t)* and S_r curves showed a clearer detection of the first crack than those of number of hits and CSS (**Figures 7.5**-**7.6**), which was confirmed in all beams. The values of AE parameters (acquired from the same sensor location in each beam) related to the detection of first crack show (in most of tested beams) relatively small variations among the tested beams (**Table 7.3**). However, some beams exhibited relatively larger variations between AE parameters recorded using the same sensor location. These relatively larger variations may be associated with the differences in both crack heights and widths and the distance from the crack to the attached sensors.

Table 7.3 Different AE parameters at the time of first crack identification for corroded/un-corroded beams

Beam	Amplitude (dB)			Number of hits			CSS (pV.s) x 10^7			*H (t)*			S_r (pV.s) x 10^5		
	CH1	CH2	CH3	CH1	CH2	CH3	CH1	CH2	CH3	CH1	CH2	CH3	CH1	CH2	CH3
B1	78	81	71	164	305	167	1.85	2.87	1.71	1.81	1.95	1.84	2.95	3.50	2.26
B2	74	79	73	82	157	56	2.69	3.11	2.46	1.61	2.33	1.56	1.59	3.43	2.48
B3	71	73	70	309	326	237	2.57	2.91	1.43	2.14	2.67	1.61	3.09	3.21	2.07
B4	75	76	66	143	337	149	2.08	2.88	2.47	1.53	2.12	1.68	1.93	3.07	1.75
B5	73	76	71	69	295	65	1.48	2.72	2.22	1.68	1.89	1.74	1.91	2.76	2.43
B6	82	82	82	192	222	167	1.25	1.81	1.23	4.55	4.59	3.65	2.19	3.21	2.17
B7	73	75	75	89	219	97	1.45	1.99	1.81	2.47	2.68	2.27	2.73	3.52	3.29
B8	77	84	73	242	272	189	0.76	1.10	0.61	4.53	4.72	2.06	1.09	1.75	0.79
B9	75	79	73	68	131	131	0.69	1.28	0.64	2.09	2.66	2.27	1.35	2.38	1.12
B10	72	78	72	105	211	110	0.39	1.5	1.36	2.12	3.64	2.53	1.77	2.53	1.63

CH1 = data from Sensor 1, CH2 = data from Sensor 2, and CH3 = data from Sensor 3

7.4.2 Detection of Rebar Slip and Bond Failure at the Anchorage Zone

The analysis of AE data was also implemented to attain early detection of bar slip for all beams. **Figure 7.5** indicates that there is a second point of sudden increase in *H (t)* at 169 s, which also exhibited a second slope change in number of hits, CSS, and S_r curves for B3. **Figure 7.6** also shows a second slope change followed by sharp increase in the values of number of hits, CSS, *H (t)*, and S_r starting at nearly 125 seconds in B9. This increased AE activity may be attributed to the onset of micro-cracking at the concrete-steel interface. Moreover, it can be related to the ribs-to-concrete mechanical interlock that follows the breakage of chemical adhesion between concrete and steel. It should be mentioned that both micro-cracking and ribs-to-concrete mechanical interlock are considered sources of acoustic emission (Gallego et al., 2015). This high AE activity was associated with a value of the calculated steel stress of 3.7 MPa (from the load history data of B3). This value of stress is within the range of steel stress that causes micro-

cracks at the concrete-steel interface (0.8–3.0 f_{ct}), which is typically followed by macro-cracking and bar slip inception (CEB-FIP, 2000; Gallego et al., 2015). However, this detection of micro-cracking cannot be confirmed as it is not substantiated with any other evidence.

Following this stage, the AE parameters in **Figure 7.5** kept increasing with further loading until they reached a third point of sudden rise in *H (t)* at 329 s, with a higher slope change of the number of hits, CSS, and S_r curves at the same location. This point is attributable to bar slippage initiation of one of the main bars at one of the anchorage zones. This high AE activity represents the occurrence of macro-cracking in the concrete core around the bar preceding the onset of bar slip (CEB-FIP, 2000; Gallego et al., 2015). The detection of initial slip of B3 was alternatively confirmed using the data from LVDTs recorded during the test. For example, the initial slip in B3 was detected at nearly 338 s from the left LVDTs (L2). It can also be observed from **Figure 7.6** that the third peak value of *H (t)* during the test period (4.41 at 207 seconds, **Figure 7.6c**) can be attributed to the initiation of bar slip. At this point, a noticeable change in the slope of the curves of number of hits, CSS, and S_r can also be seen from **Figure 7.6a, b, d**. This finding was further confirmed by the detection of bar slip at approximately 219 seconds using the readings of LVDT1 in B9. It should be mentioned that intensity analysis parameters (*H (t)* and S_r) enabled a better indication of bar slip (sudden rise in *H (t)* and sharper slope change of S_r) than the number of hits and CSS, as seen from **Figures 7.5-7.6**. The identification of initial slip was similarly performed in all other tested beams (corroded and un-corroded) and the corresponding values of different AE parameters are summarized in **Table 7.4**. The results of all tested beams proved the feasibility of AE

analysis in detecting early the initiation of bar slippage before its observation from the LVDTs readings. These results manifest the effectiveness of AE monitoring in identifying early stage bond deterioration of both corroded and un-corroded concrete structures prior to its visual detection.

Table 7.4 Different AE parameters at the time of initial slip detection for corroded/un-corroded beams

Beam	Amplitude (dB)			Number of hits			CSS (pV.s) x 10^7			*H (t)*			S_r (pV.s) x 10^5		
	CH1	CH2	CH3	CH1	CH2	CH3	CH1	CH2	CH3	CH1	CH2	CH3	CH1	CH2	CH3
B1	85	77	74	2033	1972	1447	20.01	15.16	17.10	3.69	2.68	2.29	18.40	13.90	11.89
B2	75	73	71	1843	1664	849	17.62	13.35	8.52	3.43	3.06	2.01	15.51	12.55	10.60
B3	72	72	70	1609	1479	893	14.10	11.60	6.93	3.22	2.69	1.96	14.70	13.10	9.72
B4	80	75	74	1443	1311	912	9.89	7.43	5.23	2.79	2.39	2.05	13.31	11.72	9.15
B5	85	77	72	997	815	562	8.64	6.44	4.55	2.88	2.24	2.04	10.39	7.37	2.88
B6	81	80	72	1953	1257	1020	21.1	20.3	10.1	2.69	2.52	2.41	21.9	18.8	14.9
B7	78	80	86	1670	2039	2630	12.2	22.7	25.9	2.77	2.79	3.8	16.8	18.4	22.1
B8	84	83	81	2799	2443	1881	27.6	24.2	13.1	3.58	3.53	3.33	23.3	18.6	17.1
B9	87	84	82	2903	2794	2329	29.5	28.3	19.3	4.71	4.45	3.42	23	21.6	18.4
B10	66	71	78	1006	3346	3048	9.13	35.7	23.9	2.44	3.18	4.54	12.3	29.6	20.4

CH1 = data from Sensor 1, CH2 = data from Sensor 2, and CH3 = data from Sensor 3

Figures 7.5-7.6 demonstrate a continual increase in the number of hits, CSS, and S_r values after the detection of initial slippage until beams failure. This increase can be correlated to the increase in the amount of bar slippage, which eventually resulted in the formation of anchorage cracking and failure of all beams (an example can be seen in **Figure 7.3**). The bar slippage is also anticipated to be one of the sources of AE in reinforced concrete (Fowler et al., 1998; Iwaki et al., 2003). The bar slippage continued to increase and became visible, as seen from the picture of B9 as an example (**Figure 7.3**). In the meantime, a sudden increase (reaching its maximum value) in *H (t)* can be noticed from **Figure 7.5b** at 447 s. This increase in *H (t)* was also associated with a noticeable

slope change in the number of hits, CSS, and S_r charts, which can be related to the growth of the failure crack in the anchorage zone. This was confirmed in B3 by visual observation of a large crack at the anchorage zone just before the beam failed at 478 s. It is worth noting that all other beams (both corroded and un-corroded) behaved similarly to B3 in terms of correlation between AE parameters and different stages of damage until bond failure occurred. The values of these AE parameters of all beams at the stage of anchorage crack identification are reported in **Table 7.5**.

Figure 7.7 Bar slippage in B9 after failure

Table 7.5 Different AE parameters at the time of anchorage cracking onset for corroded/un-corroded beams

Beam	Amplitude (dB)			Number of hits			CSS (pV.s) x 10^7			*H (t)*			S_r (pV.s) x 10^5		
	CH1	CH2	CH3	CH1	CH2	CH3	CH1	CH2	CH3	CH1	CH2	CH3	CH1	CH2	CH3
B1	86	82	78	3771	3277	2691	28.22	22.37	19.12	5.34	4.41	3.89	23.91	19.10	17.22
B2	86	83	77	3634	3462	2133	23.70	20.85	18.31	4.61	3.03	2.81	18.50	18.31	15.22
B3	77	72	71	2829	2782	1881	22.00	20.09	14.33	4.09	3.05	2.85	17.20	15.41	14.33
B4	83	82	74	2321	2009	1631	19.42	17.91	13.17	3.02	2.86	2.36	19.11	14.02	12.34
B5	83	80	71	1990	1832	1266	15.43	12.95	9.12	2.89	2.61	2.35	16.74	13.22	11.23
B1	83	81	78	3338	2375	2111	24.5	22.3	17.4	5.77	3.85	3.87	30.4	24.3	18.2
B2	68	71	73	2935	3287	4012	19.8	26.1	30.6	4.09	4.43	5.92	19.3	22.3	34.5
B3	75	74	72	4834	4477	3577	35.5	31.3	26.8	6.26	5.83	4.46	36.7	23.6	22.6
B4	85	84	80	5725	5501	5331	67.9	51.8	48.3	8.04	5.37	5.07	41.4	36.6	29.5
B5	71	81	82	5454	5707	5850	47.7	49.9	83.2	3.52	3.61	5.6	27.7	39.3	43.6

CH1 = data from Sensor 1, CH2 = data from Sensor 2, and CH3 = data from Sensor 3

7.5 Effect of Anchorage Length on Different AE Parameters

The length of the bonded part of the rebar was varied in B6, B7, B8, and B9 from 100 to 400 mm. This change had a significant impact on the force transfer between concrete and steel. Therefore, these beams showed variable load resistance and bar slippage, as described in **Table 7.2**. This was also the case for the effect of changing bonded length on AE parameters as soon as the bar slip was detected, as demonstrated in **Tables 7.4-7.5 and Figure 7.8**. The use of longer bonded length resulted, in general, in higher average values of number of hits, CSS, *H (t)*, and S_r. For example, varying the bonded length from 100 to 400 mm (B6 versus B9) yielded nearly 90%, 50%, 65%, and 13% increase in the number of hits, CSS, *H (t)*, and S_r, respectively, at the stage of bond slip detection (**Table 7.4 and Figure 7.8a**). Similar increasing trends of these AE parameters from the increase in the bonded length were also obtained at maximum load stage carried by all beams (**Table 7.5 and Figure 7.8b**). For instance, increasing the bonded length from B1 to B4

caused an overall rise in number of hits, CSS, *H (t)*, and S_r of about 112%, 162%, 37%, and 47%, respectively. These trends at both the detection of slip and maximum load were also present in all AE parameters due to increasing the bonded length from 100 to 200 mm, 200 to 300 mm, and 300 to 400 mm (**Tables 7.4-7.5 and Figure 7.8**). On the contrary, no clear relationship was obtained between changing the bonded length and the resulting AE parameters at the stage of first crack detection (**Table 7.3**). For example, by comparing B6 versus B7 it was noticed that increasing the bonded length from 100 to 200 mm did not seem to significantly increase or decrease the average AE parameters in those beams. These inconsistent trends of variation in AE parameters among the tested beams at the time of first crack detection can be attributable to the different crack patterns observed between all tested beams.

(a)

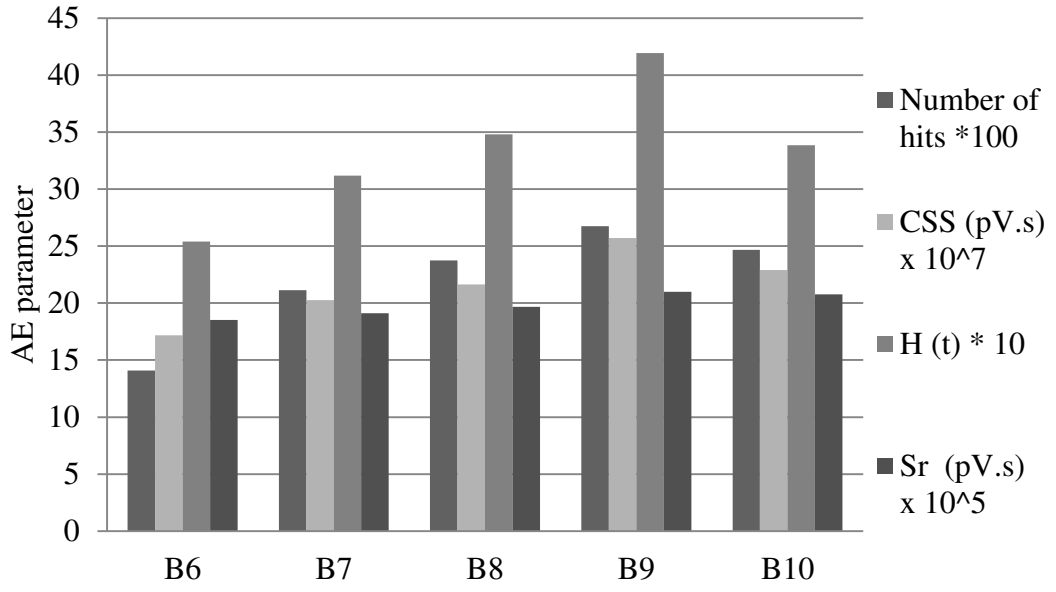

(b)

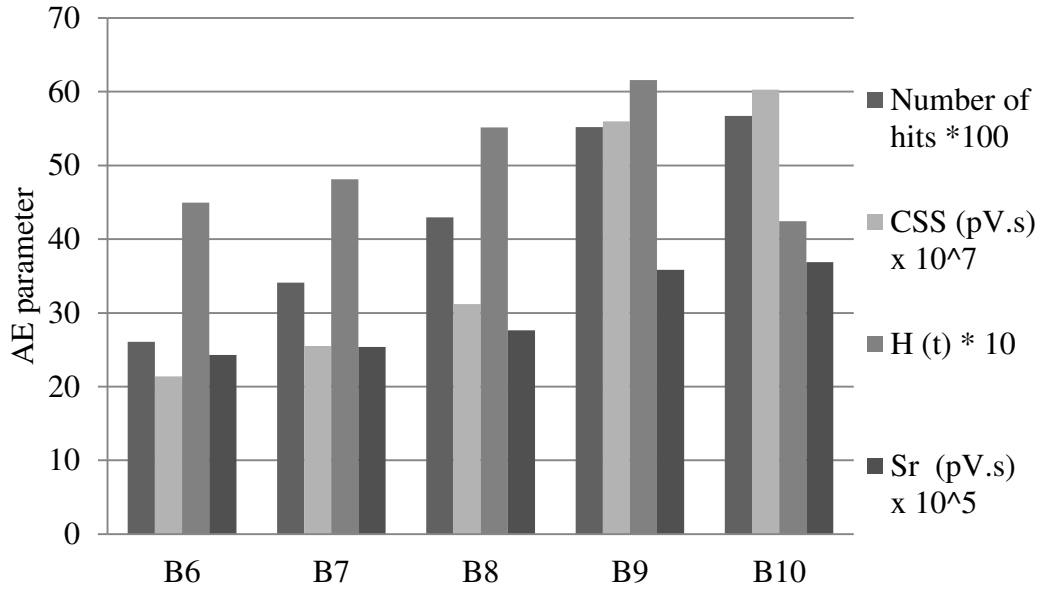

Figure 7.8 Relationship between bonded length and AE parameters: (a) at bond slip detection and (b) at maximum load/slip

7.6 Effect of Sensor Location on Different AE Parameters

As previously explained, three sensors were located on each beam at different distances from the bonded length. The sensor location measured from the centre of the bonded length was also varied in the un-corroded beams owing to the increased bonded length (B6, B7, B8, and B9) and longer span of B10. These changes in the sensor position showed a notable effect on the individual AE signal parameters (especially signal amplitude) as well as other studied AE parameters (number of hits, CSS, *H (t)*, and S_r) at all levels of damage (**Tables 7.3-7.5**). **Figure 7.9** presents the relationship between sensor location and amplitude of the acquired signals at the time of detection of bar slippage, using AE analysis in all un-corroded beams. It can be seen that the farther the sensor location is from the bonded length, the smaller the amplitude of the same signal detected

by the three sensors is in each beam. A linear trend of decline in the amplitude values in all beams can be noticed from **Figure 7.9**. For instance, the amplitude of signals detected in B10 decreased by approximately 15% when the sensor location changed from 435 to 1505 mm (**Figure 7.9**). This percentage of reduction was the maximum value obtained from all tested beams (corroded and un-corroded) due to the longer span of B10 compared to other beams. This slight decrease in the amplitude of these signals can be expected from the wave propagation through concrete, which led to wave attenuation and lower signal amplitudes. In addition, these lower amplitudes can be related to the existence of cracks in all these beams, which are considered one of the main sources of wave attenuation in concrete because of scattering and reflections (Ervin, 2007). It should be noted that the wave attenuation was more pronounced in B5 and B10 than in all other beams due to the longer span and the larger number of cracks.

The influence of sensor location on the amplitude of the signals recorded at the maximum applied load prior to failure of beams followed a similar reduction trend (**Table 7.5**) to that associated with the initial slip detection. It can also be seen from both **Table 7.4 and 7.5** that the closer the sensor was to the side of bar slippage, the larger the values of other AE parameters were, including number of hits, CSS, *H (t)*, and S_r. Meanwhile, the values of all AE parameters detected at the time of first crack using Sensor 2 (CH2) were slightly higher than those obtained from both Sensor 1 (CH1) and Sensor 3 (CH3). This can be seen from the values of amplitude, number of hits, CSS, *H (t)*, and S_r associated, in all beams, with the detection of first crack (shown in **Table 7.3**). For example, the values of amplitude, number of hits, CSS, *H (t)*, and S_r obtained from Sensor 2 were 8%, 48%, 9%, 31%, and 37%, respectively, higher than those recorded using Sensor 3 in B10 (**Table**

7.3). This overall higher AE activity from CH2 can be attributed to the closer location of Sensor 2 to the first crack observed in all beams than both Sensor 1 and Sensor 3. It is worth noting that although the sensors' position had an impact on the magnitudes of AE parameters, all sensors enabled the detection of different stages of bond damage in all beams. Nonetheless, these findings are only based on a maximum distance of 1505 mm from the slip location (furthermost sensor in B5 and B10). Larger distances between sensors should be investigated to verify the outcomes of this study.

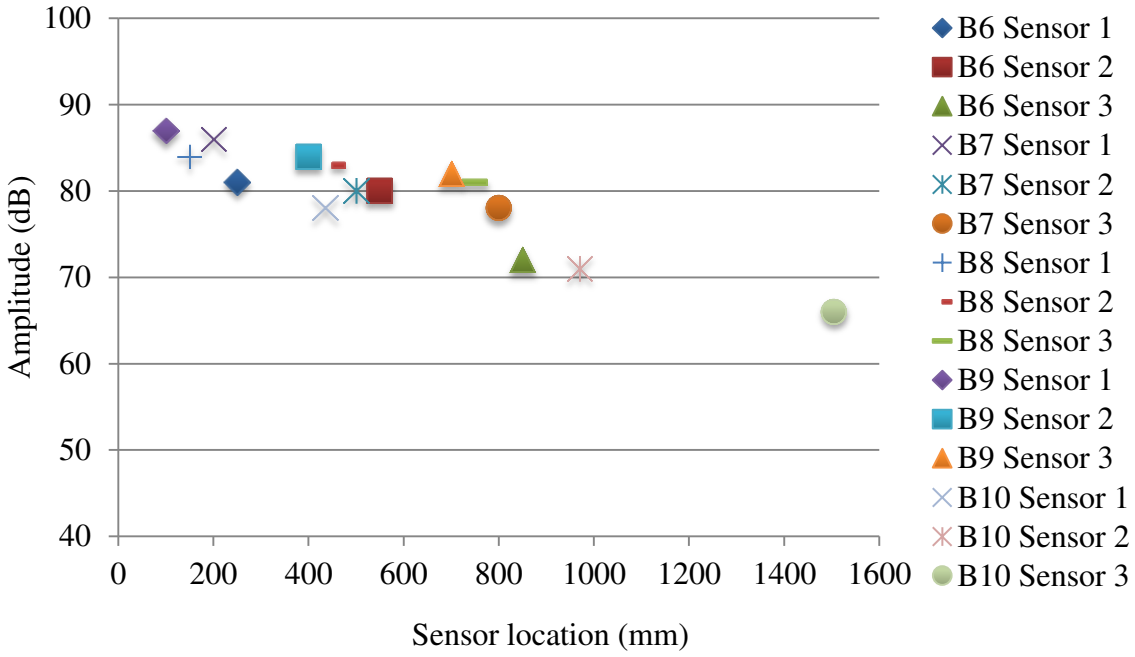

Figure 7.9 Amplitudes of signals recorded at bar slip detection versus sensor locations for un-corroded beams

7.7 Effect of Corrosion Level on Different AE Parameters

The exposure of beams to corrosion yielded a significant impact on the values of corrosion cover cracking as well as on the results of four-point load tests shown in **Table**

7.1. Increased corrosion from 0% to 30% of steel mass loss resulted in larger corrosion crack widths, lower load resistance, and lower bond strength of the tested beams. This varied corrosion exposure also significantly affected the values of AE parameters (number of hits, CSS, *H (t)*, and S_r) at both initial slip and anchorage cracking stages (**Tables 7.4-7.5**). However, at the stage of first crack detection no noticeable changes were observed in the average AE parameters (signal amplitude, number of hits, CSS, *H (t)*, and S_r) between beams with varied corrosion levels (**Table 7.3**). These insignificant variations of AE parameters between all beams at first crack can be justified by the similar load values at the time of first crack detection among the tested beams with variable corrosion levels (**Table 7.1**).

Tables 7.4-7.5 also indicated that the average values of signal amplitude witnessed no evident changes between corroded/un-corroded beams or between corroded beams with variable exposure. On the other hand, higher corrosion degrees reduced the average values of number of hits, CSS, *H (t)*, and S_r at both initial slip and anchorage cracking stages. For instance, changing the corrosion level from 0% to 30% (B10 versus B5) decreased the average values of number of hits, CSS, *H (t)*, and S_r by nearly 68%, 71%, 30%, and 67% at initial slip stage and by about 70%, 79%, 38%, and 63% at anchorage cracking stage. Similar trends of reduction in these AE parameters were also warranted by increasing corrosion from 0% to 30% in B7 and B4, respectively. In addition, increasing the percentage of steel mass loss from 5% to 10%, 10% to 20%, and 20% to 30% had a similar influence on the average values of number of hits, CSS, *H (t)*, and S_r (**Tables 7.4-7.5**). These overall reduced AE parameters were related to the contribution of corrosion in bar expansion causing cover cracking, thus reducing the load capacity of beams at both

initial slip and anchorage cracking stages. The results of corrosion presented in **Chapter 5** show that higher corrosion exposure yielded higher cover crack widths. These increased corrosion crack widths were expected to reduce the chemical adhesion, confinement, and friction between concrete and corroded bars. Moreover, these high corrosion levels led to a minimized contribution of rib bearing and consequently an overall lower load transfer between steel and concrete. As a result, lower AE activities (at initial slip and anchorage cracking stages) were anticipated due to the increase in corrosion level from 0% up to 30% in all tested beams.

7.8 Bond Damage Classification of Tested Beams Using AE Intensity Analysis

The average values of *H (t)* and S_r obtained from the three sensors in all beams with 200 mm bonded lengths (B1, B2, B3, B4, B5, B7, and B10) were calculated and used to develop a damage classification chart (**Figure 7.10**). The chart categorizes three stages of damage for all tested beams: first crack, initial slip, and anchorage cracking detection. The figure shows that the range of *H (t)* values (1.77-2.76) and S_r values (2.24-3.18 x 10^5 pV.s) were found to represent first crack onset. The initiation of bar slip can be anticipated if the magnitudes of *H (t)* and S_r ranged between 2.39-3.39 and 6.88-20.77 x 10^5 pV.s, respectively. Similarly, the occurrence of anchorage cracking can be predicted if the amounts of *H (t)* and S_r were within 2.61-4.81 and 13.65-36.87 x 10^5 pV.s, respectively. It can be observed from the chart that the magnitudes of *H (t)* and S_r exhibited the largest variations between the tested beams at the stage of anchorage cracking. These large differences in the values of *H (t)* and S_r at this stage can be related to the notable changes across all beams in the size of anchorage cracks. Further testing is

needed to quantify the size of anchorage cracks and to relate it to the *H (t)* and S_r in order to refine the data presented in this chart.

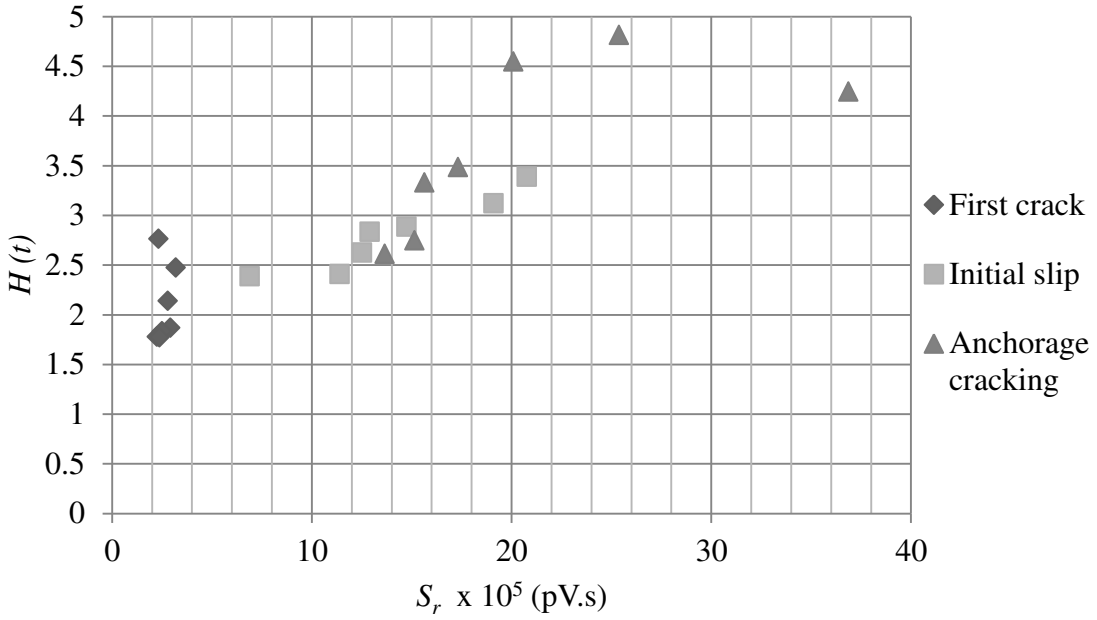

Figure 7.10 Damage classification chart for the 200 mm bonded length beams

8. Conclusions and Recommendations

8.1 Conclusions

The research program completed in this thesis consisted of four successive experimental studies involving the utilization of AE monitoring for both damage detection and assessment of concrete structures. These investigations aimed at the prognosis/diagnosis of steel corrosion, corrosion-induced cover crack growth detection/quantification, and identification/assessment of bond integrity between corroded/un-corroded steel and concrete in both small- and full-scale RC elements. The analysis of the AE data acquired from these extensive investigations and its comparison with all experimental measurements and visual observations attained from all tests led to the following conclusions:

8.1.1 Corrosion Detection and Crack Growth Monitoring Using AE Sensors in Small-Scale RC Samples

- It was confirmed that reviewing the history of CSS of all tested samples throughout the test could be feasible for detecting different stages of corrosion progression (corrosion initiation, cracking, and severe damage stages up to 5% of steel mass loss). These stages were found to occur at locations with a sudden increase of the CSS, $H(t)$, and S_r versus time curves. However, the intensity analysis curves provided a clearer detection of corrosion initiation and propagation.

- The analysis of AE parameters (CSS, $H(t)$, and S_r) showed superior performance in detecting the corrosion initiation earlier than the HCP standard test. In addition, the results of $H(t)$, and S_r showed to be correlated well with the extent of damage resulting from corrosion progression.
- CSS analysis can only be utilized for early detection of corrosion initiation and cannot be applied for estimating the degree of corrosion. The magnitude of CSS showed a considerable variation within the tested samples despite the similar increasing trend with higher degrees of damage. On the other hand, the values of $H(t)$, and S_r exhibited non-significant variations between different tested samples at the same degree of corrosion.
- The rate of increase in CSS, $H(t)$, and S_r values versus time after the inception of cover cracking was found to be less than that found at earlier stages (corrosion initiation and cracking). This trend may be attributed to the continuous opening of cracks, which can lead to increased wave attenuation and result in lower values of signal strength.
- The growth of corrosion-induced cover cracks due to corrosion propagation showed a significant impact on different AE parameters, which resulted in an overall increase in the results of number of hits, CSS, and CE and a general declining trend in the b-values in all tested samples regardless of the cover thickness and corrosion level. The variation of these parameters with respect to the test time showed a similar increasing trend in all tested samples.

- Increasing the cover thickness from 20 to 30 mm and from 30 to 40 mm resulted in an overall reduction of the number of hits, CSS, and CE and an increase in the b-values, at all degrees of steel mass loss in all tested samples. However, this reduction is mostly attributed to the higher crack widths in samples with 20 mm covers than their 30 and 40 mm counterparts.
- No significant variations in the amplitude or peak frequencies of detected AE hits between all tested samples, regardless of cover thickness or percentage of steel mass loss. The values of amplitudes and peak frequencies in all tested samples ranged from 45 to 85 dB and from 19 to 111 kHz, respectively.
- The analysis of the variations of the b-values throughout the tests enabled an early detection of micro-cracks, before the first visual crack was noticed in all tested specimens. The occurrence of these micro-cracks was identified at the locations of sudden rise in the b-value versus test time curves.
- The intensity analysis parameters ($H(t)$ and S_r) were not significantly affected by the increase in the cover thickness of all samples. In addition, both results of $H(t)$ and S_r at the same crack widths showed very similar values at all percentages of steel mass loss in contrast with the b-values.
- Damage classification charts were developed to correlate the degree of steel mass loss and crack width to the acquired AE signal strength data ($H(t)$ and S_r). These charts categorized corrosion damage in steel into five degrees (1%, 2%, 3%, 4%, and 5%) of rebar mass loss. The charts also identified four groups of concrete cover crack widths (ranging from 0.08 to 5 mm) associated with the magnitudes of

$H(t)$ and S_r from the intensity analysis. These charts may be especially beneficial for the corrosion damage assessment of existing concrete structures at subsequent stages after corrosion initiation as a function of the collected AE signal strengths.

8.1.2 Corrosion Detection and Crack Growth Monitoring Using AE Sensors in Full-Scale RC Beams

- Identifying the locations of slope change of the cumulative number of hits, CSS, and S_r curves and sudden jumps in $H(t)$ values throughout the tests permitted the early detection of corrosion initiation and onset of corroion-induced cover crack growth prior to both the HCP tests and visual observation of cracks in all tested beams, irrespective of sensor location. This finding confirmed the outcomes of the previously implemented study and proved the feasibility of this approach for corrosion damage recognition, regardless of sample size.
- Studying the severe corrosion levels (up to 30% of steel mass loss) indicated the effectiveness of AE analysis to assess the corrosion propagation (in terms of steel mass loss and corroion-induced cover crack growth) in full-scale RC beams at all values of sensor distances from the source of damage. It was found that increasing the percentages of steel mass loss and corrosion-induced cover crack widths were associated with an overall increase in the studied AE parameters (cumulative number of hits, CSS, $H(t)$, and S_r).
- The increase in the sensor distance from the source of damage resulted in a general decline in the values of the signal amplitude, cumulative number of hits, CSS, $H(t)$, and S_r in all tested beams at all degrees of corrosion. This impact of

varying the sensor location was also highlighted as a result of using larger size beams (farther sensor distances from the source of damage) compared to the previous investigation. However, all sensors enabled the detection/characterization of all levels of corrosion damage in all tested beams with variable distances from the exposed bars ranged between 0.2 to 1.505 m.

- The average magnitudes of *H (t)* and S_r recorded using the three sensors in each beam were exploited to generate damage classification charts. These charts can be utilized to categorize the extent of corrosion progression of all tested beams in terms of corrosion stage and percentage of steel mass loss as well as to predict the range of the corrosion-induced crack widths.

8.1.3 Evaluation of Concrete-Steel Bond Behaviour Using AE Sensors in Small-Scale Corroded/Un-Corroded RC Samples

- The analysis of CSS, *H (t)*, and S_r versus test time curves allowed the detection of two early stages of bond loss, including micro- and macro-cracking prior to the occurrence of bond splitting failure, in all corroded/un-corroded samples. These stages were noticed at the locations of slope change in CSS and S_r curves. Accordingly, any linearity in these curves indicates no bond deterioration in the tested specimen. The micro- and macro-cracking stages were also identified at the points with sudden increases in the values of *H (t)*.
- *H (t)* showed to be more numerically sensitive than all other AE parameters for early detection of the micro-cracking stage of bond damage. At this early stage, no visible cracking or bar slippage were noticed in any of the tested samples.

- The values of different AE parameters including cumulative number of hits, CSS, *H (t)*, and S_r, were in a good correlation with the corrosion level in all tested samples. An overall reduction in all AE parameters (cumulative number of hits, CSS, *H (t)*, and S_r) was noted from increasing the corrosion level from 0 to 5% at the macro-cracking stage. In contrast, only AE cumulative number of hits, CSS, and S_r were decreased, in samples with higher corrosion degrees, at the micro-cracking stage. Moreover, a slight decline in the amplitude of the signals detected at both micro- and macro-cracking stages was warranted due to the presence of reinforcement corrosion.
- The growth of splitting cracks following the micro-cracking stage were accompanied by an overall increasing trend in the results of cumulative number of hits, CSS, *H (t)*, and S_r, in all corroded/un-corroded samples. In addition, these AE parameters were feasible in identifying the sizes of splitting cracks among the tested samples. An overall increase in these AE parameters was noticed from samples with larger splitting cracks at all bar diameters, cover thicknesses, and degrees of corrosion.
- The use of longer bonded length and thicker concrete cover resulted in higher AE cumulative number of hits, CSS, and S_r at both micro- and macro-cracking stages, in all corroded/un-corroded samples. The values of *H (t)* also increased as a result of using longer bonded length and larger cover thickness at the macro-cracking stage. However, insignificant changes in *H (t)* were found between all tested

samples regardless of bar diameter, bonded length, cover thickness, or steel mass loss at the micro-cracking stage.

- The AE signals associated with the detection of micro- and macro-cracking were characterized by higher amplitude values than that of the AE signals collected before the start of micro-cracking. Meanwhile, no explicit variations between waveform parameters (rise time, counts, cumulative number of hits, signal strength, energy, amplitude, duration, and frequency values) were observed at micro- and macro-cracking stages, in all corroded/un-corroded samples. In addition, the changes in bar diameter, cover thickness, corrosion level, and embedded length did not significantly affect the collected AE waveform signatures at all degrees of bond degradation.
- Damage classification charts based on the results of $H(t)$ and S_r were created to classify the stages of bond deterioration and quantify the amount of bar slippage of corroded/un-corroded bars embedded in concrete. These charts enable the characterization of the micro- and macro-cracking stages of bond damage and prediction of the range of bar slippage according to the detected AE signal strength data obtained from monitoring existing concrete structures.

8.1.4 Evaluation of Concrete-Steel Bond Behaviour Using AE Sensors in Full-Scale Corroded/Un-Corroded RC Beams

- All corroded beams exhibited bond failure at the corroded anchorage side after the formation of a large anchorage crack, as expected. Also, un-corroded beams followed a similar failure mode at one of the two anchorage ends of the beams.

- Studying the variations in AE number of hits, CSS, *H (t)*, and S_r throughout the bond tests enabled earlier detection of first flexural crack, initial slip, and anchorage cracking than visual inspection, in all corroded/un-corroded beams. These successive stages of damage were pinpointed at the locations of sudden rise in *H (t)* and slope change of AE number of hits, CSS, and S_r curves throughout the tests and were confirmed using the test data and visual observation of cracks. However, the review of intensity analysis parameters (*H (t)* and S_r) versus time curves showed a more evident identification of the extent of damage (detection of first crack, micro-cracking, and initial bar slippage) than did number of hits and CSS in all beams.
- Increasing corrosion level (5%-30%) yielded larger corrosion crack widths, lower load capacity, and lower bond strength, which also generally decreased the average AE parameters (number of hits, CSS, *H (t)*, and S_r) at both initial slip and anchorage cracking stages. On the contrary, changing corrosion level had no evident effect on the average magnitudes of these AE parameters at the first crack detection stage. Furthermore, the average values of signal amplitude exhibited non-significant variations at all degrees of deterioration between corroded/un-corroded beams or between corroded beams with variable corrosion levels.
- After the identification of bar slip, the increase in the values of bar slippage was accompanied by an overall increase in the values of AE parameters, including number of hits, CSS, *H (t)*, and S_r, until failure of all corroded/un-corroded beams.

This higher AE activity was correlated to the bond damage progression at the concrete-steel in terms of the increasing bar slippage.

- Varying the bonded length of the bars resulted in significant changes to both the load resistance and consequent AE parameters (in terms of number of hits, CSS, *H (t)*, and S_r) resulting from bond degradation in all tested beams. Increasing the bonded length of the bar (from 100 through 400 mm) increased the concrete-steel interaction and yielded higher values of the AE parameters, starting at the bond slip detection until failure. Conversely, the variable bonded length had no significant effect on the AE parameters recorded at the time of first crack of all beams.
- Increasing the sensor distance from the source location of damage slightly reduced all AE parameters (signal amplitude, number of hits, CSS, *H (t)*, and S_r) at all stages of damage in both corroded and un-corroded beams. Nevertheless, AE data from all sensors permitted the detection of first crack, slip initiation, and anchorage cracking up to a maximum sensor distance of 1505 mm from the source of bond damage.
- The *H (t)* and S_r results of all tested beams were utilized to establish a damage classification chart. This chart classified the damage of all beams into three levels including first crack, initial slip, and anchorage cracking before the occurrence of bond failure. This chart can be useful in identifying early stages of bond damage of both new and existing RC structures based on the AE data collected from continuous SHM systems.

8.1.5 Observed Limitations of AE Monitoring as a SHM Technique

- For the practical application of the findings of this thesis to aging concrete structures (which are already corroded to a certain degree of corrosion), the extent of corrosion damage may be determined by well-established non-destructive testing techniques, like guided wave based techniques.
- Some potential variations may exist between the results of this thesis and that expected in real concrete structures (such as the changes of ambient conditions, size of tested samples and pre-stressing of the reinforcement).

8.2 Recommendations for Future Research

- Further investigations involving the application of natural corrosion mechanisms are required in order to validate the presented results obtained from the current accelerated corrosion studies.
- Future studies are also needed to examine the effectiveness of AE monitoring in evaluating the condition of actual concrete structures exposed to variable ambient conditions (moisture and/or temperature variations) to complement/confirm the results of these investigations.
- The effects of other variables existed in real concrete structures such as; variable specimen size, rebar confinement conditions, and pre-stressing of reinforcement on the AE data also require additional investigations. In addition, the distribution of AE sensors at larger distances than those covered in this research (> 1.505 m) from the source of damage requires further research to generalize the outcomes from this research.

- The investigation of the influence of type of loading (static or dynamic) on the resulting AE data obtained from similar bond tests to those conducted in this research is also recommended. Meanwhile, the effect of varying concrete type (in terms of density and composition) on the AE data demonstrated in this thesis requires further examination.
- The effectiveness of AE monitoring for the evaluation of damage in RC structures exposed to combined corrosion and external loading acting simultaneously needs to be examined.
- Comparing the absolute values of the AE parameters from SHM systems from monitoring in-service concrete structures to those presented in this thesis can enhance the reliability of these results and improve the precision of the developed damage classification charts.
- The AE monitoring performed in this thesis was based on passive monitoring of AE signals generated during both destructive and non-destructive testing. Thus, investigating the feasibility of using an active AE monitoring system via ultrasonic or mechanical source as a non-destructive SHM tool for its practical application for testing real concrete structures is recommended for future work.
- The results from the pull-out tests may be used as a basis of comparison with other tests in the literature in order to develop refined equations and charts for evaluating the bond behaviour of RC structures.

Bibliography

Abdelrahman M, ElBatanouny MK and Ziehl PH (2014) Acoustic emission based damage assessment method for prestressed concrete structures: modified index of damage. *Engineering Structures* 60: 258-264.

Abdelrahman M, ElBatanouny MK, Ziehl P, Fasl J, Larosche CJ and Fraczek J (2015) Classification of alkali–silica reaction damage using acoustic emission: A proof-of-concept study. *Construction and Building Materials* 95: 406-413.

ACI Committee 222 (2001) Protection of metals in concrete against corrosion. ACI 222R-01, American Concrete Institute, Farmington Hills, Michigan, 41 pp.

ACI Committee 408 (2003) Bond and development of straight reinforcing bars in tension, American Concrete Institute, Farmington Hills, Michigan, 49 pp.

Aldahdooh MAA and Bunnori NM (2013) Crack classification in reinforced concrete beams with varying thicknesses by mean of acoustic emission signal features. *Construction and Building Materials* 45: 282-288.

Assouli B, Simescu F, Debicki G and Idrissi H (2005) Detection and identification of concrete cracking during corrosion of reinforced concrete by acoustic emission coupled to the electrochemical techniques. *NDT & E International* 38: 682-689.

ASTM C876 (1991) Standard test method for half-cell potentials of uncoated reinforcing steel in concrete, ASTM International, West Conshohocken, PA, USA.

ASTM C496 (2011a) Standard test method for splitting tensile strength of cylindrical concrete specimens. ASTM International, West Conshohocken, PA, USA.

ASTM G1 (2011b) Standard practice for preparing, cleaning, and evaluating corrosion test specimens, ASTM International, West Conshohocken, PA, USA.

ASTM C150 (2012a) Standard specification for portland cement. ASTM International, West Conshohocken, PA, USA.

ASTM C39 (2012b) Standard test method for compressive strength of cylindrical concrete specimens. ASTM International, West Conshohocken, PA, USA.

ASTM E1316 (2014) Standard terminology for nondestructive examinations. ASTM International, West Conshohocken, PA, USA.

Auyeung Y, Balaguru P and Chung L (2000) Bond behavior of corroded reinforcement bars. *ACI Materials Journal* 97(2): 214-221.

Behnia A, Chai HK, Ranjbar N and Jumaat MZ (2016) Damage detection of SFRC concrete beams subjected to pure torsion by integrating acoustic emission and Weibull damage function. *Structural Control and Health Monitoring* 23(1): 51-68.

Benavent-Climent A, Castro E and Gallego A (2009) AE monitoring for damage assessment of RC exterior beam-column subassemblages subjected to cyclic loading. *Structural Health Monitoring* 8(2): 175-189.

Benavent-Climent A, Gallego A and Vico JM (2011) An acoustic emission energy index for damage evaluation of reinforced concrete slabs under seismic loads. *Structural Health Monitoring* 11(1): 69-81.

Boller C, Chang FK, Fujino Y. (Eds.) (2009) *Encyclopedia of Structural Health Monitoring*. John Wiley & Sons, 1- 2960.

Butt SD (1996) Analysis of mining-induced high frequency microseismicity. PhD Thesis, Queen's University at Kingston, Ontario, Canada.

Carpinteri A, Lacidogna G and Pugno N (2007) Structural damage diagnosis and life-time assessment by acoustic emission monitoring. *Engineering Fracture Mechanics* 74: 273-289.

Carpinteri A, Lacidogna G and Niccolini G (2011) Damage analysis of reinforced concrete buildings by the acoustic emission technique. *Structural Control and Health Monitoring* 18(6): 660-673.

CEB-FIP (2000) State-of-the-art report on bond of reinforcement in concrete. State-of-Art Report Prepared by Task Group Bond Models (former CEB Task Group 2.5) FIB-Féd. Int. du Béton 1-97.

Colombo IS, Main IG and Forde MC (2003) Assessing damage of reinforced concrete beam using ‘‘b-value’’ analysis of acoustic emission signals. *Journal of Materials in Civil Engineering* 15(3): 280-286.

Craig BC and Soudki KA (2005) Post-repair performance of corroded bond critical RC beams repaired with CFRP. *Proceedings: FRP Reinforcement for Concrete Structures (FRPRCS-7), 7th International Symposium* (pp. 563-578), Shield, C. et al. Eds., ACI SP-230.

CSA (2014) Design of concrete structures. Standard CSA-A23.3-14. Canadian Standards Association, Toronto, ON.

Degala S, Rizzo P, Ramanathan K and Harries KA (2009) Acoustic emission monitoring of CFRP reinforced concrete slabs. *Construction and Building Materials* 23: 2016-2026.

Di Benedetti M, Loreto G, Matta F and Nanni A (2013) Acoustic emission monitoring of reinforced concrete under accelerated corrosion. *Journal of Materials in Civil Engineering* 25: 1022-1029.

Di Benedetti M and Nanni A (2014) Acoustic emission intensity analysis for in situ evaluation of reinforced concrete slabs. *Journal of Materials in Civil Engineering* 26(1): 6-13.

Di Benedetti M, Loreto G, Matta F and Nanni A (2014) Acoustic emission historic index and frequency spectrum of reinforced concrete under accelerated corrosion. *Journal of Materials in Civil Engineering* 26: 04014059.

ElBatanouny M, Mangual J, Ziehl P and Matta F (2014) Early corrosion detection in prestressed concrete girders using acoustic emission. *Journal of Materials in Civil Engineering* 26: 504-511.

ElBatanouny MK, Ziehl PH, Larosche A, Mangual J, Matta F and Nanni A (2014) Acoustic emission monitoring for assessment of prestressed concrete beams. *Construction and Building Materials* 58: 46-53.

Elfergani HA, Pullin R and Holford KM (2011) Acoustic emission analysis of prestressed concrete structures. *Journal of Physics: Conference Series* 305: 012076.

Ercolino M, Farhidzadeh A, Salamone S and Magliulo G (2015) Detection of onset of failure in prestressed strands by cluster analysis of acoustic emissions. *Structural Monitoring and Maintenance* 2(4): 339-355.

Ervin BL (2007) Monitoring corrosion of rebar embedded in mortar using guided ultrasonics waves. PhD Thesis, University of Illinois, Urbana-Champaign, USA.

Fang C, Lundgren K, Plos M and Gylltoft K (2006) Bond behaviour of corroded reinforcing steel bars in concrete. *Cement and Concrete Research* 36: 1931-1938.

Farhidzadeh A, Salamone S, Luna B and Whittaker A. (2012) Acoustic emission monitoring of a reinforced concrete shear wall by b-value-based outlier analysis. *Structural Health Monit*oring 12(1): 3-13.

Fowler TJ, Yepez LO and Barnes CA (1998) Acoustic emission monitoring of reinforced and prestressed concrete structures. In: Proceedings, *SPIE 3400*, Structural Materials Technology III: An NDT Conference, 281 (March 31, 1998); doi:10.1117/12.300100.

Fowler TJ, Yepez LO and Barnes CA (1998) Acoustic emission monitoring of reinforced and prestressed concrete structures. In: Proceedings, *SPIE 3400*, Structural Materials Technology III: An NDT Conference, 281 (March 31, 1998); doi:10.1117/12.300100.

Gallego A, Benavent-Climent A and Suarez E (2015) Concrete-galvanized steel pull-out bond assessed by acoustic emission. *Journal of Materials in Civil Engineering*, 04015109.

Ghiassi B, Verstrynge E, Lourenço PB and Oliveira DV (2014) Characterization of debonding in FRP-strengthened masonry using the acoustic emission technique. *Engineering Structures* 66: 24-34.

Giurgiutiu V (2008) *Structural Health Monitoring with Piezoelectric Wafer Active Sensors*, Elsevier Academic Press, 1-760, ISBN 978-0120887606.

Gjørv OE (2009) Durability design of concrete structures in severe environments. Taylor & Francis, London.

Golaski L, Gebski P and Ono K (2002) Diagnostics of reinforced concrete bridges by acoustic emission. *Journal of Acoustic Emission* 20(1): 83-89.

Goszczyn´ska B (2014) Analysis of the process of crack initiation and evolution in concrete with acoustic emission testing. *Archives of Civil and Mechanical Engineering* 14(1): 134-143.

Grosse CU, Reinhardt HW and Finck F (2003) Signal-based acoustic emission techniques in civil engineering. *Journal of Materials in Civil Engineering* 15(3): 274-279.

Grattan SKT, Taylor SE, Sun T, Basheer PAM, Grattan KTV (2009) Monitoring of corrosion in structural reinforcing bars: performance comparison using in situ fiber-optic and electric wire strain gauge systems. *IEEE Sensors Journal* 9: 1494-1502.

Ho SCM, Ren L, Labib E, Kapadia A, Mo Y-L, Li H and Song G (2015) Inference of bond slip in prestressed tendons in concrete bridge girders. *Structural Control and Health Monitoring* 22: 289-300.

Hooton RD, Geiker MR and Bentz EC (2002) Effects of curing on chloride ingress and implications on service life. *ACI Materials Journal* 99: 201-206.

Idrissi H and Limam A (2003) Study and characterization by acoustic emission and electrochemical measurements of concrete deterioration caused by reinforcement steel corrosion. *NDT & E International* 36: 563-569.

Ing M, Austin S and Lyons R (2005) Cover zone properties influencing acoustic emission due to corrosion. *Cement and Concrete Research* 35: 284-295.

Iwaki K, Makishima O, Tanaka H, Shiotani T and Ozawa K (2003) Evaluation of bond behavior of reinforcing bars in concrete structures by acoustic emission. *Journal of Acoustic Emission* 21: 166-175.

Ju M and Oh H (2015) Experimental assessment on the flexural bonding performance of concrete beam with GFRP reinforcing bar under repeated loading. *International Journal of Polymer Science* 2015, 367528: 1-11.

Jung Y-C, Kundu T and Ehsani MR (2002) A new nondestructive inspection technique for reinforced concrete beams. *ACI Materials Journal* 99(3): 292-299.

Kawasaki Y, Wakuda T, Kobarai T and Ohtsu M (2013) Corrosion mechanisms in reinforced concrete by acoustic emission. *Construction and Building Materials* 48: 1240-1247.

Kawasaki Y, Wasad S, Okamoto T and Izuno K (2014) Evaluation for RC specimen damaged from rebar corrosion by acoustic emission technique. *Construction and Building Materials* 67: 157-164.

Kobayashi K and Banthia N (2011) Corrosion detection in reinforced concrete using induction heating and infrared thermography. *Journal of Civil Structural Health Monitoring* 1:25-35.

Kurz JH, Finck F, Grosse CU and Reinhardt H-W (2006) Stress drop and stress redistribution in concrete quantified over time by the b-value analysis. *Structural Health Monitoring* 5(1): 69-81.

Lam CCC, Mandamparambil R, Sun T, Grattan KTV, Nanukuttan SV, Taylor SE, Basheer PAM (2009) Optical fiber refractive index sensor for chloride ion monitoring. *IEEE Sensors Journal* 9: 525-532.

Li Z., Zdunek A, Landis E and Shah S (1998) Application of acoustic emission technique to detection of reinforcing steel corrosion in concrete. *ACI Materials Journal* 95(1): 68-76.

Li D, Chen Z, Feng Q and Wang Y (2015) Damage analysis of CFRP-confined circular concrete-filled steel tubular columns by acoustic emission techniques. *Smart Materials and Structures* 24, 085017: 1-11.

Lovejoy SC (2008) Acoustic emission testing of beams to simulate SHM of vintage reinforced concrete deck girder highway bridges. *Structural Health Monitoring* 7(4): 329-346.

Lu Y, Zhang J, Li Z and Dong B (2013) Corrosion monitoring of reinforced concrete beam using embedded cement based piezoelectric sensor. *Magazine of Concrete Research* 65(21): 1265-1276.

Mangat PS and Elgarf MS (1999) Bond characteristics of corroding reinforcement in concrete beams. *Materials and Structures* 32: 89-97.

Mangual J, ElBatanouny M, Ziehl P and Matta F (2013a) Acoustic-emission-based characterization of corrosion damage in cracked concrete with prestressing strand. *ACI Materials Journal* 110(1): 89-98.

Mangual J, ElBatanouny M, Ziehl P and Matta F (2013b) Corrosion damage quantification of prestressing strands using acoustic emission. *Journal of Materials in Civil Engineering* 25(9): 1326-1334.

Maierhofer C, Reinhardt HW and Dobmann G, (Eds.) (2010) Non-destructive evaluation of reinforced concrete structures. Volume 2 of non-destructive testing methods, Woodhead Publishing, Oxford.

Martin-Peréz B, Pantazopoulou SJ, Thomas MDA (1998) Finite element modelling of corrosion in highway reinforced concrete structures. In Proceedings of Second International Conference on Concrete under Severe Conditions CONSEC ’98, Tromso, Norway.

Matta F, Rizzo P, Karbhari VM and Lanza di Scalea F (2006) Acoustic emission damage assessment of steel/CFRP bonds for rehabilitation. *Journal of Composites for Construction* 10(3): 265-274.

Miller TH, Kundu T, Huang J and Grill JY (2012) A new guided wave–based technique for corrosion monitoring in reinforced concrete. *Structural Health Monitoring* 12(1): 35-47.

Mistras Group (2007) PCI-2 based AE system user’s manual. Physical Acoustics Corporation, Princeton Junction, NJ, USA.

Mpalaskas AC, Vasilakos I, Matikas TE, Chai HK and Aggelis DG (2014) Monitoring of the fracture mechanisms induced by pull-out and compression in concrete. *Engineering Fracture Mechanics* 128: 219-230.

Mufti AA, Bakht B, Tadros G, Horosko AT, Sparks G (2007) Civionics – A new paradigm in design, evaluation, and risk analysis of civil structures. *Journal of Intelligent Material Systems and Structures* 18: 757-763.

Na W-B, Kundu T and Ehsani MR (2002) Ultrasonic guided waves for steel bar concrete interface testing. *Materials Evaluation* 60(3): 437-444.

Na W-B and Kundu T (2002) A combination of PZT and EMAT transducers for interface inspection. *Journal of the Acoustical Society of America* 111(5): 2128-2139.

Na W-B, Kundu T and Ehsani MR (2003) Lamb waves for detecting delamination between steel bars and concrete. *Computer-Aided Civil and Infrastructure Engineering* 18(1): 58-63.

Na W-B and Kundu T (2003) Inspection of interfaces between corroded steel bars and concrete using the combination of a piezoelectric zirconate-titanate transducer and an electromagnetic acoustic transducer. *Experimental Mechanics* 43(1): 24-31.

Nair A and Cai CS (2010) Acoustic emission monitoring of bridges: review and case studies. *Engineering Structures* 32(6): 1704-1714.

Nair A, Cai CS, Pan F and Kong X (2014) Acoustic emission monitoring of damage progression in CFRP retrofitted RC beams. *Structural Monitoring and Maintenance* 1(1): 111-130.

Nilson AH, Darwin D and Dolan CW (2010) *Design of concrete structures*. New York: McGraw-Hill.

Oh B, Kim K and Jang B (2009) Critical corrosion amount to cause cracking of reinforced concrete structures. *ACI Materials Journal* 106(4): 333-339.

Ohtsu M (1996) The history and development of acoustic emission in concrete engineering. *Magazine of Concrete Research* 48(177): 321-330.

Ohtsu M, Uchida M, Okamoto T and Yuyama S (2002) Damage assessment of reinforced concrete beams qualified by acoustic emission. *ACI Structural Journal* 99(4): 411-417.

Ohtsu M and Tomoda Y (2008) Phenomenological model of corrosion process in reinforced concrete identified by acoustic emission. *ACI Materials Journal* 105(2): 194-199.

Ohtsu M (2010) Test method for classification of active cracks in concrete structures by acoustic emission. *Materials and Structures* 43: 1187-1189.

Ohtsu M, Mori K and Kawasaki Y (2011) Corrosion process and mechanisms of corrosion-induced cracks in reinforced concrete identified by AE analysis. *Strain* 47 (2): 179-186.

Okude N, Kunieda M, Shiotani T and Nakamura H (2009) Flexural failure behavior of RC beams with rebar corrosion and damage evaluation by acoustic emission. *Journal of Acoustic Emission* 27: 263-271.

Otieno MB, Alexander MG and Beushausen HD (2010) Corrosion in cracked and uncracked concrete: Influence of crack width, concrete quality and crack reopening. *Magazine of Concrete Research* 62(6): 393-404.

Park C, Park Y, Kim S and Ju M (2016) New emerging surface treatment of hybrid GFRP bar for stronger durability of concrete structures. *Smart Structures and Systems* 17(4): 593-610.

Patil S, Karkare B and Goyal S (2014) Acoustic emission vis-à-vis electrochemical techniques for corrosion monitoring of reinforced concrete element. *Construction and Building Materials* 68: 326-332.

Physical Acoustics (2005) R6I-AST sensor, Princeton Junction, NJ, USA.

Pollock AA (1986) Classical wave theory in practical AE testing. In: Proceedings, *Int. Acoustic Emission Symp.*, Japanese Society for Nondestructive Testing, 708-721.

Poursaee A and Hansson CM (2009) Potential pitfalls in assessing chloride-induced corrosion of steel in concrete. *Cement and Concrete Research* 39: 391-400.

Puri S and Weiss J (2006) Assessment of localized damage in concrete under compression using acoustic emission. *Journal of Materials in Civil Engineering* 18: 325-333.

Qin F, Kong Q, Li M, Mo YL, Song G and Fan F (2015) Bond slip detection of steel plate and concrete beams using smart aggregates. *Smart Materials and Structures* 24: 115039, 1-13.

Ramadan S, Gaillet L, Tessier C, Idrissi H (2008) Detection of stress corrosion cracking of high-strength steel used in prestressed concrete structures by acoustic emission technique. *Applied Surface Science* 254: 2255-2261.

Ridge AR and Ziehl PH (2006) Evaluation of strengthened reinforced concrete beams: cyclic load test and acoustic emission methods. *ACI Structural Journal* 103(6): 832-841.

Rilem-Fip-Ceb (1973) Bond test for reinforcing steel: 1-Beam test (7-II-28 D). 2-Pullout test (7-II-128): tentative recommendations. *Materials and Structures* 6(32): 96-105.

Rizzo P, Spada A, Degala S and Giambanco G (2010) Acoustic emission monitoring of chemically bonded anchors. *Journal of Nondestructive Evaluation* 29: 49-61.

Rogers RA, Wotherspoon L, Scott A and Ingham JM (2012) Residual strength assessment and destructive testing of decommissioned concrete bridge beams with corroded pretensioned reinforcement. *PCI Journal* 57(3): 100-118.

Rucka M and Wilde K (2013) Experimental study on ultrasonic monitoring of splitting failure in reinforced concrete. *Journal of Nondestructive Evaluation* 32: 372-383.

Saboonchi H and Ozevin D (2013) MEMS acoustic emission transducers designed with high aspect ratio geometry. *Smart Materials and Structures* 22(9), 095006: 1-14.

Salamone S, Veletzos MJ, Lanza di Scale F, Restrepo JI (2012) Detection of initial yield and onset of failure in bonded posttensioned concrete beams. *Journal of Bridge Engineering* 17: 966-974.

Sagar RV, Prasad BKR and Sharma R (2012) Evaluation of damage in reinforced concrete bridge beams using acoustic emission technique. *Nondestructive Testing and Evaluation* 27(2): 95-108.

Sagar RV and Prasad BKR (2013) Laboratory investigations on cracking in reinforced concrete beams using on-line acoustic emission monitoring technique. *Journal of Civil Structural Health Monitoring* 3:169-186.

Schumacher T, Higgins CC and Lovejoy SC (2011) Estimating operating load conditions on reinforced concrete highway bridges with b-value analysis from acoustic emission monitoring. *Structural Health Monitoring* 10(1): 17-32.

Shahidan S, Pulin R, Bunnori NM and Holford KM (2013) Damage classification in reinforced concrete beam by acoustic emission signal analysis. *Construction and Building Materials* 45: 78-86.

Soudki KA, Rteil A, Hammoud R and Topper T (2007) Fatigue strength of fibre-reinforced-polymer-repaired beams subjected to mild corrosion. *Canadian Journal of Civil Engineering* 34(3): 414-421.

Staszewski WJ, Boller C and Tomlinson GR (Eds.) (2004) *Health Monitoring for Aerospace Structures: Smart Sensor Technologies and Signal Processing*. John Wiley & Sons, 1-288.

Talakokula V and Bhalla S (2015) Reinforcement corrosion assessment capability of surface bonded and embedded piezo sensors for reinforced concrete structures. *Journal of Intelligent Material Systems and Structures* 26(17): 2304-2313.

Vélez W, Matta F and Ziehl P (2015) Acoustic emission monitoring of early corrosion in prestressed concrete piles. *Structural Control and Health Monitoring* 22: 873-887.

Wu F and Chang FK (2006a) Debond detection using embedded piezoelectric elements in reinforced concrete structures – Part I: Experiment. *Structural Health Monitoring* 5(1): 5-15.

Wu F and Chang FK (2006b) Debond detection using embedded piezoelectric elements in reinforced concrete structures – Part II: Analysis and algorithm. *Structural Health Monitoring* 5(1): 17-28.

Wu F, Chan HL and Chang FK (2015) Ultrasonic guided wave active sensing for monitoring of split failures in reinforced concrete. *Structural Health Monitoring* 14: 439-448.

Yoon D, Weiss W and Shah S (2000) Assessing damage in corroded reinforced concrete using acoustic emission. *Journal of Engineering Mechanics* 126(3): 273-283.

Zaki A, Chai HK, Aggelis DG and Alver N (2015) Non-destructive evaluation for corrosion monitoring in concrete: A review and capability of acoustic emission technique. *Sensors* 15: 19069-19101.

Zhu XQ, Hao H and Fan KQ (2013) Detection of delamination between steel bars and concrete using embedded piezoelectric actuators/sensors. *Journal of Civil Structural Health Monitoring* 3: 105-115.

Ziehl PH, Galati N, Nanni A and Tumialan JG (2008) In-situ evaluation of two concrete slab systems. II: evaluation criteria and outcomes. *Journal of Performance of Constructed Facilities* 22: 217-227.

Ziehl P (2008) Applications of acoustic emission evaluation for civil infrastructure. In: Proceedings, Smart Structures and Materials, Nondestructive Evaluation and Health Monitoring, Society of Photo-Optical Instrumentation Engineers, Bellingham, WA, 693401.

Appendix

List of Publications from this Thesis:

A. Journal Papers:

1. **Ahmed A. Abouhussien** and Assem A. A. Hassan (2016) ‘‘Application of acoustic emission monitoring for assessment of bond performance of corroded reinforced concrete beams.” Structural Health Monitoring, pp. 1-13, (http://journals.sagepub.com/doi/abs/10.1177/1475921716681460).
2. **Ahmed A. Abouhussien** and Assem A. A. Hassan (2016) ‘‘Acoustic emission monitoring for bond integrity evaluation of reinforced concrete under pull-out tests.” Advances in Structural Engineering, pp. 1-16, (http://journals.sagepub.com/doi/abs/10.1177/1369433216678864).
3. **Ahmed A. Abouhussien** and Assem A. A. Hassan (2016) ‘‘The use of acoustic emission intensity analysis for the assessment of cover crack growth in corroded concrete structures.” Journal of Nondestructive Evaluation, 35(3), pp. 1-14, (http://link.springer.com/article/10.1007/s10921-016-0369-1).
4. **Ahmed A. Abouhussien** and Assem A. A. Hassan (2016) ‘‘Detection of bond failure in the anchorage zone of reinforced concrete beams via acoustic emission monitoring.” Smart Materials and Structures, 25(7): 075034, pp. 1-13, (http://iopscience.iop.org/article/10.1088/0964-1726/25/7/075034/meta).
5. **Ahmed A. Abouhussien** and Assem A. A. Hassan (2016) ‘‘Acoustic emission-based analysis of bond behaviour of corroded reinforcement in existing concrete structures.”

Structural Control and Health Monitoring, (http://onlinelibrary.wiley.com/doi/10.1002/stc.1893/full).

6. **Ahmed A. Abouhussien** and Assem A. A. Hassan (2015) ‘‘Evaluation of damage progression in concrete structures due to reinforcing steel corrosion using acoustic emission monitoring.” Journal of Civil Structural Health Monitoring, 5(5), pp. 751-765, (http://link.springer.com/article/10.1007/s13349-015-0144-5).
7. **Ahmed A. Abouhussien** and Assem A. A. Hassan ‘‘Acoustic emission monitoring of corrosion damage propagation in large-scale reinforced concrete beams.” Journal of Performance of Constructed Facilities **(Revision Submitted: Manuscript # CFENG-1906R1)**.

B. Conference Papers:

8. **Ahmed A. Abouhussien** and Assem A. A. Hassan, ‘‘Condition assessment of corroded reinforcement bond to concrete by acoustic emission monitoring.” Paper, 5th International Structural Specialty Conference, Canadian Society for Civil Engineering, CSCE Annual Conference 2016, June 1-4, 2016, London, Ontario, Canada.
9. **Ahmed A. Abouhussien** and Assem A. A. Hassan, ‘‘Cover crack growth monitoring in RC structures subjected to corrosion with acoustic emission sensors.” Paper, 5th International Structural Specialty Conference, Canadian Society for Civil Engineering, CSCE Annual Conference 2016, June 1-4, 2016, London, Ontario, Canada.

10. **Ahmed A. Abouhussien** and Assem A. A. Hassan, ‘‘Assessment of concrete-to-steel bond behaviour of reinforced concrete structures using acoustic emission intensity analysis.” Paper, 11th International Conference on Civil and Architecture Engineering, ICCAE-11, April 19-21, 2016, Cairo, Egypt.
11. **Ahmed A. Abouhussien** and Assem A. A. Hassan, ‘‘Experimental study on corrosion monitoring and assessment of concrete structures using acoustic emission.” Paper, International Conference on Advances in Structural and Geotechnical Engineering, ICASGE-15, April 6-9, 2015, Hurghada, Egypt.